1.0

4.5
5.0

2.8

2.5

3.2

2.2

1.1

3.6

4.0

2.0

1.8

1.25

1.4

1.6

MICROCOPY RESOLUTION TEST CHART
NATIONAL BUREAU OF STANDARDS 1963 A

50272-101

REPORT DOCUMENTATION PAGE	1. REPORT NO. SRS-483 UILU-ENG-80-2023	2. AD-A094 153	3. Recipient's Accession No.

4. Title and Subtitle

A STRESS ANALYSIS OF CIRCULAR CYLINDRICAL SHELL INTERSECTIONS, INCLUDING THE INFLUENCES OF REINFORCEMENT, CYCLIC PLASTICITY AND FATIGUE

5. Report Date
December 1980

6.

7. Author(s)
D. P. Rajkotia and W. C. Schnobrich

8. Performing Organization Rept. No.
SRS 483

9. Performing Organization Name and Address
Department of Civil Engineering
University of Illinois at Urbana-Champaign
Urbana, Illinois 61801

10. Project/Task/Work Unit No.
Proj. No. NR064-183

11. Contract(C) or Grant(G) No.
(C) N00014-75-C-0164
(G)

12. Sponsoring Organization Name and Address
Office of Naval Research, CODE N00014
Department of the Navy
Arlington, Virginia 22217

13. Type of Report & Period Covered
Technical Report

14.

16. Abstract (Limit: 200 words)

The intersection of cylinders is an unavoidable element in many engineering installations such as nozzle to cylinder connections in nuclear reactors or pressure vessels, pipe intersections in offshore platforms etc. The region of intersection presents a sharp geometric discontinuity in the structure which produces a stress field with very high stress concentration.

A unified in depth study of the behavior of cylinder intersections is presented in this document. This study consists of numerical evaluations of the stress fields in the vicinity of the cylindrical shell intersections. Included in the study are variations of reinforcement configurations around the curve of intersection, variations of nozzle to cylinder diameter ratios, variations of angles of intersection, and cyclic plasticity. The finite element method is employed for this stress analysis. An algorithm is developed for an automated mesh generation covering the region of the cylinder intersection. A kinematic strain hardening material model is formulated for application to cases with cyclic plasticity. The results of the nonlinear analysis are incorporated with existing numerical techniques to predict the fatigue life of the components involved.

17. Document Analysis   a. Descriptors

Fatigue
Finite Element Analysis
Pressure Vessels
Reinforced Openings

b. Identifiers/Open-Ended Terms   Shell Intersections

c. COSATI Field/Group   13. Mechanical, Industrial, Civil and Marine Engineering
M. Structural Engineering

18. Availability Statement	19. Security Class (This Report) Unclassified	21. No. of Pages 218
Approved for public release	20. Security Class (This Page)	22. Price

(See ANSI-Z39.18)   See Instructions on Reverse

OPTIONAL FORM 272 (4-77)
(Formerly NTIS-35)
Department of Commerce

1

ACKNOWLEDGMENT

Accession For

NTIS GRA&I	✓
DTIC TAB	☐
Unannounced	☐
Justification	

By

Distribution/

Availability Codes

| Dist | Avail and/or Special |

A

TABLE OF CONTENTS

v

vii

LIST OF TABLES

LIST OF FIGURES

1. INTRODUCTION

1.1 General

The importance of a stress analysis for intersecting cylindrical shells is well recognized because of the frequent occurence of intersecting cylinders in engineering structures. Examples include pressure vessels, boilers, pipe networks, etc. Until the last two decades, the design of the components involved in a cylinder intersection was carried out by rules-of-thumb. The trend towards the use of high strength materials for pressure vessels and the stringent safety requirements for nuclear reactor components, have intensified the need for a more complete understanding of the behavior of the region or vicinity which includes the cylinder intersection.

The introduction of a nozzle in a pressure vessel is a common requirement. The resulting discontinuity in the geometry introduces high stress concentrations in the region, thereby reducing the capacity of the vessel to withstand an internal pressure. If the vessel is to retain a significant percentage of its original capacity, additional material - "REINFORCEMENT" should be provided around the curve of the intersection. Moreover, by allowing a small amount of restrained plastic flow in this region, the stress concentrations can be smoothed out by redistribution, as long as the material is ductile and loading is

increasing monotonically (1.1)*.

However engineering structures which contain intersecting cylinders, are frequently subjected to constantly fluctuating loading conditions. This introduces another important factor for consideration, FATIGUE. A failure criteria attached only to the plasticity of a critical region may produce very deficient design. Due consideration must be given to the fatigue behavior of the structure when it is subjected to an anticipated history of stress reversals. A design which incorporates this fatigue consideration, depending upon life expectancy, may significantly restrain the allowable plasticity in the structure. An accurate and detailed determination of stresses in the vicinity of the cylinders' intersection would be of little value unless the designer recognizes the significance of those stresses in relation to fatigue. For a good estimation of the fatigue life of a structure, a reliable stress analysis including the possibility of material nonlinearity, is of primary importance.

To this end an analytical evaluation of the stress distribution using elastic thin shell equations, is almost impossible for cylinder intersections with a large aspect ratio because of the complexity of the curve of intersection. This curve is spacial and unique. No generalized equation exists for the definition of this curve. Within some restrictions the problem can be simplified by assuming a particular shape for this curve, for example selecting a circle in a plane for the case of

---

*Numbers in parentheses correspond to the references.

normally intersecting cylinders having a small aspect ratio. Of course, some inaccuracy is attached to this assumption. This inaccuracy becomes considerable for aspect ratios larger than one-third.

Earlier efforts to arrive at a generalized method of design for the case of intersecting cylinders were based on results derived primarily from experimental work. In the late fifties, two major projects were independently undertaken one under the auspices of the Welding Research Council and the other at the Oak Ridge National Laboratory. These initial experiments were carried out using the photo-elastic technique. Loading included both externally applied loads and internal pressure. Unfortunately the results from the experiments were very scattered making it almost impossible to derive, therefrom, any generalized equation around which to form a basis for design.

In recent years the finite element method has emerged as a very powerful procedure for general structural analysis. The method provides engineers with a versatile tool which has very wide applicability. The finite element method is now firmly established as the general numerical method to be used for obtaining a solution for complicated structures. The subdivision process of the method allows the specification of complicated configurations, abrupt changes in properties and even irregular geometrical boundaries. Moreover, the finite element method is one of the most efficient methods for the solution of structural nonlinearities. A cost analysis for the solution favoured the finite element method by a factor of 1:3 over a purely

experimental process for the evaluation of the stresses in the vicinity of a pipe intersection (1.2). Reliability and efficiency of the finite element method for the stress analysis of the intersecting cylinders is already proven (1.3).

1.2 Objective and Scope

Motivation of this research stems from the fact that, no unified in depth study of the behavior of the cylinder intersections, having a record of consistent results, exist. The decision is taken to approach this problem in the environment of a numerical method with proven reliability and accuracy. To carry out this goal of a unified study, various aspects of the behavior of the structure are investigated utilizing the finite element method. The objectives set down for the study can be summarized as :

1.   To carry out an in depth investigation of the effect of reinforcement around the curve of the cylinder intersection. One objective of this phase is to determine an efficient configuration for the reinforcement.

2.   To conduct a parametric study considering various aspect ratios and angles of intersection of cylinders, recognizing their influence on the variation in the stress pattern and associated stress concentration factors.

3.   To study the nonlinear cyclic response of the cylinder intersection. The derived results form a base which can be incorporated with existing numerical techniques to predict the fatigue life of the components.

To meet these objectives the following road map is taken.

It is well recognized that for a three dimensional structure such as intersecting cylinders the finite element mesh generation is one of the most formidable tasks that must be undertaken. Efforts are directed to develop a data generation algorithm. The algorithm is capable of handling any range of aspect ratios, angles of intersection, and reinforcement configurations. At the same time the algorithm is efficient, have simple input data requirements and is flexible enough for the user to readily change the layout of any region of the structure.

For the purpose of preparing an efficient structural model, three dimensional isoparametric elements are utilized in the vicinity of the curve of intersection. The rest of the structure is discretized using curved shell elements. For connecting the regions of three dimensional solid elements with the regions of curved shell elements, a transition element is developed. This element has one face like a three dimensional isoparametric element while the others are like a curved shell element. Moreover, three dimensional isoparametric transition elements are developed to facilitate the reduction in the layering of three dimensional elements through the thickness.

The concepts of isotropic strain hardening materials have been employed in an earlier nonlinear analysis of pipe

intersections (1.1). This idealization however breaks down when the structure is subjected to cyclic loads. A kinematic strain hardening material model is developed for application to cases with material nonlinearity. It should be noted that this study does not include the effects of temperature variations or creep on the response of the structure. Also the geometric nonlinearity is exluded by an assumption of small deformations.

2. CYLINDRICAL SHELL INTERSECTIONS

2.1 Introduction

In recent years the use of structures which contain cylinder intersections has been on a continually increasing trend. Many engineering installations now involve their use such as boilers, reactor pressure vessels, pipe networks in chemical plants, off-shore oil drilling towers, etc. In spite of these increased occurences no analytical solution has been achieved to form the basis for a design process for the region of the intersection. This lack of a solution has drawn the attention of many researchers who have followed several different approaches in search of a procedure capable of determining the stress patterns produced in the region of cylinder intersections.

2.2 Literature Review

2.2.1 General

The determination of stresses in the region of intersection is complicated because of the sudden discontinuity in the structure. This is particularly true in shell structures with their membrane or surface force characteristics. The complexity of the geometry of the curve of intersection further complicates the problem. The different approaches that have been tried for

the solution of this structural problem can be catagorized as :

1. Analytical approaches using differential equations.

2. Limit analysis techniques assuming a collapse mechanism.

3. Experimental studies employing model or component specimens.

4. Numerical analyses using computer oriented procedures such as Finite Element Analysis.

2.2.2 Analytical Approach

Classic analytical approaches were taken by almost all of the early researchers attracted to this problem. Classic analysis of the structure, however, has proved to be a very formidable task due to the fact that the curve of intersection is a three dimensional spatial curve without any symmetry. Idealization of this curve to a circle simplified the problem when a small cylinder intersected a large vessel. The solution produced an acceptable approximate analysis for these small aspect ratio cases.

Krisch (2.1) was the pioneer investigator researching the stress concentration around a hole in a flat plate subjected to an axial tension. Lure (2.2,2.3) was the first to attack the problem of a circular opening in a cylindrical shell. He produced his solution based upon the assumptions of thin shallow shell theory. Lure's study was directed to the case with an aspect ratio of less than 1/4. He wrote his solution in the form of a power series in a non-dimensional curvature parameter, viz.

the square of the hole radius divide by the product of the shell radius and the wall thickness. Similar approaches for related problems have been discussed by Pirogov (2.4), Savin and Gouz (2.5), and Gouz (2.6).

Lure and van Dyke (2.7) wrote the solution to the basic differential equations as a series of products of exponential and Hankel functions, subsequently splitting the solution into symmetrical and antisymmetrical parts by replacing the exponential terms by Krylov functions. Lekerkerker (2.8) wrote the exponential as Fourier-Bessel series, making the solution easier to handle analytically.

A comprehensive analytical treatment to a nozzle intersecting into a cylindrical shell was first given by Reidelbach (2.9). He applied Donnell equations for both cylindrical shells. There are some objections, however, to this approach because it neglects the interaction between different terms in a Fourier series expansion and it assumes the validity of Donnell equations for all cylinder intersections. When the cylinders are of equal diameters these assumptions are considered very inaccurate (2.10).

Tyn, Mint, Radok and Wolfson (2.11) used a Ritz method as the basis of their approach. They chose displacement components which satisfied the boundary conditions, and minimized the potential energy. The selected boundary conditions were such that the edge of the hole in the main shell was fixed or clamped. Based on Donnell equations Eringer and Suhubi (2.12) and Eringer, Naghdi, Mahmood, Thiel and Ariman (2.13) presented a solution for

a shallow shell intersection with an aspect ratio less than 1/4. Yamamoto, Isshiki, Hamada, Hayashi and Ukaji (2.14) treated the same problem by using Flugge equations for the branch shell and Donnell equations, including shallow shell conditions, for the main shell. Minimum energy principles were then used to establish compatibility between the two components of the structure. A comparision with experimental results revealed good agreement.

Some unsuccessful attempts were made to treat the problem of shells with aspect ratios larger than 1/4, that is for shells where the assumption that the curve of intersection is a circle, is not valid. Within this category we can list the investigations by Bylaard, Dohermann and Wang (2.15), van Campen (2.16) and Pan and Beckett (2.17). Bylaard employed Flugge equations for both shells, however, his paper concluded without giving any numerical examples. Van Campen formulated the problem using Morley equations for cylindrical shells. He concluded his paper with the mention of difficulties when numerical solutions were sought. Pan and Beckett used Donnell equations for the intersected shell. They gave a numerical example for an aspect ratio of 1/2. Their results compared qualitatively with experimental results. However, they also emphasized difficulties in achieving numerical solutions. Thus in spite of the assuring formal equations the ensuing numerical work ended in difficulties because of the existence of ill conditioning in the equations.

A concluding remark for this survey on analytical elastic approaches can be summarized as, in spite of the two decades of

research a proven method for stress analysis of cylindrical shell intersect;ons has not been found.

2.2.3 Limit Analysis

Another approach taken by some researchers for solving the problem is that of limit analysis. For the sake of simplification several assumptions, such as following, were made : it was assumed that both the shells were thin shells, elastic deformations were neglected, change in geometry was not included even for large deformations, and strain hardening was not considered. Within the confines of these assumptions, the limit approach can be classified either as 1. a lower bound solution or as 2. an *upper bound* solution. For the lower bound solution, kinematical criteria were ignored. Main workers in this area have been Robinson (2.18,2.19), Ellyin and Turkkan (2.20), and Biron and Courchese (2.21). For the upper bound solution stress equilibrium conditions were ignored. Some work in this area was carried out by Goodall (2.22), Cloud (2.23), and Schroeder and Roy (2.24,2.25).

Limit solutions contain many assumptions and approximations, hence their results may be far from any realistic solution. They may be good enough, however, to give a rough estimate for the stress concentration factor. Precautions should be taken before a solution is qualified as a true lower bound or even a reasonable engineering evaluation of a true lower bound, as suggested by .iron and Courchese (2.21).

2.2.4 Experimental Approach

Experimental work has been done by various researchers seeking a solution to the shell intersection problem. Generally the experiments have been carried out by utilizing steel models or by photo-elastic methods. These experiments are few in number, because of the difficulties associated with precise modelling of a thin shell and the costs involved in such fine modelling.

The earliest record of such experimentation is found in Welding Research Council Bulletin of 1959. Hardenbergh (2.26), reported the results for a metallic model under internal pressure. Strains were measured utilizing rectangular strain rosettes at locations well removed from the branch connection. In the same bulletin Taylor, Lind and Schweiker (2.27) reported their experiments with photo-elastic models. The ultimate goal of this latter study was to investigate the effect of the important parameters on the stress amplification, and to establish a procedure and criteria for the design of reinforced openings. The above paper presented the experimental results but it failed in establishing correlations with different parameters. The results of the study are of an uncertain value as their validity is questioned because of the wide scatter in the data, as indicated by Mershon (2.28).

Hardenbergh and Zarmik (2.29) reported the results of experimental stress analyses of full scale steel models of cylinder intersections. Measurements were obtained through the use of electrical resistance strain gauges. Their results

indicated the necessity of proper reinforcement around the nozzle for the purpose of reducing the stress amplification. No concluding remarks were made. Experimental studies with externally applied loads were also carried out by Hardenbergh and Zarmik (2.30), and Riely (2.31). These researchers studied the effect of axial thrust and bending on the stress pattern. Other reports on experimental results of tests on full scale steel models were given by Meringer, Cooper (2.32) and Cranch (2.33). General behavior and shifts in the region of stress concentration were studied by Taniguchi, Kono, Iki and Setoguchi (2.34), for the case of externally applied loads. No attempt was made to arrive at any generalized equation. Gwaltney, Corum, Bolt and Bryson (2.35), carried out experiments with very well controlled steel models to study elastic response of the structure under internal pressure along with externally applied loads.

Very few experiments have been carried out which extend into the plastic range of material behavior. First mention of such a test is by Lind, Sherboune, Ellyin and Dainore (2.36). They came to the conclusion that the shape factor, which is defined as the ratio of plastic limit pressure to the elastic limit pressure, was as high as 3.8 for their models.

Further experimentations on cylinder intersections, in the plastic range, under internal pressure and externally applied loads were carried out by Schroeder, Shrinivasan and Graham (2.37), Ellyin (2.38,2.39), Maxwell and Holland (2.40) and Schroeder and Tugcu (2.41). These studies outlined the general behavior of the structure in the plastic range and how, in an

overall sense, varying parameters like aspect ratio, diameter to thickness ratio etc. change this general behavior. Unfortunately, the scatter of the results from the various tests is too large to arrive at any specific conclusions.

2.2.5 Finite Element Approach

The earliest attempt at a solution to the pipe intersection problem by the finite element method was reported by Prince and Rashid (2.42). In the earlier stages of development, flat plate triangular elements were used in the modelling process. Because of their discretization errors, a large number of such elements were needed to converge to a reasonable answer. Qualitative agreement of the results with experimental values, however, demonstrated the general potential of the method.

Greste (2.43), developed a program for the finite element mesh generation appropriate to cylindrical shell intersections. He used two dimensional flat rectangular elements that included membrane and bending behavior, but were restricted to the elastic range of material response. The numerical results obtained, using this program, were in reasonable agreement with the experimental values derived by Corum, Bolt, Greenstreet and Gwaltney (2.35,2.44).

Hellen and Money (2.45), and Bathe, Bolourchi, Ramaswamy and Snyder (2.46) demonstrated general capabilities of the stress analysis for the intersecting structures. This involved the use of BERSAFE for the linear analysis and ADINA for the nonlinear analysis. Ando, Yagawa and Kikuchi (2.47) used elements based on

Novozhilov and Mushtari-Vlasov shell theories for their finite element analysis of both inclined and normally intersecting cylinders.

The use of different types of elements in a mesh of finite elements was introduced by Bakhrebah and Schnobrich (1.3). Three dimensional isoparametric elements were used in the region of stress concentration, that is, near the curve of cylinder intersection while Ahmad shell elements were used throughout the rest of the structure. Incompatible modes and the technique of reduced integration were employed for improvement in results. The study showed good agreement with the elastic response of Corum's experimental effort.

The versatility of the finite element analysis for nonlinear behavior of structures was demonstrated by Argyris, Faust, Szimmat, Warnke and Willam (2.48). For the study of cylinder intersections, Gwaltney, Corum, Bolt and Bryson (2.49) used flat plate elements with five degrees of freedom at each node (Hsiegh, Clough and Tocher element). Their results demonstrated good agreement with earlier experimental results for nonlinear response. Eight node three dimensional solid elements with incompatible modes were employed by Brown, Haizlip, Nielson and Reed (1.2), for the problem of normally intersecting cylinders. They utilized three layers of such elements through the thickness over the entire structure. Gantayat and Powell (2.50) also used the same element but restricted the discretization to a single layer through the thickness.

Chen and Schnobrich's (1.1) contribution to the finite element analysis of intersecting cylinders involved the development of a general procedure, with material nonlinearity. Three dimensional solid elements were used, through the thickness, in a layered configuration. These were confined, however, only to the region of stress concentration. Curved Ahmad shell elements were used throughout the remainder of the structure. A criterion including isotropic strain hardening was considered with monotonically increasing load. Stress analysis was performed on normally intersecting cylinders under internal pressure.

Kroenke and Mckinley (2.51), compared their nonlinear finite element analysis results for the cylinder intersection, subjected to an internal pressure loading, with the test results from a steel model. The analysis was carried out by using the computer program ADINA. Degenerated 8 noded isoparametric elements were utilized by arranging them in three layers through the thickness in the region of the stress concentration. A good agreement of the results was observed in the elastic range. However, in the plastic region, the structural response of their analysis was considerably stiffer than that observed in the test results.

2.3 Reinforced Opening

2.3.1 General

High stress concentrations exist in the vicinity of the curve of intersection of the cylinders. This curve poses the "weakest link in the chain", therefore it requires careful attention during design in order to maintain the safety of the structure. It is highly uneconomical and impractical to let the high local stresses of this region govern the design. Branch pipe connections of ductile materials, if provided with proper reinforcement, are capable of developing large plastic deformations, thus having considerable plastic reserve strength beyond the elastic limit pressure.

2.3.2 Previous Work

The amount of reinforcement and its effective distribution around the curve of intersection has posed a formidable question for many designers and researchers. In 1956 the Pressure Vessel Research Committee undertook a ten year program aimed at the development of a theory for reinforced openings (2.52). Photo-elastic experiments were carried out at various research centers like the University of Illinois at Urbana-Champaign, the University of Waterloo and the Westinghouse Research Laboratories. However the photo-elastic experimental results showed an overall scatter of about 20%, while having consistantly lower values than comparable results from experiments with steel

models. It was concluded that photo-elastic experiments were not entirely adequate for nozzle tests, because in this case a variation of the parameters produces only small changes in the stress distribution (2.28).

For small aspect ratios of d/D < 1/3, Chukwujekwu (2.53) and Cloud and Rodabaugh (2.54) proposed design methods for the reinforcement. These design methods were based on a limit analysis, where a dimensionless parameter ρ was correlated with an expected reinforcement thickness. The values of the parameter ρ are given by

$$\rho = \frac{d}{D} \sqrt{D/T} \qquad (2.1)$$

Design curves were proposed covering the range of 0.1 < t/T < 2.0

Another approach was suggested by Atterbury and Bert (2.55) by employing simple beam theory. The stresses at the critical point were divided into two components, membrane stresses and bending stresses. Curves of desirable stress level were plotted against the thickness ratio for various ratios of membrane and bending stresses. The application of a simple beam theory to the cylindrical shell intersection problem is, however, highly questionable.

2.3.3 Requirements for an Effective Design

Additional material should be provided around the curve of intersection to compensate for the weakening effect. This added material should be integral with the structure ie. it should be fully continuous with the shell, as contrasted with pad or saddle reinforcements which are welded to the shell only along the inner and the outer peripheries. However, it is observed that such pad or saddle reinforcement if welded with adequate shear strength is qualitatively equivalent to integral reinforcement (2.56).

The reinforcement should be provided in an adequate amount to significantly reduce the high stress amplification. The cost of material making up the reinforcement is negligible compared to its benefits, hence under-reinforcement should be avoided. On the other hand the addition of too large an amount of material has a reverse effect. An over-reinforced location restrains the natural expansion of the cylinder under internal pressure, creating the effect of a hard spot thereby overshooting the local stresses. This is analogous to "pinching a balloon".

The reinforcement should be provided in the region of its greatest effectiveness. A suitable configuration should be provided to avoid any high local stress concentrations. Extension of reinforcement lengths beyond the required limit is equivalent to increasing the thickness of the walls of the shells. The transition from unreinforced to reinforced thicknesses should be gradual so as to avoid any local sharp discontinuity. There are three possible locations for the provision of the reinforcement, viz. outside the nozzle, outside

the cylinder and inside the cylinder Fig. 2.2. It seems obvious that the most desirable situation is to provide equal distributions of reinforcement to the inside and the outside of the cylinder to avoid any eccentricity. However, it is common practice to avoid inside reinforcement because of its difficulty in fabrication.

2.3.4 Established Design Procedures

Various methods currently exist for the design of reinforced openings. The design procedures are formulated on four different bases which can be categorized as follows :

1. Design procedures evolved only by experience without any specific objective foundations, as a rule-of-thumb (2.57).

2. Design procedures based on simple elastic analysis using shell equations valid for small aspect ratios (2.58).

3. Limit stress analysis with restrictions on the maximum allowable stress is the basis of some design procedures (2.59).

4. Design procedures based on experimental evaluations of models and their extrapolations and interpolations (2.60).

The current American practice as described in several American design codes (2.57), is based on past experience which is expressed as a rule-of-thumb. The specifications require that the material cut out by the opening, ie. D*T, be replaced around

the opening within an effective zone. The effective zone is defined as shown in Fig. 2.3.1. Along the cylinder it is equal to the greater of either the diameter of the finished opening or the radius of the finished opening plus the thickness of the cylinder wall plus the thickness of the nozzle wall. Normal to the cylinder the effective zone is defined as the smaller of either 2.5 times the nominal cylinder thickness or 2.5 times the nozzle wall thickness. It is further proposed that the area of the reinforcement at the transverse section can be curtailed to half of its value at the longitudinal section with a smooth transition traversing between these limits. The longitudinal and the transverse sections are defined as, plane X-Z and Y-Z respectively in Fig. 2.1. It should be noted that no theoretical formulation exists to substantiate this reduction in reinforcement area.

The British Standards Institute (2.59) specification for reinforcement is based on a limit stress analysis. The design criterion limits the calculated maximum stress in a reinforced spherical shell to 2.25 times the nominal stress in the unperforated sphere. It should be noted that the nozzle-in-sphere theory is assumed to be valid for the nozzle-in-cylinder case. The applicability is restricted to an aspect ratio of less than 1/3. Design curves are given to predict the increase in the shell wall thickness depending upon a dimensionless parameter ρ , which is defined by Eq. 2.1. The reinforcing length along the nozzle, Fig. 2.3.2, is specified as the square root of the product of the inside diameter of nozzle

times reinforced thickness of the nozzle. Along the cylinder the length of reinforcement is specified as the smaller of either one half the inside diameter of nozzle or the square root of the product of the inside diameter of cylinder times the reinforced thickness of the cylinder.

The design specification established by the German code (2.60) is based on experimental investigations. A large number of tests were performed to determine the internal pressure which produced a permanent strain of 2%. Design plots are proposed with a dimensionless variable parameter ρ , as defined by Eq. 2.1. The reinforcement length requirements by the German code are, along the nozzle, the square root of the product of the internal nozzle diameter times the reinforced thickness of nozzle, and along the cylinder, the square root of the product of cylinder diameter times its reinforced thickness.

2.4 Numerical Analysis

It is interesting to note that the specifications of standard design of the various countries are based on completly different foundations. This diversity indicates a fundamental disagreement in the design philosophy and the complexity of the problem. Most of the design methods were developed before the last decade, when the use of the finite element technique was not yet established for the numerical stress analysis of complex structures like cylinder intersections. No extensive effort has been noted in the literature relative to the investigation of the behavior of reinforced shell intersections using the finite

element technique.

In the present study the effect of various configurations of reinforcement on the structural response is studied by utilizing the finite element method. The reinforcement is provided in all possible geometries, however an in depth study is performed with the reinforcement only on the outside of the cylinder. The structural modelling and the results are discussed in the latter part of this document.

3. THE FINITE ELEMENT ANALYSIS

3.1 The Finite Element Method

3.1.1 General

Developments in the field of computational hardware have put sophisticated powerful computers within easy reach of researchers. This has played an important role in the phenomenal progress that has occured in the development of various numerical methods. Any attempt at presenting in detail the developements that have occured in field of the finite element analysis would be far beyond the feasible bound of this document. Moreover many excellent books(3.1,3.2,3.3) are already aviaiable that cover the details of these developments. Popularity of the finite element technique stems from the fact that a complex structure can be discretized into small elements that are easily implemented in a computer application. Also due to the fact that this method handles complex boundary conditions, irregular shapes, inhomogeneity in material composition and mixed structures with relative ease.

In this work the displacement method is used for the solution. A brief formulation of the displacement method along with other important facets of the technique are presented here, to complete the documentation. Extension of the finite element technique for the inclusion of material nonlinearity is

discussed in Chapter 5.

3.1.2 The Formulation of Displacement Method

The displacements of a point in an element can be correlated to the displacements of the element nodes by :

$$u_i = [N] \{u\} \tag{3.1}$$

where [N] represents the interpolation functions called "shape functions".

From the theory of elasticity we know that the Green's strains at a point of interest in the element can be obtained by taking the proper derivatives of the displacement field with respect to any selected coordinate system. Hence the strain displacement relationship can be expressed in matrix form as:

$$\{\varepsilon\} = [B]\{u\} \tag{3.2}$$

where [B] depends on nodal coordinates.

The uniaxial stress strain curve of the material can be used to formulate the constitutive relation. For the elastic case this is easy to derive from a Hookian law. The 2 nd Piola-Kirchoff stress can be expressed as:

$$\{\sigma\} = [D] \{\varepsilon\} \tag{3.3}$$

where [D] is the material property matrix.

For a surface traction { T } and a body force { F } , the work eqivalent nodal load { P } is :

$$\{P\} = \int\limits_V [N]^T \{F\} dV - \int\limits_S [N]^T \{T\} dS \qquad (3.4)$$

For the equilibrium of the system, utilizing the principle of virtual work, it can be shown that :

$$[K] \{u\} = \{P\} \qquad (3.5)$$

where $[K] = \int [B]^T [D] [B] dV$ is the stiffness matrix of the element.

At the structure level, all the stiffness matrices of the elements and the equivalent nodal loads for those elements are assembled by proper superposition. The manner depends upon the element configuration in the structure. The resulting matrix equation is solved with proper values of known boundary displacements and equivalent nodal loads to evaluate displacements of active nodes. The set nodal displacements are then applied at the element level to find the stresses and the strains at desired points within an element.

3.1.3 Structural Modeling

Governing parameters which influences the decisions on the manner of structural modeling are, desirable accuracy and computational cost. The optimum level of combination of these parameters is achieved only after studying the behavior of the selected elements and preliminary study of the structure under given loading conditions and with specified constraints.

An important aspect contributing to the accuracy of the finite element technique is the selection of the right type of element. Depending upon the expected behavior of the structure, in a given zone under a prescribed load, a proper selection of element, one having the desired behavioral characteristics, is made. Either the same type of elements is used for the entire structure or different types of elements are used in different zones of the structure. This latter modeling may require some transition elements in the connecting region, wherein the dissimilar element types are joined.

Efficient use of the finite element method is achieved by using an optimum size of mesh with proper degrees of freedom at the nodes, depending upon the behavior of the structural response under consideration. It is desirable to have a finer mesh for accuracy but at the same time the finer the mesh, the larger the number of nodes, the more the number of equations and the higher the computational costs. Moreover beyond an optimum size of the mesh, the achieved addition in the accuracy is not significant. However it is important to restrict the size of elements in a region where the stress gradient is sharp, like the region

surrounding a sudden discontinuity in the stress field.

3.1.4 Substructuring and Static Condensation

Substructuring is a powerful tool for dealing with large structures, which otherwise might be too big to solve (3.4). Most finite element programs have a limitation on the maximum number of nodes and elements that can be used in a structure. In the finite element program FINITE, used for the solutions of this research, a maximum of eight hundred and thirtythree is set as a maximum limit on the nodes and one thousand as the maximum limit on the number of elements. A structure consisting of nodes or elements in numbers exceeding these limits, can only be solved by substructuring the problem into smaller structures then condensing out sufficient nodes so that no intermediate substructure or the final structure exceeds the specified limits at any time.

If a structure is a combination of repetitive components, it may be possible to save considerable computational time by defining a typical component as an idenity , viz. a substructure. This substructure can be reduced by condensing out all the internal nodes while keeping only those nodes which connect it to the adjacent substructure. The stiffness matrix is calculated only once for the substructure and the same matrix is used for each repetition of the component. Furthermore, for a linear response of the structure, the stiffness matrix for only one component of the structure need to be stored, making it possible to deal with large structures without exceeding the

capacity of the machine.

Substructuring also makes the task of structure discretization easier for large structures of complex geometry. The numbering of the nodes in proper sequence to minimize the band width, is an important factor in the economical utilization of finite element programs. The efficient sequencing of numbering in the case of a large and complex structure presents a formidable task. The structure can be divided into smaller substructures thereby making discretization easier.

The advantages of substructuring in a nonlinear finite element analysis are significant. Nonlinear analysis involves the updating of a structural stiffness matrix as well as the performance of many iterations, solving the governing equations until a selected convergence criteria is meet. Any saving in the computational time during the process of equation solution is compounded many times, thereby, leading to an impressive reduction in cost. Most structures have localized zones of stress concentration, limiting the zones of material plasticity. By condensing out parts of a structure, with an expected elastic response, considerable reduction in the number of equations to be solved can be achieved. Moreover, the stiffness update can also be restricted only to those substructures with expected material nonlinearity.

Careful attention is needed, however, in the selection of the number of uncondensed nodes on the boundaries of the structure. The stiffness matrix of a condensed structure, unlike that of the parent structure, may be a full matrix. Due to this

fact the process of static condensation of a substructure can actually increase the half band width of the stiffness matrix of the assembled structure, thereby, resulting in an increase in the computational cost. Substructuring is particularly effective for branch or tree like structures but not for square surface type structures.

Taking all these factors into consideration, the structure of the cylinder intersection, the problem investigated in this study, is divided into three basic substructures, Fig. 3.1. These are designated as Nozshell, Cylshell and Solid. The structures Nozshell and Cylshell are condensed out keeping only the nodes along their edges in order to make the connection with Solid.

3.1.5 Computer Algorithm

Solution of any practical size structure, by the finite element method, involves a considerable amount of computation and book-keeping. Without the availability of modern computer hardware and software capabilities, the application of the method would be impossible. In recent years, an enormous amount of computer software has been developed for handling the requirements of the finite element method.

At the university level, there is a general trend for researchers to develop a new system entirely. Primary concern of most such programmers, with specialization in the development of the finite element method, is to develop an algorithm suitable to a digital computer for the solution of a specific problem.

However, it is well recognized that most of these programs are quite incapable of handling problems that involve any significant modifications. At the same time these programs are deficient in the general ability required by a good system. As most of the components of a generalized system are the same, large amounts of research effort are wasted in repetitive development. A researcher in the development of the finite element technique should restrict his efforts to analytical aspects of the field with the implementation of the algorithms reflecting only new developments.

The aim of most commercially developed finite element programs is for a system with minimum input efforts to achieve maximum benefits. However, most of these systems lack the capability of interfaces or the flexibility to incorporate any new developments, well desired by the user. The efforts of most of the users of such systems are restricted only to effective discretization of the structure, preparation of input data and interpretation of output results. For such systems' users, considerable engineering time could be saved by properly designed free formated input data requirements along with plotting capabilities. Adequate output information in a well tabulated format is also a desirable feature for quick interpretation of results.

The implementation of a general purpose system is a formidable task requiring considerable knowledge of computer science. Factors which distinguish a good system from others can be summarized as man-machine communication (input & output),

mathematical modelling capabilities, source utilization, flexibility, restart capability, error recovery, maintainability and portability.

A versatile and highly capable system, called POLO-FINITE (3.5), with all the above mentioned features has been developed at the Civil Engineering Research Laboratory at the University of Illinois at Urbana-Champaign. In the present study the POLO-FINITE system is used as the base program to which required algorithms are developed and added.

3.2 Intersecting Cylinders

3.2.1 General

In the present study the intersecting cylindrical shell is the structure of prime interest. From previous studies of this problem (1.1), the general format of the stress patterns can be predicted. It is noted that the curve of intersection presents a sudden discontinuity in geometry, thereby inducing very high stresses in this region with the dominating stress being bending stress. These high stresses in the area of concentration decay within a small distance away from the curve of intersection. The decay is at a rather rapid rate with the results converging to the membrane stresses. It is desirable to use very small elements in the region close to the intersection curve in order to monitor these high stresses and their gradients. The mesh should get coarser away from the region as the stress gradient

diminishes, this to ensure a minimal computational cost. To organize such a modeling arrangement it is convenient to define different zones in the structure for the purpose of different levels of discretization.

The intersecting cylinder is called henceforth by the term "Nozzle". The intersected cylinder is simply referred to as the "Cylinder". Fig. 3.1

3.2.2 Region Of Stress Concentration

In the case of the nozzle, the situation is similar to a cylindrical shell subjected to an edge load at one of its ends. The stress distribution for this type of structure can be found by applying standard solution techniques for cylindrical shells, while using equations of a Donnell or even Flugge type. It is observed from these solutions that the effect of an edge disturbance induced on a cylinder by boundary loads decays at a very rapid rate. The stresses become negligible at a distance of 2.45 $\sqrt{r*t}$ from the edge. However there is one exception to this case which must be mentioned here. When the edge of the cylinder is subjected to a self equilibriating axial force, like that of a sine function, the resulting disturbance propogates a very long distance along the cylinder, Vlassov (3.6). This can contribute to an ovalling or a buckling collapse of the cylinder in some cases.

From the observation of the work done by various researchers (1.3,3.7) it is deduced that in the case of the cylinder, the stresses stabilize at a distance of 2.0 - 2.8 $\sqrt{R*T}$.

3.2.3 The Selection of Elements

Away from the zone of stress concentration, the stress field is dominated by membrane stresses. An Ahmad shell element (3.8) is a suitable selection for this region. This element is derived from a three dimensional isoparametric element Fig. 3.2. An assumption is made during the derivation of this element which excludes the possibility of the ill conditioning that otherwise would occur as a consequence of the thickness being very small compared to the other dimensions of the element. This frees the selection of the dimensions other than the thickness, from a restriction based on the aspect ratio relative to the thickness. A relatively coarser mesh is then adequate for the structure dominated by membrane stresses.

The use of a shell element even in the region of stress concentration, as has been employed in some previous studies (2.43), should be avoided. At the curve of intersection inplane bending of an element on the Nozzle causes out of plane bending of the connecting element on Cylinder and vise versa. The formulation of the Ahmad shell element does not include inplane bending as a degree of freedom. When the equations are written in a cartesian global system this can result in a lack of independence in the equations. To avoid the resulting ill conditioning a rotational spring with an arbitarily assigned stiffness is implemented at each node. Hence, due to this approximation an Ahmad shell element is inherently inaccurate for inplane bending, thereby, causing an inaccuracy in the most sensitive region of the structure. Furthermore, unless the

tangential and normal displacements are of equal order the displacements of the various elements are not compatible along the curve of intersection. Finally, because the curve of the cylinder intersection is a complex spacial curve, definition of a unique normal direction at the junction is impossible.

Three dimensional solid isoparametric elements are selected for applications in the region of stress concentration. Fig. 3.3. The dimensions of these elements are restricted to follow normal rules of element proportioning, thereby, keeping the aspect ratio of the elements to less than 20.

Improvement in the accuracy of the computed stress values can be achieved by using two layers of elements through thickness. In case of a nonlinear analysis, stress values and yield functions are computed at the integration points. Each integration point is representative of the material in the vicinity of the point up to approximately half the distance to the adjacent integration point. In most of the intersecting cylindrical structures the yielding starts from the inside surface (1.1) and propogates toward outside surface.

Precise observation of the progression of the yielding is dependent on the number of integration points through thickness. For early detection of the initial yielding an integration point placed close to the inside surface is advisable. Two layers of the three dimensional isoparametric elements with two integration points through their thickness, has an integration point at 0.1057*t away from the inside surface. While one layer of the same elements with three integration points through the thickness

would have an integration point at 0.1127*t away from the inside surface.

It should be borne in mind that by providing two layers of three dimensional elements through thickness the band width of the simultaneous equations increases considerably, increasing the computional cost by a high factor. A proper selection should be made between desirable accuracy versus its cost.

3.2.4 Transition Elements

Two main categories of transition elements are developed for the purpose of connecting different types or arrangements of elements organized in various combinations within a single problem.

3.2.4.1 3D Transitional Elements

A class of three dimensional isoparametric elements with fifteen, sixteen and seventeen nodes is developed, Fig. 3.4. This group of transitional elements makes any combination of layering possible between adjacent regions of the shell, particularly allowing more layers in the region of stress concentration. Formulation of these elements is based on the assumption that the displacement variation along an edge having two nodes is linear while that for the edge having three nodes is quadratic. Because the formulation of the stiffness matrix and equivalent load vector for the family of isoparametric elements is well established(3.1), that formulation will not be reiterated

here.

3.2.4.2 Transition Shell Element

the combination of three dimensional isoparametric elements, in the region of stress concentration and Ahmad shell elements throughout rest of the structure is made possible by the introduction of a transition element capable of connecting these two markedly different types of elements. A quadratic transition shell element with eleven nodes is developed for this purpose, Fig. 3.4. An Ahmad shell element is degraded on one face so as to appear on that face as a sixteen noded three dimensional isoparametric element. That one face of this transition element then contains six nodes with three degree of freedom at each node.

As the Ahmad shell was already implemented in the computer program FINITE, advantage of this is taken by using that already programmed element as a base for the implementation of the transition element. The face to be used as the connection to the solid element, is modified by using the assumption of a linear variation of displacement through the thickness. This assumption is inherent in the basic formulation of the shell element. The stiffness of the transition shell element is obtained by the simple transformation of displacements. The same simple transformation applies to the equivalent loads. The stiffness matrix is post-multilied by a displacement transformation matrix, and pre-multiplied by the corresponding force transformation matrix. This force transformation matrix is nothing more than

the transpose of the displacement transformation matrix. A detailed formulation of the process is given in the appendix A.

3.3 Mesh Generator

3.3.1 General

Once all the features required for any finite element analysis are implemented in a finite element computer program, it remains to prepare input data for the description of the structure. Preperation of input data consists of discretization of the given structure into a suitable mesh using well defined elements connected at node points. The node and element numbering, and the tabulation of coordinates and incidences are the major portions of the data preparation.

In case of two dimensional structures the task of discretization is relatively easy compared to that for three dimensional structures, as it is possible to draw an exact diagrammatic representation of the two dimensional structure on a plane. Then, coordinates of the node points can be directly retreived by measurement or by using an electronic digitizer.

However, when the structure is not only three dimensional but at the same time has the added complexity of being curved in space as in the case for the cylinder intersection, discretization poses a formidable task. Any attempt to achieve a solution manually would not only consume several man days but it would also be highly error prone.

An early attempt was made by Greste (2.43) to develop a mesh generation algorithm using the technique of conformal mapping. This algorithm was restricted to use on cases where only shell elements modeled the entire structure. The problem becomes significantly more complex when more than one layer of three dimensional elements are used through the thickness particularly if that occurs over only a part of the structure. Also a feature providing the capability of reinforcing around the curve of intersection by some additional material was not incorporated in Greste's algorithm.

In this study a very generalized computer algorithm is developed for the discretization of intersecting cylinders. Simple input parameters are designed to describe the geometry and control the discretization process. The description of the capabilities and limitations of this program along with various options and operations are listed briefly in the rest of this chapter. The required input parameters and their default values are described in appendix B.

3.3.2 The Curve Of Intersection

The curve of intersection of two cylindrical surfaces is very complex in its nature. This curve can be located in cartesian coordinates by a variable, ϕ , the angle of sweep on the plane normal to the axis of the intersecting cylinder Fig. 2.1. In the general case with an angle of intersection between the two axes of rotation, the curve of intersection can be represented as:

$$X = r \sin \phi$$

$$Y = R \cot \alpha + R \cos\phi \sin\alpha -\{R(1-m)-\gamma\cos\phi\cos\alpha\} \cot\alpha$$

$$Z = R + m$$

where $m = \sqrt{1-(\gamma/R)\sin\phi}$ (3.6)

The shape of the curve varies considerably depending upon the angle α and upon the aspect ratio γ/R , Fig.3.6, thereby significantly increasing the task of generalizing the mesh generation.

3.3.3 Reinforcement

In the mesh generating routine, provision is kept to introduce the reinforcement in the geometry specified by the user. Three basic configurations of reinforcement are enough to describe, by proper combination, any practical reinforcement pattern. These basic configurations are, on the outside of intersecting cylinder, on the outside of the intersected cylinder and on the inside of the intersected cylinder Fig 2.2 .

The reinforcement length, thickness, and number of elements are specified by the user. To avoid any sudden discontinuity at the end of the reinforcement, it is provided with an inclined edge with the angle of inclination varying according to the users' specifications.

3.3.4 Discretization of Nozshell

The boundary between Nozshell and Solid is decided by the computed generator lengths. At the sweeping angle, ϕ = 0, 90 and 180 degrees, Fig. 2.1, the generator lengths in the region of stress concentration, are computed by multiplying the stress decay factors, specified by the user, by $2.45\sqrt{r*t}$. The length of the transition zone is also added to get the final lengths of the generators in the region Solid. Intermediate generator lengths are measured by interpolation.

In the region Nozshell, the stress field is dominated by membrane stresses. As the stress gradient in this region is very shallow, a refined mesh is not needed. Ahmad shell elements are used for this substructure. Nozshell is divided, by generators and rings, into a grid as shown in Fig. 3.1. The number of elements around the circumferential direction is decided on the bases of the desirable aspect ratio set for the solid elements in the region of stress concentration.

The lengths between the rings in the axial direction is based on the aspect ratio of the shell elements, specified by the user. The longest generator is divided into intervals in the axial direction so that all the subdivided lengths are within the limits of the aspect ratio times the distance between the generators.

As it is expected that the number of elements should be more in the axial direction than in the circumferential direction, to minimize the band width, the node and the element numbering is done in the circumferential direction starting from the top edge.

I

The structure Nozshell is condensed keeping the nodes only on the bottom edge, that is the edge connecting Nozshell to the rest of the structure.

3.3.5 Discretization of Solid

The region can be subdivided into two subregions, the intersecting cylinder, called here as Nozsol, and the intersected cylnder, Cylsol. This part of structure is composed of three dimensional isoparametric elements and transition elements. The layering arrangements used are shown in Fig. 3.5. Four distinct cases are considered.

Grid case (i) *One layer of 20 noded three dimensional* isoparametric elements through thickness.

Grid case (ii) **Two layers of 20 noded three dimensional** isoparametric elements through thickness.

Grid case (iii) One layer of 16 noded three dimensional isoparametric elements through thickness.

Grid case (iv) **Two layers of 16 noded three dimensional** isoparametric elements through thickness.

More than two layers of elements through thickness is not only economically infeasible but also the additional elements do not contribute to a significant increase in accuracy.

3.3.5.1 Nozsol

The mesh generation in this region is done in two steps. A reference grid is prepared on the midsurface based upon various parameters specified by the user. Once the grid is ready the three dimensional elements are built on that grid in the required number of layers.

The top two rows of elements in Nozsol consist of transition elements with the transitional shell element in the first row. The second row is made up of the three dimensional transitional element except for grid case (iii). The length of this transition zone varies between 2 and 15 times the minimum dimension of the solid elements in order to achieve a smooth transition in the generator lengths in Nozsol.

The rest of the zone consists of rows of three dimensional elements in the specified number of layers.

The shape and characteristics of this zone is very flexible. It is possible to specify the length of this zone by stress decay factors. Also the number of rows are flexible, varying from 4 to 8. The lengths of the various rows of elements in the axial direction are controlled by a proportionality ratio, specified by the user.

If reinforcement type one or two is provided the lengths of the rows of elements are readjusted depending on the number of elements specified in the reinforcement. The summation of the lengths of these readjusted rows is equal to the length of the reinforcement of type one or thickness of the reinforcement of type two. Again the individual lengths of these elements in the

axial direction is governed by the proportionality ratio.

The coordinates on the curve of intersection are obtained by using Eq. 3.6.

The nodes and the element numbering starts from the top edge where the condensed substructure Nozshell is connected. The sequence in node numbers is carried out first from the inside to the outside through the thickness, next in the circumferential direction and then in the axial direction.

3.3.5.2 Cylsol

The opening in Cylinder is on the circumference, hence unlike Nozsol the region has to be divided into a more complex grid. Generators can not be used to form a grid in this case. To simplify the task then, the coordinate system S-Y is introduced. The 'S' coordinate is the circumferential distance on the midsurface of the cylinder from the generator having the maximum value of Z, Fig. 2.1. Under this new coordinate system Cylinder can be visualized as unfolded on to a plane. As in the case of Nozsol, mesh generation is done in two steps. A reference grid is prepared and then the three dimensional elements are built on that grid in the required number of layers.

The reference grid is easier to prepare on the pseudo plane, S-Y, by dividing the zone in radial and tangential directions around the opening, with a smooth transition in the lengths of the elements in the radial direction. This zone contains four rows of three dimensional isoparametric elements in the radial direction. The lengths of the various rows in the radial

direction is controlled by the proportionality ratio.

If reinforcement is provided, the number of rows of elements is readjusted depending upon the specified number of elements in the reinforcement. The total lengths of these readjusted rows depends on the lengths of the reinforcement for types 2 and 3 and on thickness for type 1. The division of this readjusted zone in the radial direction also must obey the proportionality ratio. If reinforcement types 2 and 3 are provided at the same time, the length of reinforcement type 3 would be based on the number of elements specified for it, as the configuration of elements depends on the parameters specified for reinforcement type 2.

The nodes and the element numbering in this zone are in a continuation from Nozshell, and hence the increment scheme is similar to that of Nozshell.

3.3.6 Discretization of Cylshell.

The structure other than Solid, of the intersected cylinder is considered as Cylshell. Once the boundary of Solid and Cylinder is established, then it is possible to divide this zone into a regular grid formed by generators and rings, Fig. 3.1. The reference points on this boundary are obtained from the reference grid of the substructure Cylsol.

This zone is dominated by membrane stresses with but a small stress gradient. Ahmad shell elements are used in this substructure. Their aspect ratio is set smaller or equal to the users specification.

Node and element numbering are started from the end with maximum Y coordinate at the generator with maximum Z coordinate. The increment in the numbering is carried out first in circumferential direction and then in the axial direction. The structure Cylshell is condensed keeping the nodes only on the edge connecting it to the rest of the structure.

4. FATIGUE

4.1 Introduction

The failure of metals, when subjected to repeated or cyclic loads, became a recognized engineering problem, with the introduction of rotating or reciprocating machinery during the industrial revolution of the early 1800s. Metals were observed to fail in a brittle manner, at a load level previously considered safe. The first documentation of this phenomenon is dated 1829 by Albert in Germany. Since then, extensive research on metal fatigue has been carried out. The researchers involved come from such diversified fields as physics, Metallurgy, Mechanics and Engineering. Efforts have concentrated on determining the nature of fatigue damage, as well as methods for coping with it in design.

In 1963 Gohn (4.1), after reviewing a number of theories, concluded that fatigue is the consequence of uninhibited fine slip which gradually becomes intensified and finally develops into a crack. This crack then propogates until the remaining cross section is too small to carry the load, with the result that a cataclysmic failure occurs. Morrow (4.2), modified the above deduction by dropping the prefix "un" from the word uninhibited to explain the role of plastic strain in fatigue.

The theory of fatigue is explained by physicists in terms of dislocations and slips within the atomic lattice. Improvements

in the material fatigue properties have been primarily due to physicists and metallurgists. It remains to mechanics to derive the fatigue properties and to study the metal behavior under various environments. Engineers are provided with the characteristic properties of various metals. It is up to them to design the structural component effectively along with a proper selection of the material to reduce the risk of a fatigue failure.

The microscopic mechanism of fatigue is beyond the scope of this research and hence no details are given here. A specific study of fatigue life in the environment of a shell intersection is carried out for the purpose of improving the understanding of fatigue for this kind of structures. To understand the fatigue phenomenon, it is important to study the cyclic behavior of metals defining certain parameters, which are characteristic to any metal under cyclic load.

4.2 Cyclic Stress Strain Behavior of Metals

For a material exhibiting only elastic response under the action of the applied loads, the stress strain curve is a straight line, ie the stress strain response of the material is completly retraceable and the strains are completly recoverable. During plastic flow, the complete load cycle produces a hysteresis curve that reflects both elastic and plastic deformations. The detailed explanation of this behavior is described in chapter 5.

The area contained within the hysteresis loop presents a measure of plastic deformation work done on the material. Some of this work is stored in the material as cold work while the remainder is emitted as heat.

It is important to recognize that fatigue damage occurs only when cyclic plastic strains are generated. This is not to be misconstrued, however, as implying that whenever applied nominal stresses are below the material yield strength no fatigue results. Flaws in the material or stress concentrations can elevate local stresses resulting in an associated strain in the plastic range.

With progression of the load cycle most materials reflect changes in the shape of the hysteresis loop. These changes continue until the material reaches cyclic stability. The material can cyclically harden, soften or even display a mixed behavior. Under stress controled conditions, the width of the hysteresis loop contracts with cyclic hardening and expands during cyclic softening. Cyclic softening is a severe condition, leading to an early failure.

Most metals, after cycling with a constant strain amplitude for a relatively short duration (4.3,4.4), stabilize to a steady hysteresis loop. The locus of the tips of such cyclically stabilized loops, for various amplitudes of strains, presents a curve known as a cyclic stress strain curve. Fig. 4.1. The cyclic stress strain curve is used to find the material's fatigue properties. Also the local stress strain curve in a structure subjected to cyclic loads, is obtained from the constitutive

relations based on this curve to study its stabilized response.

A number of methods (4.5,4.6) exist for the determination of the uniaxial cyclic stress strain curve.

4.3 Fatigue Life Analysis

The fatigue life generally is defined as the number of load reversals to develop a crack of visible length. Life, when used in this context, means reversals to crack initiation plus some early growth.

Many theories have been proposed to predict the fatigue life of a component. The experimental and theoretical work associated with many of these theories was recently reviewed by Brown and Miller (4.8), and by Krempl (4.9).

Two basic approaches exists for the prediction of fatigue life, viz. the experimental approach and the numerical approach. In the experimental approach the component under investigation is subjected to a simulated field condition of load reversal in a controled laboratory environment. The region of stress concentration is closely watched for the initiation and propogation of a fatigue crack. After statistical study of several such experimentations the fatigue life of the component is predicted for the required probability level of failure. Though the accuracy of the experimental approach is commendable, it involves the resources which are beyond the scope of this investigation. Hence in this study the second approach is considered.

According to the present "state of the art", the numerical approach for the prediction of fatigue life of a component can be catagorized into two methods. In the first method, the relationship between the fatigue life and the plastic deformation work is established. For this purpose laboratory tests are conducted on polished cupons subjected to uniaxial load cycles of various intensities (4.10). A curve of the fatigue life versus plastic deformation work is plotted from these test results. To predict the fatigue life of a component, the dissipated plastic deformation work is numerically evaluated for the given amplitude of loading. The life is then predicted depending upon the total dissipation of the energy per load cycle (4.11). It should be noted that results obtained using this method display inconsistancies with experimental results. Furthermore no proven theory substantiate this approach.

The most widely accepted and used approach to predict fatigue life is to find a set of local equivalent stress and strain values and relate them to experimental values obtained from uniaxial test results (4.12,4.13). In this study this second method is used for the purpose of establishing a life prediction for the cylinder intersection problem.

Fatigue life of a material can be characterized by a strain amplitude versus life curve. This curve can be determined from polished laboratory specimens, tested under a history of complete reversal of strain. Coffin (4.14) and Mason (4.15) were the pioneers in expressing the relationship between plastic strain amplitude and fatigue life by a simple power function. The

plastic strain amplitude, $\Delta\varepsilon p/2$, is related to fatigue life, $2N_f$, according to equation:

$$\frac{\Delta\varepsilon_p}{2} = \varepsilon_f' \ (2N_f)^c \qquad (4.1)$$

To account for the total strain amplitude, the elastic component of the strain remains to be considered. The relationship between elastic stress amplitude and fatigue life was first suggested by Basquin (4.16) in the following form :

$$\frac{\Delta\sigma}{2} = \sigma_f'(2N_f)^b \qquad (4.2)$$

In the elastic zone Hook's law applies, therefore :

$$\frac{\Delta\varepsilon_e}{2} = \frac{\sigma_f'}{E} \ (2N_f)^b \qquad (4.3)$$

Total strain amplitude is equivalent to the summation of its elastic and plastic components, hence :

$$\frac{\Delta\varepsilon}{2} = \varepsilon_f'(2N_f)^c + \frac{\sigma_f'}{E} \ (2N_f)^b \qquad (4.4)$$

For the purpose of a fatigue analysis we need to know the material characteristics listed below.

ε_f' True fracture ductility

σ_f' True fracture strength

b   Fatigue strength exponent

c   Fatigue ductility exponent

Many techniques to estimate these fatigue properties are documented by Landgraf (4.6). Over the years, experiments have been performed on various materials to collect these properties in data banks (4.7).

4.3.1 The Effect of Mean Stress and Mean Strain

In all the above discussion it has been assumed that cyclic stress and cyclic strain were completely reversible with respect to the virgin stress strain state of the material. However this is seldom the case. In most problems, loading is associated with certain values of mean stress, σ_m, and/or mean strain, ε_m. Mean stress and strain under certain situations can significantly alter the fatigue life of the material.

A tensile mean stress causes severity by opening a crack, causing high stress concentrations at the crack tip. The crack might be a pre-existing flaw or a freshly nucleated fatigue crack. Hence a tensile mean stress tends to reduce the fatigue life of a component while a compressive mean stress has a reverse effect. It closes any microcracks thereby helping to extend the fatigue life.

The effect of mean stress σ_m has been quantified by Morrow (4.17), as :

$$\frac{\Delta \varepsilon}{2} = \varepsilon_f' (2N_f)^c + \frac{\sigma_f' - \sigma_m}{E} (2N_f)^b \qquad (4.5)$$

The mean strain reduces the fatigue life by exhausting some of the ductility available in a virgin material (4.18). This regressive effect of mean strain, ε_m, can be expressed in a fatigue life equation as (4.19):

$$\frac{\Delta \varepsilon}{2} = (\varepsilon_f' - |\varepsilon_m|) (2N_f)^c + \frac{\sigma_f' - \sigma_m}{E} (2N_f)^b \qquad (4.6)$$

4.3.2 Multi-axial Stress Field

All the previous discussion was based on the assumption that the stress field was uniaxial. However, all the derived equations can be extended to multi-axial stress fields with due modifications. For this purpose an analogy can be drawn with equivalent plastic strain in plasticity theory (4.12).

As in plasticity theory, equivalent strain is obtained by combining the principal strain components as :

$$\bar{\varepsilon}_e = [\frac{\sqrt{2}}{3} \{ (\varepsilon_1 - \varepsilon_2)^2 + (\varepsilon_2 - \varepsilon_3)^2 + (\varepsilon_3 - \varepsilon_1)^2 \}^{1/2}] \qquad (4.7)$$

whereas equivalent stress is obtained by :

$$\bar{\sigma}_e = [\frac{1}{\sqrt{2}} \{ (\sigma_1 - \sigma_2)^2 + (\sigma_2 - \sigma_3)^2 + (\sigma_3 - \sigma_1)^2 \}^{1/2}] \qquad (4.8)$$

Equivalent stress and strain values are calculated at the maximum and the minimum load level of a cycle. From these values equivalent amplitudes and mean values of stress and strain are calculated. It should be noted that the values of equivalent stress and strain are always positive. Hence it is important to find the position of the stress and strain points on the pai plane to recognize their tensile or compressive nature. The pai plane is a plane normal to the hydrostatic axis in the Haigh-Westergaard stress space.

The equivalent range of strain obtained in the above fashion is applicable under the following assumptions :

(a) All stresses are in phase or out of phase by 180 degrees. ie. σ_1 , σ_2, and σ_3 achieve their highest or lowest values at the same time, or when one reaches its minimum value the rest achieve their maximum values.

(b) The elastic component of strain is small compared to the plastic component. However restrictions imposed by this assumption could be waived by multiplying the elastic characteristics of the strain-life curve by a constant w defined as :

$$w = \frac{2}{3}(1 + \nu) \tag{4.9}$$

Eq. 4.6 can then be modified to read as :

$$\frac{\Delta \epsilon}{2} = (\epsilon_f' - |\epsilon_m|) \ (2N_f)^c + \frac{w(\sigma_f' - \sigma_m)}{E}(2N_f)^b \tag{4.10}$$

The first assumption puts some restrictions on the applicability of this analogy in a very general sense. However, in most practical cases, the phase relation among the strains is either 0 or 180 degrees, thus questions regarding the validity of the procedure rarely arise.

4.3.3 Cycle Counting and Cumulative Damage

The purpose of present investigation is to study the general fatigue behavior of the cylinder intersection. Hence for ease, simple load cycle with constant amplitude of loading is considered. However, it is possible to extend this study for the inclusion of more complex loading situations. The loading can be combinations of small reversals on top of large peak values. This type of loadings are considered as a combination of hysteresis loops of different amplitudes. Fatigue life in loading cases like this, can be predicted by obtaining the number of cycles of load reversal a structure is capable of sustaining for each hysteresis loop. Hence, some technique to count the cycles of loading corresponding to each loop is essential.

Common cycle counting techniques in use today are the peak-range, the range-pair and the rain flow. Of these the rain flow (4.20) has been shown to be superior. It yields the best fatigue predictions (4.21). The apparent reason for the superiority of the rain flow counting is due to the fact that it combines load reversal in a manner which defines a cycle as a closed hysteresis loop.

The fatigue process of a material is due to the combination of the imposed loading, which could be looked on as an accumulation of damage toward a maximum tolerable limit. The total damage caused by each load loop can be determined by a linear damage concept, such as the well known Miner's rule (4.22). This rule says, fatigue failure occurs when the summation of damage caused by each amplitude of loading is equated to one. In this context the damage for any particular load is defined as the ratio of actually performed number of cycles, n_i , at that load level, divided the single level fatigue life, N_i , for the same amplitude of loading. Mathematically, the damage, D_i , for loading amplitude i is :

$$D_i = n_i/N_i \qquad (4.11)$$

Fatigue failure then occurs when :

$$\Sigma D_i = 1 \qquad (4.12)$$

4.4 The Fatigue Life of Cylinder Intersection

In this analysis the failure is considered at the point when a fatigue crack of visible length is developed. The time taken for the propogation of the crack is not considered. In shell structures, like the pressure vessel intersection, once the fatigue crack nucleats, the propogation is rather rapid. Hence the structure can be considered to have failed once the crack

initiates.

The following steps are followed then to find the fatigue life of the cylinder intersection :

1. The selection of a material is made from within the range of material specifications set by ASME. Here, the selection is based on the ductility requirement of the structure as large localized strains are expected. For this purpose a mild steel, SAE1015, is selected. The properties of this material are shown in Figs. 4.1 and 4.2.

2. The strucutre is analyzed for the given loading history. In case of constant amplitude load reversals, only half load cycle is enough to evaluate amplitudes *and mean values of local* stresses and strains. The characteristics of cyclic stress-strain curve are considered for the purpose of the analysis.

3. Values of equivalent stress range, equivalent strain range, equivalent mean stress and equivalent mean strain are evaluated at the most vulnerable point on the structure.

4. A strain-life curve is plotted using Eq. 4.10, after proper substitution of equivalent mean stress and equivalent mean strain values. From the computed equivalent strain amplitude the fatigue life of the component is found utilizing the strain-life curve.

In this discussion the effect of various other factors, which can alter the fatigue life, are not considered. These

factors include residual stresses, temperature, environment and metallurgical aspects like peening, tempering, etc. Consideration of these variables is out of scope of this study.

5. MATERIAL NONLINEARITY

5.1 Introduction

Investigation of structural response, including consideration of nonlinear material behavior, was first thought of and documented, as early as 1864, by Tresca. However, due to the size of calculation efforts involved solution for even a simple structure was difficult. It is only in the last ten years, that the thrust for this kind of problem has become significant.

For the viability of any stress computation technique and design procedure, two main aspects are of utmost importance- viz. Usability and Accuracy. The cost of computation is decreasing, as faster and more efficient computers are being developed with impressive hardware and software capabilities. Numerical analysis techniques which just a few years ago had seemed totally impracticable because of the computational effort and costs involved are now becoming almost an every day routine.

5.2 Material Response Idealization

If the material response is to be limited so as to remain within the elastic state, then for most materials a linear idealization using Hook's law can be applied. The solution technique for this kind of structural response is well established.

However, once the material response crosses the boundary of the elastic zone, then more complex idealizations are needed. The consideration of an isotropic hardening law to account for nonlinear behavior is sufficient for a structure subjected to only monotonically increasing loads (5.1). Under cyclic loading conditions, however, the isotropic hardening law gives inaccurate results as it ignores the Bauschinger effect. According to isotropic hardening, with constant load amplitude, the stress strain curve shakes down to a linear response after the first reversal of the loading. Fig. 5.1.

A kinematic hardening model was devised to account for the Bauschinger effect under load reversal (5.2). For a material idealized with kinematic hardening and subjected to constant amplitude load reversals, the stress strain curve stabilizes in a constant loop at the end of the first loading cycle. Fig. 5.2.

The response of an actual material is different than those predicted by either of the hardening laws. Most virgin materials have a transitional zone in the earlier stages of cyclic response. Depending upon their inherent characteristics, they either cyclically harden or soften, eventually however stabilizing in a constant loop. The stabilization of most materials is achieved at approximately the end of half of their fatigue life (4.2).

Recently efforts have been directed to incorporate this transitional material behavior in the material models by combining isotropic and kinematic hardening (5.3). However, a difficulty developes in deciding the percentage contribution of

each type of hardening. There is no established method for predicting the split. The result is to resort to a trial and error approach, comparing the results with experimental values. Moreover, when a structural analysis is aimed at the prediction of fatigue life, a mixed hardening law would necessiate the continuation of the analysis until the structural response shakes down to a stable loop. Nonlinear finite element analysis is a very effective tool but at the same time it is not an inexpensive computation. Its use should be invoked based on proper judgement and rationality. It should not be simply turned loose in the hope of overcoming a lack of knowledge.

In the present study the cyclic stress strain curve is utilized, along with kinematic hardening, to study the stress patterns in the structure. The structure is subjected to only one reversal of loading. The objective is to evaluate the stress amplitudes for the purpose of predicting fatigue life.

In the subsequent parts of this chapter various aspects of material idealization are described in detail.

5.3 Yield Criteria

A material subjected to monotonically increasing load, initially linearly relates its stress to strain quantities up to a certain stress magnitude. This limit is called the proportional limit. Stressing of the material beyond this point causes both recoverable and irrecoverable deformations. This stress magnitude is sufficient to define the yield point for a uniaxial stress field.

However, for the case of multiaxial stress fields, yielding is more complex to define. Various physical phenomena observed over the years by many researchers are primarily responsible for the current definition of the condition of yield. It is well known that any attempt to describe all materials by means of a single criterion can hardly be expected to meet with success. The three most widely used criteria for materials ranging from metals, concrete, and soils to composite materials, are the Huber-Mises, the Tresca and the Mohr-Coulomb yield criteria.

In this work, it is decided to use the Huber-Mises yield criterion with some required modifications. This criterion is reasonably representative of the behavior of the material under consideration viz. steel.

5.3.1 Huber-Mises Yield Criteria

The Huber-Mises yield criteria is based on two simple postulations. (i) Yielding does not occur in a material subjected to a hydrostatic stress field; and (ii) For yielding the energy causing distortion should be the same for uniaxial and multiaxial stress fields.

The strain energy in the body under a multiaxial stress field can be written as:

$$U = \frac{1}{2} \sigma_{ij}\epsilon_{ij} \qquad (5.1)$$

This energy equation can be rewritten in terms of stress invariants as :

$$U = \frac{2G+3\lambda}{6} (I_1^2 - 3\alpha \, T \, I_1) + 2G \, J_2 \tag{5.2}$$

I_1 represents the spherical state of stress, whereas J_2 is an invariant of the deviatoric stress. Hence the above equation can be considered as a combination of two parts. The first term is the energy involved in changing the volume of the body, and the second term is the energy of distortion.

For the uniaxial case $J_2 = \frac{1}{3}\sigma_o^2$, hence from the second postulation:

$$\frac{1}{2}[(\sigma_1-\sigma_2)^2 + (\sigma_2-\sigma_3)^2 + (\sigma_3-_1)^2] = \frac{1}{3} \sigma_o^2 \tag{5.3}$$

In general we can write this relationship in the well known form as :

$$f(\sigma_{ij}) = \sigma_y(K) \tag{5.4}$$

Eq. 5.3 represents the Huber-Mises yield condition for a multiaxial stress field. Physically this equation represents a surface in the stress field. By the introduction of a stress space characterized with the principal stresses as coordinate axes, visualization of a yield surface becomes quite simple. This stress space is known as the Haigh-Westergaard stress space (5.4). In this stress space, Eq. 5.3 represents a circular cylinder of radius equal to $\sqrt{2/3} \, \sigma_o$ with its axis equally inclined to all the three coordinate axes. Fig. 5.3.

When the stresses at a point in the material are inside the cylinder, only elastic deformation of the material occurs. Plastic strains start only when the stresses at a point locate that point on this cylindrical yield surface.

5.4 Hardening Laws

Once yielding has begun further stressing of the structure causes changes in the yield surface. Different sets of criteria have been devised to monitor this change. These criteria are called Hardening laws.

5.4.1 Isotropic Hardening

Hill (5.5) introduced the idea of isotropic hardening, stating that as yield progresses the yield surface expands uniformly in all the directions. The subsequent yield surface can therefore be written as:

$$F = f(\sigma_{ij}) - \sigma_y(K) \tag{5.5}$$

where $\sigma_y(K)$ is a function of plastic deformation and the history of the stress path.

For the Huber-Mises yield criterion the subsequent yield surface is a concentric cylinder with the same axis of rotation and with a radius $\sigma_y(K)$. This criteria does not take into account the Bauschinger effect, thereby, introducing some errors in its use for a structure subjected to cyclic loading.

5.4.2 Kinematic Hardening

Prager (5.2) introduced the idea of a kinematic hardening model. This model accounts for the Bauschinger effect. As yielding progresses, the total elastic range is maintained constant by translating the yield surface without deforming it. The subsequent yield surface can now be written as:

$$F = f(\sigma_{ij} - \alpha_{ij}) - \sigma_o \qquad (5.6)$$

where σ_o is a constant and α_{ij} represents a second order tensor indicating the instantaneous center of the yield surface in a stress space.

Prager suggested that translation of the yield surface is in the direction of the plastic strain increment. Though Prager's hardening rule observes the Bauschinger effect, it is not invariant with respect to the reduction in dimensions possible in almost any application, Perrone and Hodge Jr. (5.6).

To avoid this kind of inconsistancy in problems with two dimensional stress fields Ziegler (5.7) suggested the yield surface should be translated in the direction of the radius connecting the instantaneous center with the stress point. Mathematically this can be represented by the equation:

$$d\alpha_{ij} = (\sigma_{ij} - \alpha_{ij}) \, d\mu \qquad (5.7)$$

where α_{ij} is the instantaneous center of the yield surface and $d\alpha_{ij}$ is the translation of that yield surface Fig. 5.5. $d\mu$ is

a scalar quantity greater than zero reflecting the hardening variation.

Ziegler's hardening rule was generalized by Mroz (5.8) who introduced the concept of the field's work hardening moduli. The nonlinear uniaxial stress strain curve is divided into linear segments, each segment having a different hardening coefficient. In the Haigh-Westergaard stress space this is represented by a set of concentric cylinders, with the space between them indicating the field of differing work hardening moduli. The material model used in the present research is based on this postulation. It is described in detail in section 5.6.

To complete the basic theory of incremental plasticity the third important rule to be considered is the flow rule. This rule describes the relations between stress and strain, once yielding has begun.

5.5 Constitutive Relation

In the plastic range of material response, stresses are not uniquely determined from strains by a simple relationship such as that of Hook's laws for the elastic range. In the plastic range there can be different values of stress for the same value of strain, depending upon the whole history of loading that has gone on prior to reaching that particular state of strain.

The relationship between stress and strain in the plastic range can be derived from four basic postulations. These postulations are due to Drucker (5.9). They insure the uniqueness of the stress for a given loading history and strain. They also

define the stability of a material, which in a uniaxial sense, is a material for which stresses are monotonically increasing functions of strain.

Drucker proposed that an external agency which slowly applies an additional set of stresses on a material and then slowly removes them, during which time the material remains in equilibrium, (i) positive work is done by the external agency and also (ii) the net work done by the agency over the cycle of application and removal is zero or positive. In the mathematical terms:

$$d\sigma_{ij}(d\epsilon_{ij}^e + d\epsilon_{ij}^p) > 0 \tag{5.8}$$

and

$$d\sigma_{ij}\, d\epsilon_{ij}^p \geq 0 \tag{5.9}$$

Eqs. 5.8 and 5.9 constitute the first two assumptions, describing the characteristics of a stable material. Two more assumptions are required for establishing the constitutive equations.

It is assumed that as in fluid flow, a potential loading function exists. At any stage of loading a function $f(\sigma_{ij})$ exists so that plastic deformation will take place only if $f(\sigma_{ij}) > 0$, where $f(\sigma_{ij})$ depends upon the state of plastic strain and the loading history. If this potential function is considered to be the same as the yield function, it is called an associative flow rule.

Lastly, it is assumed that the relationship between infinitesimals of stress and plastic strain is linear ie:

$$d\varepsilon_{ij}^{p} = C_{ijk\ell} \; d\sigma_{k\ell} \qquad (5.10)$$

With these four basic assumptions, Drucker showed that the incremental stress and strain relationship in the plastic range can be written as :

$$d\varepsilon_{ij}^{p} = G \; \frac{\partial f}{\partial \sigma_{ij}} \; (\frac{\partial f}{\partial \sigma_{ij}} \cdot d\sigma_{ij}) \qquad (5.11)$$

where G is a scalar which depends upon the stress strain relationship and the loading history.

It is interesting to note that Drucker's derivation implies that the plastic strain increment is normal to the yield surface. This normality is rather imposed than proven. This normality condition may not be true for materials like soil where softening takes place, but for metals normality does give satisfactory results.

By considering the Huber-Mises yield condition as the loading potential in Eq. 5.11 it can be shown that :

$$d\varepsilon_{ij}^{p} = d\lambda \; S_{ij} \qquad (5.12)$$

where
$$d\lambda = G \cdot df$$

and S_{ij} are the components of the deviatoric stress. Eq. 5.12 is also called the Prandtl-Reuss equation (5.10,5.11) for the incremental constitutive equation of plasticity.

5.6 Material Model

As described in this study a material model is a mathematical simulation of the physical behavior of a material when subjected to various stress fields. The material model developed in this work is based on a kinematic hardening concept. The Huber-Mises yield criteria is used along with the modifications suggested by Mroz. An incremental Prandtl-Reuss equation is utilized to represent the constitutive relation.

Consider a material whose stress strain curve under a uniaxial stress field is represented by a linear segmental idealization, Fig. 5.4. This curve consists of n linear segments having tangent moduli E_1 , E_2 ,....,E_n corresponding to stress ranges σ_o^1 , σ_o^2 ,...., σ_o^n . This uniaxial stress strain curve is represented in multiaxial stress space by concentric hyper-surfaces located by equations of the form :

$$F = f(\sigma_{ij} - \alpha_{ij}^n) - \sigma_o^n \qquad (5.13)$$

The region between each curve represents a field with a constant work hardening modulus. For an initial isotropic material all these surfaces are concentric. In the case of a two dimensional stress field the yield surface is represented by a circle, Fig. 5.4.2, which is easy to portray diagrammatically. Hence for ease of visualization the subsequent explanation is directed to two dimensional stress field. However, all the discussion is also true for a three dimensional stress field.

5.6.1 Surface Translation

The translation of the hyper-surfaces can best be explained by considering a case with nonproportional loading. Within this case the material is subjected to an arbitrary stress field, as shown in the Fig. 5.6. The stress conditions are such as to place the stress point at L. If the material is subjected to further stressing, the hyper-surface f_n translates in the direction of point M on the outer surface f_{n+1}. Point M has the same outward normal direction as that for surface f_n at stress point L. It should be noted that by restricting the translation of the hyper-surfaces in the direction to the point on the outer surface having the same normal we are eliminating the possibility of an intersection of the surfaces. The surfaces can only move by pushing the outer surface once it touches the latter. During this translation they keep the same point of contact.

5.6.2 Loading

Consider a structure subjected to a monotonically increasing load which induces a uniaxial stress field. Stresses at the given point increase while obeying Hook's law until first yield is reached. Schematically in Fig. 5.4 the stress point moves from the origin along the vertical axis until it reaches the elastic limit at point A on hyper-surface f_1. On further loading the stress point moves from A to B. Correspondingly the hyper-surface f_1 translates along the vertical axis until it touches the hyper-surface f_2 at point B. The rate of the translation of hyper-surface f_1 with the stress point up to

surface f_2 is governed by the tangent modulus E_2 of the surface f_1. On further application of stress, ranging from B to C, hyper-surfaces f_1 and f_2 now translate together, keeping the same point of contact, and moving along the vertical axis until they touch hyper-surface f_3. During this translation in the stress field between f_2 and f_3, the rate of translation is governed by E_3. And so on.

It is interesting to note the assumption made here that all surfaces are allowed to translate in stress space without changing their shape or orientation. Also when the inner surfaces containing the stress point are moving, all the outer surfaces remain stationary.

5.6.3 Unloading

This situation is explained as the continuation of the loading case of the previous section. If loading is reversed after reaching the stress state portraied at point C, the stress point will move back inside the surface f_1, Fig. 5.4. During this reversal all the surfaces remain stationary until the stress reaches point D. Under further unloading, a process exactly similar to that executed during loading starts. Once the stress state exceeds D, reverse plastic flow occurs, translating the surface f_1, downward until it touches surface f_2 and so on. With continued unloading up to stress state G, the developed configuration of the surfaces is exactly the same as that of stress state C, but on the opposite side of the origin.

In the present study the outermost hyper-surface is assumed to be representative of a point of infinite yield. The work hardening modulus for this surface is zero representing a perfectly plastic situation. Once the stress point reaches this surface, on further loading, the surface does not translate but the point slides along this surface.

5.6.4 Mathematical Representation

Once the physical behavior of the material model is understood schematically, it becomes much easier to represent that behavior mathematically. For an isotropic virgin material the initial yielding is assumed to be governed by the Huber-Mises criteria expressed as :

$$f(\sigma_{ij}) - \sigma_y^n(K) = 0 \qquad (5.14)$$

The subsequent yield function or loading function after the first yielding may be written as :

$$f(\sigma_{ij} - \alpha_{ij}^n) - \sigma_y^n(K) = 0 \qquad (5.15)$$

where α_{ij}^n denotes the instantaneous center of the yield surface n.

For two yield surfaces, n and n+1, the vectors joining their instantaneous centers to the points of the equidirectional normals are parallel Fig. 5.6. Denoting the stresses at these two points as σ_{ij}^n and σ_{ij}^{n+1} we can therefore say that :

$$\sigma_{ij}^{n+1} - \alpha_{ij}^{n+1} = \frac{\sigma_y^{n+1}(K)}{\sigma_y^n(K)} \cdot (\sigma_{ij}^n - \alpha_{ij}^n) \tag{5.16}$$

Also the translation of the yield surface is given by :

$$d\alpha_{ij}^n = d\mu \ (\sigma_{ij}^{n+1} - \sigma_{ij}^n) \tag{5.17}$$

where $d\mu > 0$ is a scalar. On substituting Eq. 5.16 into Eq. 5.17 and rearranging, that equation can be rewritten as :

$$d\alpha_{ij}^n = d \ \mu \{ \frac{\sigma_y^{n+1}(K)}{\sigma_y^n(K)} \ (\sigma_{ij}^n - \alpha_{ij}^n) + \alpha_{ij}^{n+1} - \sigma_{ij}^n \} \tag{5.18}$$

The scalar $d\mu$ is obtained from the condition that the stress point remains on the yield surface during plastic flow, thus :

$$(d_\sigma ij - d\alpha ij) \ \frac{\partial f}{\partial \sigma_{ij}} = 0 \tag{5.19}$$

Substituting the result of Eq. 5.18 into Eq. 5.19 and again rearranging the terms yields :

$$d\mu = \frac{\frac{\partial f}{\partial \sigma_{ij}} \ d\sigma_{ij}}{\frac{\sigma_y^{n+1}(K)}{\sigma_y^n(K)}(\sigma_{ij}^n - \alpha_{ij}^n) + \sigma_{ij}^{n+1} \} \ \frac{\partial f}{\partial \sigma_{ij}}} \tag{5.20}$$

This equation quantifies the translation of a hyper-surface for a stress increment of value $d\sigma_{ij}$.

To complete the definition of the material behavior it is essential to consider a flow rule. From Eq. 5.12 :

$$d\epsilon_{ij}^{b} = \frac{\partial f}{\partial \sigma_{ij}} d\lambda \qquad (5.21)$$

where $d\lambda > 0.$ and is a scalar. The elastic strain increment can be obtained from the stress increment by Hook's law as :

$$d\sigma_{ij} = D_{ij} d\epsilon_{ij}^{e}$$

or

$$d\sigma_{ij} = D_{ij}(d\epsilon_{ij} - d\epsilon_{ij}^{p}) \qquad (5.22)$$

Substituting Eq. 5.21 into 5.22 yields :

$$d\sigma_{ij} = D_{ij}(d\epsilon_{ij} - \frac{\partial f}{\partial \sigma_{ij}} d\lambda) \qquad (5.23)$$

On rearranging the terms in the above equation, after having multiplied both sides by $\frac{\partial f}{\partial \sigma_{ij}}$, it can be shown that (5.15) :

$$d\sigma_{ij} = D_{ij}\epsilon_{ij} - \frac{D_{ij} \frac{\partial F}{\partial \sigma_{ij}} \frac{\partial F}{\partial \sigma_{ij}} D_{ij}}{H' + \frac{\partial F}{\partial \sigma_{ij}} D_{ij} \frac{\partial F}{\partial \gamma_{ij}}} \qquad (5.24)$$

H' is the tangent modulus of stress plastic strain curve. For the hyper-surface, n, H' is given by :

$$H' = \frac{E_n E_1}{E_1 - E_n} \qquad\qquad (5.25)$$

where E_1 is the elastic modulus. Eq. 5.24 can be rewritten in matrix notation as :

$$\{d\sigma\}= [[D] - \frac{[D]\{a\}\{a\}^T[D]}{H' + \{a\}[D]\{a\}}] \ \{d\epsilon\}$$

or

$$\{d\sigma\} = [D_T] \ \{d\epsilon\} \qquad\qquad (5.26)$$

where $[D_T]$ is the current material property matrix.

5.6.5 Material Anisotropy

In the development of the work hardening model of this study two kinds of material anisotropies are considered.

5.6.5.1 Initial Anisotropy

During the first loading cycle certain materials demonstrate different properties in tension and compression. This kind of behavior can be attributed either to residual stresses induced during fabrication of the component or it may be an inherent property of the material. In either case, after the first cycle the stress strain curve shakes down to a closed loop. This kind of initial anisotropy can be considered as that of a material having an inherent history of plastic stresses not accounted for

in the stress values.

The initial anisotropy is characterized by assuming that the initial yield surface had been translated during the manufacturing process (5.13,5.14). Fig. 5.7. In other words the center of rotation of the yield surface is assumed as having an offset, say α_{ij}^O. It is further assumed that there is initial isotropy with respect to tension only or compression only. By this assumption, the offset α_{ij}^O is assumed to have the same values in all directions, say α^O. Implementing this assumption in the yield criteria, Eq. 5.15 can be written as :

$$f(\sigma_{ij} - \alpha^O) - \sigma_Y = 0 \tag{5.27}$$

In the above equation, there are only two unknowns α^O and σ_Y, a solution is therefore obtained by two simultaneous equations, restricting this theory to only plane structures. By requiring that the yield surface must pass through points, $(\sigma_Y^T, 0)$ and $(\sigma_Y^C, 0)$, Fig. 5.7, it can easily be shown that :

$$\alpha^O = \sigma_Y^T - \sigma_Y^C \tag{5.28}$$

and

$$\sigma_Y^2 = \alpha^{O2} + \sigma_Y^T \, \sigma_Y^C \tag{5.29}$$

5.6.5.2 Permanent Anisotropy

Some materials have different material properties in tension and in compression throughout the loading history. Their uniaxial cyclic stress strain curve in the tensile zone is not identical to that in the compressive zone. This materials thereby display permanent material anisotropy. For a constant strain loading the stress strain curve is a closed loop, having different peak values in tension and in compression.

This kind of material behavior can be characterized by changing the shape of the yield surface. All subsequent discussion corresponds to the i th hyper-surface in stress space. This discussion could be extended to multiple hyper-surfaces. The yield function can be divided into different zones with different yield equations as :

$$f(\sigma_{ij} - \alpha_{ij}) - \sigma_Y^T = 0 \qquad \text{for } \bar{\sigma}_m \geq \frac{1}{3} \sigma_Y^T$$

$$f(\sigma_{ij} - \alpha_{ij}) - \sigma_Y^C = 0 \qquad \text{for } \bar{\sigma}_m \leq \frac{1}{3} \sigma_Y^T \qquad (5.30)$$

and $\qquad f(\sigma_{ij} - \alpha_{ij}) - \sigma_Y^{tr} = 0 \qquad \text{for } \frac{1}{3} \sigma_Y^C \leq \bar{\sigma}_m < \frac{1}{3} \sigma_Y^T$

where $\qquad \bar{\sigma}_m = \frac{1}{3}\{ (\sigma_1 - \alpha_1) + (\sigma_2 - \alpha_2) + (\sigma_3 - \alpha_3) \} \qquad (5.31)$

Considering the uniaxial situation, σ_y^{tr} can be defined at a uniaxial tension point and at a uniaxial compression point. ie. :

$$\sigma_y^{tr} = \sigma^C \qquad\qquad \text{for } \bar{\sigma}_m = \frac{1}{3} \sigma_y^C \qquad (5.32$$

and

$$\sigma_y^{tr} = \sigma^T \qquad\qquad \text{for } \sigma_m = \frac{1}{3} \sigma_Y^T$$

Substituting Eq. 5.32 in 5.30 yields :

$$\sigma_Y^{tr} = \frac{3(\sigma_Y^T - \sigma_Y^C)}{(\sigma_Y^T + \sigma_Y^C)} \; \bar{\sigma}_m + \frac{2\sigma_Y^T \sigma_Y^C}{(\sigma_Y^T + \sigma_Y^C)} \tag{5.33}$$

The detailed derivation of this equation is given in appendix C.

In the Haigh-Westergaard stress space, the first two equations of Eq. 5.30 represent cylindrical surfaces with radii $\sqrt{2/3} \; \sigma_Y^T$ and $\sqrt{2/3} \; \sigma_Y^C$, while the third equation represents a frustra of a cone.

For the two dimensional case, the yield surface is schematically shown as Fig. 5.8. It consists of circular arcs in the tension zone, AB, and the compression zone, CD, joined by smooth elliptical transitional curves. Different tangent modulii could exist for the stress fields in compression and in tension, for uniaxial stress strain curve. The material model in the tension zone AB reflects the tangent modulus E^T while in compression zone CD the modulus is E^C.

In the transition zone AD and DC a linear idealization can be developed to represent an approximate smooth transition.

Observing :

$$E = E^T \qquad\qquad \text{for } \bar{\sigma}_m = \frac{1}{3} \sigma_Y^T$$

and

$$E = E^C \qquad\qquad \text{for } \bar{\sigma}_m = \frac{1}{3} \sigma_Y^C$$

$$E^{tr} = \frac{3(E^T - E^C)}{(\sigma_Y^T + \sigma_Y^C)} + \frac{\sigma_Y^T E^C + \sigma_Y^C E^T}{(\sigma_Y^T + \sigma_Y^C)} \tag{5.34}$$

The detailed derivation of Eq. 5.34 is given in appendix C.

5.7 Application of Plasticity to the Finite Element Method

The material model developed, in this study, to represent the behavior of metals including plasticity is implemented in the finite element computer program FINITE (3.9). As the application of the finite element technique to problems with nonlinear material behavior is well established, Dodds (5.12) that process will not be described here in depth, rather only basic concepts are outlined for reference.

In the program FINITE, an incremental iterative technique is used for the solution of nonlinear problems. Loads are applied in specified subincrements, depending upon the nature of the nonlinearity. The incremental nodal displacements are obtained by solving the equation :

$$[K_T]\{\delta u\} = \{\Delta P\} \tag{5.35}$$

where $[K_T]$ is the current tangent stiffness matrix for the structure.

The tangent stiffness matrix can be updated at any time depending on the rate of convergence. The current material property matrix, $[D_T]$, Eq. 5.26, is provided by the material model. This material matrix is used to update the stiffness matrix as derived from the equation :

$$[K_T] = \int_V [B]^T [D_T] [B] \ dv \tag{5.36}$$

The results of this computation are incorporated in Eq. 5.35 for

subsequent determination of displacements.

From the calculated increment in the displacements, increments of the Green's strain are calculated. These calculated strain increments are passed on to the material model routine to calculate corresponding stress increments, Eq. 5.26, and the translation of the hyper-surfaces Eq. 5.18. The flow diagram of the process involved in these computations is shown in Fig. 5.9.

Equivalent nodal loads are calculated for each element by converting element stresses to a system of equivalent loads at the nodes. This system does the same work as the element stresses would do during a virtual displacement. In other words a system of internal nodal forces is calculated for each element. The residual loads are then obtained by subtracting these internal forces from the actual applied forces. The internal forces that are being determined in this process are defined as :

$$\{IF\} = \int_V [B]^T \{\sigma\} \ dv \qquad (5.37)$$

The Newton-Raphson iteration techinque is utilized, in the solution process with the flexibility to update the tangential stiffness matrix during any iteration and as often as specified by the user in an incremetal load step.

Convergence of the solution is checked by comparing the Euclidian norms of the residual loads or that of the current displacement increments, with the applied load increment or initial displacement increment for the current load step

respectively. For every load increment, iterations are performed until the convergence criteria specified by the user is satisfied. At the end of each load step any residual load remaining after calculation is added to the next load step for equlibrium accuracy.

Considered use of this combination of incremental iterative techniques with proper use of the stiffness updating capabilities is observed to yield an efficient computational effort. This method has been suggested and implemented by many researchers (5.3,5.12). It has a proven record of efficiency.

5.8 Conclusion

A versatile material model is developed based on the concepts suggested by Mroz (5.8). The flexibility of this model stems from the fact that stress space is divided in multiple fields of stress modulus. As far as it fits within the general framework of the assumptions, each hyper-surface can be independent of the others in characteristics and properties. Many variations in material behavior could be easily implemented by enforcing specified rules either in the translation or in the shape of the yield surfaces.

The cyclic softening could be reflected by changing the tangent modulus after each half cycle, as demonstrated by Kalev and Gluck (5.14).

Mixed hardening could be implemeted by saying that during plastic flow, the yield surfaces not only translate but they also expand in some proportion (5.3).

Residual stresses could be considered by an initial shift in the hyper-surfaces in a proper direction as discussed in section 5.6.5. Also, the material anisotropy can be handled by defining the hyper-surface as a combination of various surfaces as shown in section 5.6.5.2.

6. NUMERICAL ANALYSIS

6.1 Introduction

In this investigation the behavior of a structure formed by the intersection of several cylinders is studied for various aspects of the geometry of the intersection and also for the placement and amount of reinforcement provided at the intersection. Numerical analyses are carried out both in the elastic and in the plastic ranges of material behavior. The capability of the finite element method for nonlinear cyclic plasticity is demonstrated along with an indication of its applicability to predict the fatigue life for structures of this type.

The first two examples illustrate the capability of the kinematic hardening material model to handle load reversal. The structures are subjected to cyclic loads of high enough magnitude to induce material plasticity. The loads are applied in increments demonstrating the variations in stresses and displacements along with the progression of the yield envelope. A thick walled cylinder under internal pressure is analyzed for a complete load cycle. The results are compared with theoretical values. Also an aluminum plate with two semicircular holes on opposite sides is considered to demonstrate the anisotropic capability of the material model. Reliability of the material model is verified by comparision of the results of these stress

analyses with available analytical or experimental data.

Another two examples are considered to illustrate the reliability of the structural modeling and the numerical analysis for handling the cylinder intersection problem. In the first example one layer of three dimensional elements is considered through the thickness in the region SOLID. The structure is subjected to a small internal pressure inducing a response in the elastic regime. In the second example two layers of three dimensional elements are considered through the thickness in SOLID. The structure is subjected to an incremental internal pressure sequence to evaluate the displacements and stresses in the region of material nonlinearity. A reduced integration technique is used in the examples. Accuracy is verified by comparing the results of the numerical analyses with experimental data.

The behavioral study of the cylinder intersection subjected to internal pressure, is divide into four categories.

1. The effect of the reinforcement around the curve of intersection is studied for a cylinder intersection with aspect ratio of 0.5. Various configurations of the reinforcement are considered to study their effect on stresses. An attempt to find optimum lengths of the reinforcement along the cylinder and in the nozzle is one aspect that recieved additional attention.

2. The stress fields and their variations are studied for normally intersecting cylinders with various aspect ratios. For the parametric study the aspect ratio i

1.0

1.1

1.25   1.4   1.6

2.8   2.5
3.2   2.2
3.6
4.0   2.0

1.8

MICROCOPY RESOLUTION TEST CHART
NATIONAL BUREAU OF STANDARDS-1963-A

86
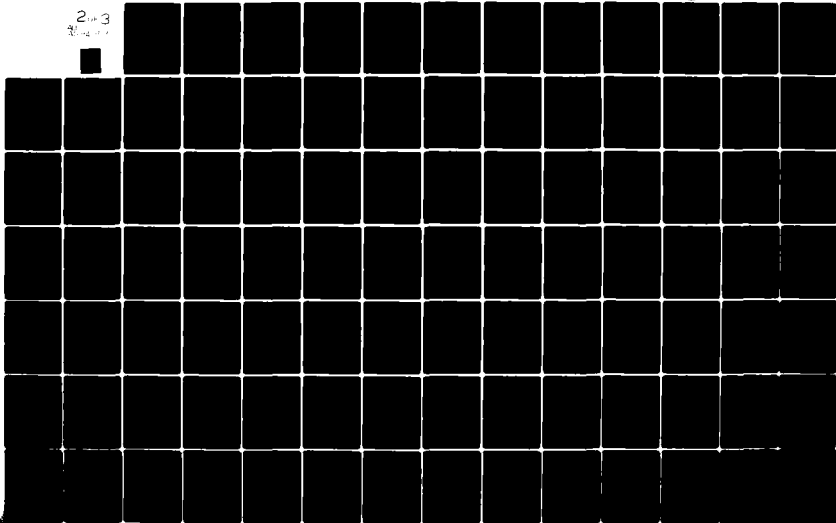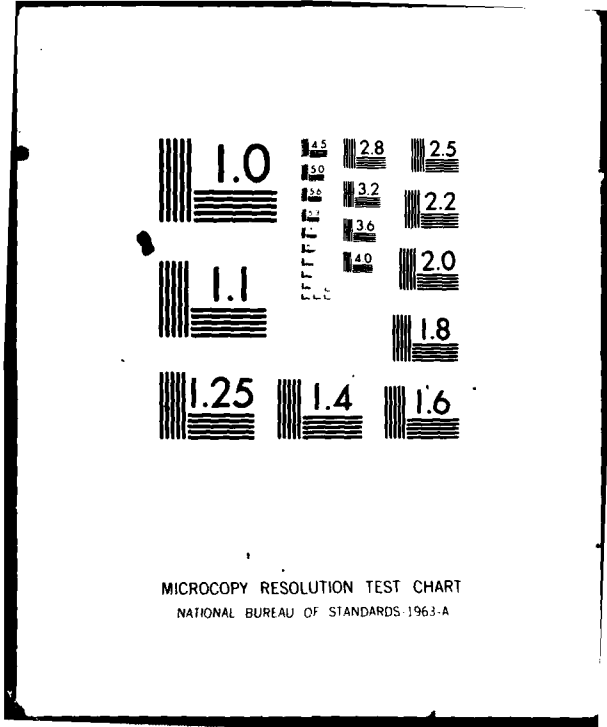
varied from 0.25 to 1.0.

3. The response of the structure with a nonradial nozzle
    is another facet of this work. The effect on the
    stress concentration factor for a decreasing angle of
    intersection is illustrated.

4. An incremental internal pressure sequence is applied to
    the cylinder intersection to study its cyclic response.
    The fatigue life of the structure is then predicted by
    utilizing available numerical techniques for fatigue
    predictions.

6.2 Thick Walled Cylinder

To demonstrate the reliability of the nonlinear cyclic
plasticity model in the finite element program the problem of a
thick walled cylinder is considered. The structure is subjected
to an internal pressure in increments up to a peak value. Then
the pressure is reduced in steps until it reached the same peak
value in suction. The pressure is then again increased in steps
back up to the original peak value to complete the load cycle.
This problem was first investigated by Prager and Hodge (6.1) by
using a finite difference technique for the solution. However,
the cylinder was subjected to only monotonically increasing
pressure.

The structure is constructed of an elastic fully plastic
material. The outer radius of the cylinder is twice the inner
radius. The cylinder is considered infinitely long, making it
possible to consider just a slice of a unit length out of the

structure. This piece of the structure is divided into six quadratic axisymmetric elements organized through the thickness. Only one row of elements along the length is considered. The specified boundary conditions restrain the top and the bottom surfaces of the cylinder from displacements in the axial direction. Fig. 6.1.1.

At the quarter of one cycle the progression of the yield zone, the tangential stress, the radial stress and the displacements are in agreement with those derived by Prager and Hodge. This agreement can be seen in Figs. 6.1.2 through 6.1.6. At peak of the suction, (complete load reversal), the stresses and displacements are exactly same as those at peak pressure but on the opposite side of axis, as expected. On the completion of the loading cycle the displacements and stresses regain their former values, thereby completing a closed loop.

The following remarks are pertinent to the tangential stresses in the thick walled cylinder. It is observed that as the internal pressure increases the elastic tangential stress on the inside surface increases until the initiation of yielding. Once yielding sets in, the peak value of the stress remains along the boundary of the yielded region, releasing the stress inside the yielded zone. The maximum value of the stress monotonically increases along with increases in the internal pressure. Upon load reversal, compressive residual stress sets in at a relatively small pressure relief. At complete unloading, high residual stresses exist. The nature of this stress being compressive on inside surface while tensile at outside surface.

On application of internal suction, yielding initiates at a relatively small value. However it is interesting to note that the absolute maximum value of the stresses, unlike during the loading cycle, remains constant during this increment of load. The value of the stress is the same as that of the maximum value of the same stress at the peak load.

The behavior of the axial stress is also similar to the radial stress with one exception. Before yield the axial stresses are of the same value through the thickness. Also it is interesting to note the consistent behavior of radial stresses through the load cycle. The peak value, being same in magnitude as the internal pressure, is always at the inside surface with a smooth transition to zero stresses at the outside surface. With complete unloading the residual stresses are compressive in nature throughout the thickness. The completly closed loops of displacements and stresses at the end of the load cycle indicates the accuracy of the numerical analysis.

6.3 Notched Plate

The anisotropic capability of the kinematic material model described in this report is demonstrated through the stress analysis of a notched plate. The material used for this structure is an aluminum alloy, 2024-T3. Uniaxial stress strain curves for this material under tensile loading differ considerably from those observed during compressive loading. Experimental investigation of this structure was carried out by Crews (6.2). Since then this plate has become a bench mark for

many investigators (5.3,5.13,5.14) for the demonstration of their cyclic plasticity material models.

The structure consists of a 35 by 11.9 inch rectangular plate with a 0.162 inch thickness. Two symmetrically placed semi circular notches of radius 1.672 inch are provided to induce the stress discontinuity, Fig. 6.2.1. The stress strain curves in tension and compression for the aluminum alloy are expressed with a Ramberg-Osgood approximation as :

$$\varepsilon = \frac{\sigma}{1 \times 10^8} + \frac{3\sigma}{7 \times 10^8} [\frac{\sigma}{0.53 \times 10^5}]^{36} \quad \text{for tension} \quad (6.1)$$

$$\varepsilon = \frac{\sigma}{1 \times 10^8} + \frac{3\sigma}{7 \times 10^8} [\frac{\sigma}{0.47 \times 10^5}]^{7.1} \quad \text{for compression} \quad (6.2)$$

These curves with their linear approximation are shown in Fig. 6.2.2.

A quarter of the plate structure is discretized using two dimensional quadratic isoparametric elements Fig. 6.2.3. Because of its demonstrated improved accuracy and efficiency these elements are evaluated using reduced integration. Boundary conditions appropriate to a symmetry are applied on the lines of symmetry. The structure is subjected to uniformly distributed loads applied along the top edge. The load is applied in small increments for one complete cycle, starting with tensile loads. The stress analysis is carried out for three different load cycles of different magnitudes inducing free field stresses of 25 KSI, 35 KSI and 4.5 KSI. Fig. 6.2.4

For the elastic range, the expected stress concentration factor of 2 is observed. The local stress strain curves are in a reasonable agreement with the experimental data. That deviation that does exist from the exact experimental results can be attributed to the linear idealization of the actual stress strain curves. Close verification of the residual stresses is noted.

6.4 Reinforced Intersection

The behavior of normally intersecting cylinders with the provisions for various configurations of reinforcement is studied by numerical analyses of a base structure and 11 cases of reinforced structures. Two aspects of the reinforcement are investigated. Firstly the reinforcement is provided on the outside of the cylinder. Reinforcement length and thickness are considered as variable parameters while keeping the total area as a constant. In the second category the study focuses on the effect on the stress pattern that results from various distributions of the reinforcement, viz. placed outside the cylinder, placed inside the cylinder, placed outside the nozzle and combinations thereof. The set of intersecting cylinders used in the experiments conducted at Oak Ridge National Laboratory (2.44), is selected as the base structure. This structure has also been investigated numerically by Prince and Rashid (2.42), Bakhrebah and Schnobrich (1.3) and Chen and Schnobrich (1.1). Dimensions of the base structure and material properties are :

Nozzle

    Outside diameter, $d = 2.5$ in.

    Thickness, $t = 0.05$ in.

    Length, $1 = 19.5$ in.

Cylinder

    Outside diameter, $D = 10$ in.

    Thickness, $T = 0.1$ in.

    Half Length, $L = 19.5$ in.

Angle of Intersection, $\alpha = 90$

Dimensionless Parameters

    Nominal hoop stress ratio, $s/S = 1$

    Aspect ratio, $d/D = 0.5$

    ρ $d/D \sqrt{D/T} = 5$

Material Properties

    Modulus of elasticity, $E = 30,000,000$ psi

    Poisson's ratio, $\nu = 0.3$

The reinforcement distribution and the designations used for the structures with the various reinforcement patterns are tabulated in Table 6.1. The structures are subjected to an internal pressure of 50 psi, which induces stresses that remain within elastic region. For the unreinforced base structure the pressure initiating yield is 110 psi(1.1).

In carrying out the computations advantage is taken of symmetry along the longitudinal and the transverse sections. Only quarter of the structure is discretized with the appropriate

boundary conditions specified on planes of symmetry. At the ends of both the nozzle and the cylinder the effect of a rigid end cap is introduced by restricting the tangential rotation and the radial displacements while allowing the axial displacements. Axial force is provided at the ends to simulate the rigid cap action on the rest of the structure. The magnitude of the axial stress applied at the ends of the nozzle and cylinder to account for the internal pressure, p, is then :

$$\sigma = \frac{p * r_{int}^2}{2 * r_{mid} * t_{sh}}$$

where r_{int} and r_{mid} are the internal and the mid surface radii while t_{sh} is the thickness of the shell.

One layer of elements is used through the thickness of the base structure. However, depending upon the thickness of the reinforcement, one or two additional layers of elements are provided to model that reinforcement. The technique of reduced integration is used with a 2 x 2 x 3 pattern of Gaussian integration points. The description of the mesh generation process is presented in Chapter 3. The typical mesh used for the region SOLID is shown in Fig. 6.3.1.

The stress patterns from the analyzed structures are plotted for axial and hoop stresses in the nozzle and in the cylinder at the lines $\phi = 0$ and $\phi = 90$ in Figs. 6.3.2 through 6.3.7. For the reinforced intersecting cylinders three possible locations of stress concentration are observed on the vertical plane forming the axis of symmetry, (ie. a plane containing Z axis, Fig. 2.1).

One of these locations is the inside corner of the intersection of the cylinder and the nozzle walls. The other two locations being near the ends of the reinforcement on the nozzle and on the cylinder. For convenience these locations are designated, hereafter, the "heel", the "noztoe" and the "cyltoe" respectively. Fig. 6.3.1. In absence of the reinforcement, as in case of TRF1, the noztoe and the cyltoe represents the same point at the outside corner of the intersection of the cylinder and the nozzle walls. Several conclusions are derived from a study of these numerical results compiled from the finite element analyses of the various reinforced intersections. These conclusions are based on observations of the computed behavior of these reinforced structures.

1. The solution for the unreinforced structure, TRF1, under an internal pressure of 50 psi shows good agreement with the experimental results. It should be noted that the stresses are computed at integration points. Hence they are not exactly in line with the experimental stress points. To make the comparisions it is necessary to extrapolate the computed stresses to the outer surfaces of the structure. This solution of the unreinforced structure forms the basis for the verification of the analysis and provides the base for the comparisions of the variations in the stress patterns resulting from different reinforcements.

2. At the curve of intersection near $\phi = 0$, even the addition of a small thickness of reinforcement, for

example that provided in TRF2, helps considerably in reducing the magnitudes of the peak stresses. The magnitude of these discontinuity stresses is governed by the differences in stiffness between the connected edges. The unreinforced cylinder edge is quite flexible. The addition of the extra material around the edge of the cylinder starts decreasing this stiffness difference quickly. On the other hand the reinforcement does not have as significant an effect on the hoop stress at ϕ = 90 , Fig. 6.3.7. At this point the stiffness difference is not so large so the beneficial effect is likewise not so large. As the stresses at ϕ = 0 are the dominating stresses with considerably larger values than those occuring at ϕ = 90 , reinforcement of the opening allows an increase in the internal working pressure for the structure, over that would be acceptable for the unreinforced case.

3. Provision of reinforcement reduces the stresses at the heel in comparision to the base structure for all the observed cases; however, in some cases the presence of reinforcement induces a sharp enough local discontinuity at the noztoe and the cyltoe so as to actually result in an increase in the stresses there. These increases, however, do not override the beneficial reduction when comparing with the unreinforced case.

4. For the unreinforced case high tensile hoop stresses develope on the inside fiber of the heel. At this point high axial compressive stresses are also present. This combination of stresses creates a point of highest potential for the initiation of yielding and for the development of a microcrack. The hoop stresses are predominately from membrane contribution, while the high axial stresses are the result of flexure in the longitudinal direction. The structures under consideration exhibit most severity on the inside face of the nozzle as the axial stresses are higher for nozzle than for the cylinder.

5. While changing the size of the reinforcement of type 2 in going through problems TRF2 to TRF8, an interesting effect on all the stresses is observed. This effect is explained here considering the specific case of the hoop stress that occurs in the nozzle at $\phi = 0$. For an unreinforced structure, TRF1, the hoop stresses in the nozzle on the outside fiber are higher than those on the inside fiber at the junction Fig.6.3.2. This is consequence of the negative circumferential moments superimposed on the membrane hoop stresses. These moments are a consequence of the ovalling tendency in the nozzle. The point of contraflexure in the nozzle for this case of hoop moment is at 0.39 inch from the heel. As the reinforcement length is increased from zero, TRF1, the stress at the heel and the noztoe

decrease up to a reinforcement length of 0.4, TRF6. The rate of decrease of stress at the noztoe is faster than that at the heel, thereby transfering the stress control point from the noztoe to the heel. The stress at heel starts increasing in magnitude with further increments in reinforcement length beyond the point of contraflexure, TRF7 and TRF8. The observed minimum value of the stress concentration factor for the hoop stress at heel is 2.04, for TRF6, as compared to 8.69 for the unreinforced structure TRF1. The same phenomenon is observed for axial stresses but with one exception, Fig. 6.3.3. Instead of the heel and the toes being the critical points, stress points are the inside fiber and outside fiber near the toes. The stress concentration factor for axial stress in nozzle is reduced down to 3.25 for optimum reinforcement length of TRF6, as compared with a value of to 12.12 for the unreinforced structure TRF1.

6. The phenomenon of the dilatation of stresses with increments of reinforcement length up to the point of contraflexure and increment in stresses therefrom is also observed for the cylinder. The stress concentration factor for hoop stress is reduced down from its value of 7.14 for the unreinforced case TRF1 to 3.2 for TRF7, Fig. 6.3.4. For axial stress these values are 2.58 for optimum length of TRF7, as compared to 8.06 for the unreinforced structure TRF1,

Fig. 6.3.5.

7. The stresses at the junction near $\phi = 90$ are small in comparision to those near $\phi = 0$. The reinforcement effects on the transeverse plane are considered beneficial but insignificant for most of the cases. However it is interesting to note that the axial stress in the nozzle increases for structures TRF2 and TRF4 compared to the values of stresses for the unreinforced structure TRF1, Fig. 6.3.6. The best configuration of reinforcement for the axial stress in the nozzle at $\phi = 90$ is achieved in structure TRF9. While that for the hoop stress in the cylinder is achieved in the structure TRF12. Fig. 6.3.7.

8. The stress analyses with various combinations of reinforcement of types 1 to 3 is carried out in the second phase of this study of reinforced structures. These combination structures are refered TRF9 through TRF12. To start with the same total area is provided for each type of reinforcement in the three different structures TRF3, TRF9 and TRF10. The reinforcement length of 1.12 inch is provided in these structures with thickness of 0.1 inch. It is observed that for the nozzle, type 2 is more effective for the hoop stress, (TRF3, Fig. 6.3.2), while type 1 gives the best results for the axial stress, (TRF9, Fig. 6.3.3). For the cylinder, reinforcement type 2 is best suited for achieving a reduction in the stresses, (TRF3,

Fig. 6.3.4). In general, out of the three types of reinforcement type 2 is the most desirable one while type 3 is the least desirable one. The combination of reinforcement type 2 and type 3, TRF12, shows little improvement over the structure compared to case with only reinforcement type 2, TRF5. This comparision is made for the cases where the reinforcement used involve the same area. The best combination is achieved by combining reinforcement type 1 and type 2, TRF11. This arrangement consistantly exhibits lowest values for all stress fields. However, as the fabrication of a structure with this reinforcement combination is more difficult than that of the structure with only reinforcement type 2, no further attempt has been made to optimize the lengths for this combination case. Moreover, as in this study, increase in thickness of reinforcement type 2, creates an effect similar to that of the combination of types 1 and 2.

In this parametric study of the reinforcement it is observed that the placement of the reinforcement has significant effect on the stresses. The most effective configuration is achieved by extending the reinforcement up to the points of contraflexure on the nozzle and on the cylinder. In the present problem these points are at 0.39 inch along the nozzle and at 0.49 inch along the cylinder. (Lengths are measured from the heel). ASME standard's specification for the reinforcement length for the same structure along the nozzle and along the cylinder are 0.225

inch and 1.225 inch respectively. These lengths are far off from those observed optimum lengths of the reinforcement.

6.5 Aspect Ratio Study

The approximate analysis of the cylinder intersection problem by utilizing the elastic theory or by a limit analysis approach places a restriction on the possible aspect ratios (d/D) between the cylinders. These analyses are valid for the cases with aspect ratios smaller than 1/3. In the present investigation the effect of higher aspect ratios on the stress pattern of the cylinder intersection is studied. Different structures having aspect ratios ranging from 0.25 to 1.0 are analyzed with an internal pressure limited to induce only an elastic response.

Dimensions of the analyzed structure are selected to keep ratios of nominal hoop stress (s/S) constant. The angle of intersection is ϕ = 90 for all the cases with nozzle length and cylinder half length set at 19.5 inches. Other properties are tabulated in Table 6.2. Mild steel is selected as the material with the following properties :

Modulus of elasticity, E = 30,000,000 psi

Poisson's ratio, ν = 0.3

The structures are analyzed for internal pressure of 50 psi.

Discretization of the structures are carried out exactly as described for the reinforced intersection in the previous

section, excluding the reinforcement, hence the makeup of the grid is not repeated here. Typical mesh for SOLID is shown in Fig. 6.4.1.

Results of the analysis are plotted in Fig. 6.4.2 through 6.4.7 for axial and hoop stresses near $\phi = 0$ and $\phi = 90$ for the nozzle and the cylinder. The following observations are made from the study of these plots.

1. The sharp discontinuity stress field that develops near the curve of intersection at $\phi = 0$ has associated with it a set of stress concentration factors which range from 4.2 to 14.3. The magnitude of these factors depends upon the type of stress involved and upon the aspect ratio being considered, Fig. 6.4.8. The stress field near $\phi = 90$ is not nearly so intense. At that point the stress concentration factor ranges from 0.3 to 7.2. This range is not nearly as large as it seems however because the upper value represents a very abrupt increase to the 7.2 value for the cases when the aspect ratio is near one.

2. The general pattern and shape of the stress plots remain similar throughout the various increase in the aspect ratio. The changes that do take place involve a different magnification on the stresses and an outward movement of the point of contraflexure. This similarity in behavior makes it possible to believe that the closed form solution based on shell theory, which is known applicable to small aspect ratios, can

be extended to structures with higher aspect ratios after some small modifications.

3. As expected of discontinuity stresses in shells, the high stresses induced at the curve of intersection dissipate over a small distance away from the curve of intersection. The stress decay to the membrane solution values within this small zone. The range of this dissipation zone for the nozzle is observed to be 3.4 $\sqrt{r*t}$ while that for the cylinder is 2.85 $\sqrt{R*T}$, both measured from outside corner of the intersection. This indicates the approximation 2.45 $\sqrt{R*T}$ is slightly smaller than actually required.

4. The most vulnerable point for the development of a microcrack and/or for the initiation of yielding is on the inside of the nozzle wall at the point of intersection near $\phi = 0$. This point is subjected to high hoop tensile stress along with a high axial stress of equivalent magnitude but in compression. This results in that point having the highest distortional energy density of any points in the structure. As the aspect ratio is increased the hoop stress at the point decreases, stabilizing to a constant value beyond $d/D = 0.6$. On the other hand the axial stresses at the point decreases for $d/D > 0.5$. Due to these variations the strength of the structure increases along with increase in aspect ratio. The similar point of the inside fiber on the cylinder at the intersection is subjected to

stresses of the same nature, viz. tensile hoop stress and compressive axial stress. This point exhibits a constant increment in stress value with an increment in the aspect ratio above 0.5. Compared to the nozzle point the hoop stresses are lower in value for aspect ratios up to $d/D = 0.83$, beyond which point they increase but only marginally. However the compressive axial stresses are almost half in value compared to the hoop stresses, therefore reducing the severity of this point compared to the companion nozzle point. Hence it can be said that the first yield will always start at the inside fiber of the nozzle at the junction at $\phi = 0$ for all aspect ratios of cylinder intersections under internal pressure.

5. At the aspect ratio of 1.0, the stress concentration factor for axial stress in nozzle at $\phi = 90$, magnifies considerably at the outside fiber. However the stresses are lower than those at $\phi = 0$ and hence it does not introduce any significant new considerations.

Only moderate changes in the stress patterns are observed with the increments in the aspect ratio of the intersecting cylinders subjected to an internal pressure. The governing stress (hoop stress in the nozzle at $\phi = 0$) stabilizes above the aspect ratio of 0.6. The work stress design based on small aspect ratios can safely be extended for the cylinder intersections with large aspect ratios. No dramatic changes

occured in the behavior of the structure for the aspect ratio of 1.0.

6.6 Non-Radial Cylinder Intersection

When two cylinders must intersect having a radial nozzle forming a "T" joint is the most desirable geometry from the view point of the strength of the structure. However, at times for functional reasons nonradial nozzles are installed forming "Y" or "K" joints. This investigation is extended to study the behavior of a cylinder penetrating nonradially into another cylindrical shell with that system under internal pressure. Two catagories of intersections are considered, viz. the "Y" intersection and a "K" intersection. Three structures are analyzed for each catagory, each having a different angle of intersection. For all the cases the aspect ratio is restricted to 0.5 with the same nominal hoop stress ratio s/S. The structure designations and other dimensions are tabulated in Table 6.3. A mild steel material with the same properties as described in the previous section is utilized. The numerical analysis is carried out for an internal pressure of 50 psi. Distance between two nozzles in a "K" joint requires special considerations, as when they are closely placed their responses overlap (6.3). To avoid this overlapping effect a distance of 2(2.45 $\sqrt{R*T}$) is provided between the incoming nozzles.

Unlike the "T" joint, the "Y" joint has only one plane of symmetry that on the longitudinal plane Fig. 2.1. Half of the structure is analyzed with boundary conditions of symmetry set on

the plane X = 0. A "K" joint has two plane of symmetry as one nozzle is the mirror image of the other, making it possible to analyze only one quarter of the total structure. The mesh generator described in Chapter 3, is again utilized for the discretization of these structures. A typical finite element mesh for a "Y" or a "K" joint for the region SOLID is shown in Fig. 6.5.1.

The stress distributions of the structures near the curves of intersection are plotted in Figs.6.5.2 through 6.5.9 for the "Y" and the "K" joints. As the variation of the stresses, if any, between the two categories are marginal, it is decided to represent them together. The stress pattern for the "K" joint is drawn bolder than that of the "Y" joint.

Several important observations are made form the study of the numerically evaluated stress variations.

1. Difference between the stresses that are developed in "Y" joints and in "K" joints are very small. The differences get even smaller with increases in the angle of intersection. Also complete independence from overlapping is not being achieved by the provided distance of $2(2.45 \sqrt{R*T})$ between the nozzles of "K" joint.

2. The tensile hoop stress in the nozzle represents the stress field of highest magnitude, with the localized zone of high stresses at the inside acute corner of the junction at $\phi = 0$, Fig. 6.5.2. The stress concentration factor at this point is as high as 22 for

an angle of intersection of $\alpha = 30$, structure Y3. The stress concentration factor for the hoop stress in the nozzle varies with a change in the angle of intersection. This variation is in close agreement with the relation suggested by the ASME Boiler and Pressure Vessel Code (6.4), which is:

$$K_{nr} = K_r [1 + (\cot\alpha)^{4/3}] \qquad (6.4)$$

where

K_{nr} = stress concentration factor for nonradial nozzle

K_r = stress concentration factor for radial nozzle

α = the angle of intersection

3. At the obtuse corner of the intersection on the *longitudinal axis*, *the hoop stress* in the nozzle is smaller when compared with that for the radial intersection (T2), Fig. 6.5.6. This point shows a moderately incremented increase in stresses with an increase in the angle of intersection. The highest potential point for the initiation of material yielding is on the longitudinal axis at acute corner of the junction.

4. A decrease in the angle of intersection reduces the compressive axial stress in the nozzle and in the cylinder at the acute corner and in the nozzle only at the obtuse corner. The result is a tensile stress when $\alpha = 60$. Figs. 6.5.5 and 6.5.7. However, as the tensile hoop stresses increases at a very rapid rate

this improving effect in axial stress does not translate a significant effect on the rate of increment of the distortional energy density.

6.7 Fatigue Life Prediction

The stress concentrations produced by an abrupt discontinuity, as in the form from an opening in a cylindrical shell, are expecially damaging in cases of fluctuating stresses. Proper allowance for their effect is one of the most important items to be considered while determining the proportions that a design should take in order to resist a fatigue failure. Virtually all failures of such engineering components are a consequences of fatigue (6.5). Recognizing the importance that the possibility of a brittle failure due to fatigue has and the consequences such a failure would have in important structures like nuclear reactors, a small investigation, utilizing the increased computational abilities developed during this study, is applied to predict the fatigue life of intersecting cylindrical shells. For this purpose the structure with an optimum reinforcement arrangement, TRF6, is selected. Geometric parameters of the structure are described in section 6.4, and Table 6.1. For the sake of convenience this structure is redesignated as TNL2 in the subsequent discussion.

The fatigue life investigation is carried out into two stages. In the first stage a nonlinear analysis is performed, utilizing the kinematic hardening material model, to get the patterns of the strains and stresses developed under a given load

history. The second stage consists of taking these results and applying them to the fatigue analysis.

6.7.1 Nonlinear Analysis

Firstly, to verify the reliability of the nonlinear analysis process, a structure with available experimental data is selected for investigation. After the verification, the analysis is carried out for TNL2. Ellyin (2.39) performed an experimental investigation in the region of material nonlinearity. On a steel structure strains were measured at critical locations. The dimensions of the structure and the material properties are :

Nozzle

   Outside diameter,   d = 3.886 in.

   Thickness,   t = 0.124 in.

   Length,   l = 6.706 in.

Cylinder

   Outside diameter,   D = 5.976 in.

   Thickness,   T = 0.187 in.

   Half Length,   L = 7.843 in.

Angle of Intersection, α = 90

Material Properties

   Modulus of Elasticity, E = 30,000,000 psi

   Yield Stress, σ_Y = 25,000 psi

   Hardening Modulus,   H = 200,000 psi

Poisson's Ratio, $\nu = 0.3$

Longitudinal and transverse symmetries are considered during the selection of the structure's discretization. Two layers of 16 noded isoparametric elements evaluated with a reduced integration procedure, are provided in the region SOLID. The developed algorithm for mesh generation is employed for the purpose of input data generation. The mesh for region SOLID is shown in Fig. 6.6.1, along with the progression of the yield enevelope on the inside surface.

6.7.1.1 End Caps

Both the nozzle and the cylinder are provided with caps at their ends in order to close-off the space. Various possibilities exist relative to the behavior that can be prescribed for these caps. An end cap can be very flexible in its lateral bending but rigid with respect to inplane displacements. This situation can be modeled by restraining the radial deformation and circumferential rotation. This type of cap is called hereafter a "Free Cap". The cap can also be completely fixed. A "Fixed Cap" restrains all degrees of freedom. An intermediate case must also exist, in which the cap is very rigid, but the structure is still allowed to deform in the axial direction. This type of cap is designated a "Rigid Cap". The effect these various types of caps have on the structure is studied during the course of this investigation.

Structure TNL1 is subjected to a stepwise incremental internal pressure up to 1000 psi. The deflection of the point on the curve of intersection at $\phi = 0$ is compared with the experimental data in Fig. 6.6.2.

The nonlinear analysis of the structure TNL2 is performed under an internal pressure fluctuation as shown in the Fig. 6.7.4. The structure is subjected to one cycle of loading with a maximum internal pressure of 425 psi. This pressure intensity is four times that required to initiate initial yield of the base structure, (unreinforced structure), under monotonically increasing load. In the present study a mild steel, SAE 1015, is selected for the structure. This selection is based on the fatigue properties and the ductility characteristics of that material. The material properties are described in Figs 4.1 and 4.2. The cyclic stress strain properties of the material are used for the purpose of the analysis. The variation in the hoop stress and in the axial stresses at $\phi = 0$ for the nozzle and for the cylinder are plotted in Fig. 6.7.3. The deflections of the points on the curve of intersection at sweeping angle $\phi = 0$ and $\phi = 90$ are shown in Fig. 6.7.2.

From the results of the analyses the following remarks can be made :

1. The variations of the characteristics of the end cap, as in the case of structure TNL1, has a significant effect on the deformation that structure undergoes. Four cases with different combinations of end cap

conditions were considered in the analysis. The displacements for all the cases agree with each other and the test results in the elastic region; however, in the plastic region the variation is considerable. The stiffest response is observed for the fixed cap while the free cap shows largest deformations and as expected the rigid cap displays the intermediate behavior. The reason of this phenomenon can be attributed to the increase in the length of the region of stress disturbance along with the progression of yielding. The lengths of the nozzle and the cylinder in the case of TNL1, being $2(3.95 \sqrt{r*t})$ and $2(4.07 \sqrt{R*T})$, are more than sufficient to avoid overlapping in the elastic response. However as the yield progresses these free lengths are less than those required to avoid any overlapping.

In real life, most structures have longer lengths of nozzles and cylinders. As the free cap condition is the best representation of this situation, the structure TNL2 is provided with the free caps.

2. In both of the structures initial yielding starts from the inside fibers at the junction $\phi = 0$, then progresses through the thickness at a rather rapid rate. With increments in the internal pressure, the yielded zone expands along the junction as well as along the axial directions of the nozzle and of the cylinder. The progression of the yield envelope on the

inface for structures TNL1 and TNL2 are shown in Figs. 6.6.1 and 6.7.1. On the outface the configuratrion is similar, but with a reduced yielded region.

3. For structure TNL1 the maximum outward displacement of a point on the junction at $\phi = 90$ is 0.01228 inch compared to 0.00081 inch at $\phi = 0$, Fig. 6.6.2. The similar values of displacements for structure TNL2 are 0.00889 inch and 0.00205 inch, Fig. 6.7.2. This shows the structures are suseptible to higher deflections in the transverse direction as compared to those in the longitudinal direction. These uneven displacements distort the nozzle into an oval shape. If enough precautions are not taken, this ovalling can lead to a buckling or collapse tendency of the nozzle. It is interesting to note that the ovalling in the reinforced section is less predominant than that in the case of the unreinforced structure.

The following discussions are with respect to structure TNL2.

4. The initiation of yielding starts at an internal pressure of 243 psi. The similar value for the yield initiation of the base structure is 106 psi. Hence the provision of the reinforcement has increased the efficiency of the structure by a factor of 2.29, when judged on the basis of the working stress criterion. The reinforced structure shows considerable plastic

reserve strength. At the maximum internal pressure of 425 psi, which is four times the value of yield pressure of the base structure, only a small zone of the structure is yielding Fig. 6.7.1, with 0.2% as the maximum strain and 0.00889 inch as the maximum displacement.

6. The maximum observed stress occurs at the peak of applied internal pressure and at $\phi = 0$. This tensile hoop stress of 37.42 ksi exists at the at the inside fiber of the noztoe. It is interesting to note that due to the release in the hoop stress at the junction, a tensile hoop stress of only 29.5 ksi exists at the inside corner. Fig. 6.7.3. At the end of the load cycle, (at zero internal pressure), heavy compressive residual stress remains in the nozzle on the inside fiber at $\phi = 0$. The maximum value of these residual stresses being 16.5 ksi at the corner point. As this point has the maximum amplitude during the stress cycle, it is one of the most potential point for the development of a fatigue crack.

6.7.2 Fatigue Analysis

The process described in Section 4.4, is followed to predict the fatigue life of the cylinder intersection. The first important step in a fatigue life analysis is to find the most vulnerable point in the structure, that is the point with the worst combination of highest equivalent stress stress-strain amplitudes and their mean values. The most potential point, for fatigue crack initiation, is found to be on the curve of the intersection, on the inside fiber of the nozzle at $\phi = 0$. Equivalent stress and strain quatities along with their amplitudes and means are listed in Table 6.4. By substituting the required quantities in Eq. 4.6 , the fatigue life curve is established as :

$$\frac{\Delta\varepsilon}{2} = 0.94933(2N_f)^{-0.64} + 0.003365(2N_f)^{-0.11} \qquad (6.5)$$

From the plot of the fatigue life vs. strain amplitude, the fatigue life of the given structure TNL2 for the pressure cycle of 0 psi to 425 psi is found to be 150000 reversal or 75000 cycles. Fig. 6.7.5.

In most cases, a pressure vessel rarely undergoes more than 10000 cycles in its life time (2.53). Hence, the structure TNL2 can be considered safe from a fatigue failure, for the applied fluctuation of the internal pressure.

7. Concluding Remarks

7.1 Summary

In this study an in depth investigation of the behavior of intersecting cylindrical shells has been carried out. Emphasis in the investigation has been placed on two major aspects. The influence of various geometric parameters on the stress patterns has been studied for the structure under the action of an internal pressure which induces an elastic response. In the second phase, the efforts concentrated on the nonlinear material response. Here the objective was the development of basic data that can be used in an exposition of the fatigue characteristics of the structure.

A versatile general purpose algorithm has been presented for the discretization of intersecting cylinders. The capabilities of this mesh generator have been demonstrated by the effective discretization of a variety of structures which encompass various aspect ratios, angles of intersection and reinforcement configurations.

Efficient use of the finite element analysis technique is sought by organizing the substructuring approach with a proper selection of the elements used in the different substructures. The chosen isoparametric elements are rendered economical by utilizing the technique of reduced integration.

A material model with the concepts of kinematic hardening is implemented in order to study the structural response including cyclic plasticity. For this purpose, Mroz's idealization using field's of work hardening is incorporated. A nonlinear finite element analysis is performed on the intersecting cylinders while they are subjected to cyclic loads. The fatigue life of the structure is predicted from the stress-strain amplitudes computed at the most critical point.

7.2 Conclusions

High stress concentration develops at the junction of the intersecting cylindrical shells. Even a small amount of reinforcement around the curve of intersection introduces a considerable reduction in these high stress fields. The optimum configuaration of the reinforcement consists of reinforcing up to the points of contraflexure on the nozzle and on the cylinder. This observation of the optimum reinforcement is not checked for other base structures but for just the one under investigation. However the similarity of the stress patterns of unreinforced intersections with different aspect ratios, makes plausible the supposition that this observation can be extrapolated to apply for the general case with pressure loading.

The investigation of the variation of aspect ratios, ranging from 0.25 to 1.0, indicates that this variation has very moderate effect on the stress patterns produced in the cylinder intersections. The dominating stress concentration factor (that for the hoop stress on the inside fiber of the nozzle at $\phi = 0$)

increases slightly with increases in the aspect ratio, before levelling off at a constant value above the aspect ratio of 0.6.

Very high stress concentration factors are observed for the non-radial cylinder intersection. The location of these high values being at the acute angle of the inside corner on the junction. The variation in the stress concentration factor, while considering an elastic response, is observed to be following the relationship presented by ASME standards. However it should be noted that under normal conditions, it is very unlikely to expect an unyielded material at a location of such an intense stress concentration. On the other hand it is acknowledged that no attempt has been made in this analysis to reduce the sharpness of the acute corner at the junction.

Overlapping of the stresses in a "K" joint can be avoided by a carefully designed intermediate length between the two nozzles. In the present case the intermediate length of $2(2.45 \sqrt{R*T}$) showed only minimal overlapping. The stress influence is observed to be increasing with a decrease in the angle of intersection.

The reinforced intersection displays a considerable plastic reserve strength. The capacity of the structure is increased markedly by providing reinforcement. Also by allowing the structure to sustain modest yielding in the region of high stresses additional use can be made of the increased capacity.

The fatigue life prediction of the analyzed structure has indicated the safety of the structure from a fatigue failure. One of the most important factors contributing this safety is

having the linear response of the structure after the the first load cycle. Other contributing factors are the inclusion of an effective reinforcement, ductility of the material, and carefully restrained plasticity.

7.3 Recommendations for Further Studies

The recommendations for future study include the following :

1. The usefulness of the finite element method for the parametric study of the cylinder intersection has been established in this investigation. The parametric study should be extended to include additional parameters not included in the present study, like d/t, D/T, t/T etc.

2. The variations in the stress patterns of normally intersecting cylinders, with the increment of the aspect ratio, are moderate in nature. As a closed form solution based on an elastic thin shell theory already exists for aspect ratios < 1/3, the effort should be directed to extend this solution for higher aspect ratios, with necessary modifications.

3. Fatigue analysis should be extended to an experimental evaluation of the intersecting cylinders, for the purpose of the verification of the procedure presented in this study.

LIST OF REFERENCES

1.1   Chen, H. C. and Schnobrich, W. C., "Nonlinear Analysis of Intersecting Cylinders by the Finite Element Method," S.R.S. No. 435, University of Illinois at Urbana-Champaign, 1976.

1.2   Brown, S. J., Haizlip, L. D., Nielsen, J. M., and Reed, S. E., "Analytical and Experimental Stress Analysis of Cylinder-to-Cylinder Structure," Journal of Pressure Vessel Technology, Vol. 99, pp. 575-583, 1977.

1.3   Bakhrebah, S. A., and Schnobrich, W. C., "Finite Element Analysis of Intersecting Cylinders," S.R.S. No. 400, University of Illinois at Urbana-Champaign, 1973.

2.1   Kirsch, G., "Die Theorie der Elastizitat und die Bedurfnisse der Festigkeitslehre," Z.V.D.I., Vol. 42, pp. 797, 1898.

2.2   Lure, A. I., "Statics of Thin-walled Elastic Shell," State publishing House of Technical and Theoretical Literature, Moscow, Ch. 4, Art. 9, 1947.

2.3   Lure, A. I., "Concentration of Stresses in the Vicinity of an Aperture in the Surface of a Circular Cylinder," Prik, Math Mat. i. Mekh. 10, pp. 397-406, 1946. (English translation by N. Brunswick, New York University, Inst. of Math. Sc. 1960.)

2.4   Pirogov, I. M., "Stress Concentrations in the Region of a Rigid Ring on the Surface of a Circular Cylinder," (in Russian), Sb. Statei vsesoiuzn, Zaochn Politekhn, In-ta 16, pp. 65-71, 1957.

2.5   Savin, G. N., "Stress Distribution Around Holes," Kiev, 1968 (in Russian).

2.6   Gouz, G. N., "Concentration of Stress Around Openings in the Thin Shells," Prikladnaja Mekhanika, Vol. V-3, pp. 1-17, 1969.

2.7   Van Dyke, P., "Stress About a Circular Hole in Cylindrical Shell," AIAA, Vol. 9, pp. 1733-1742, 1965.

2.8   Lekkerkerker, J. G., "Stress Concentration Around Circular Holes in Cylindrical Shells," Proc. of 11 th International Conference of Applied Mechanics, Munich, pp. 283-288, 1964.

2.9   Reidelbach, W., "Der Spannungszustand im Ubergangsgebiet einer rechtwinkligen Rohrabzweigung," Ingenieur Archiv, XXX, pp. 293-316, 1961.

2.10   Lekkerkerker, J. G., "Elastic Stresses Near Cylinder-to-Cylinder Intersections," Nuclear Engineering and Design, Vol. 20, pp. 57-84, 1972.

2.11   Tyn, Mint, Radak, J. R. M., and Wolfson, "Numerical Solution of Shell Intersection Problem," Osterreichisches Ingenieur Archiv XVI, Heft 3, pp. 253-270, 1963.

2.12   Eringer, A. C., Suhubi, E. S., "Stress Distribution of Two Normally Intersecting Cylindrical Shells," Nuclear

Structural Engineering, Vol. 2, No. 2, 1965.

2.13   Eringer, A. C., Naghdi, A. K., Mahmood, S. S., Thiel, C. C., and Ariman, T., "Stress Concentrations in Two Normally Intersecting Cylindrical Shells Subjected to Internal Pressure," Welding Research Council, Bulletin No. 139, 1969.

2.14   Yamamoto, Y. H., Isshiki, H., Hamada, K., Hayashi, T., and Ukaji, H., "Theory of Stress Concentration of Two Normally Intersecting Cylindrical Shells," Bulletin of the Japanese Society of Mechanical Engineers, Vol. 12, No. 49, 1969.

2.15   Bylaard,P. P., Dohrmann, R. J., and Wang, I. C., "Stress in Junction of Nozzle to Cylindrical Pressure Vessel for Equal Diameter of Vessel and Nozzle," Nuclear Engineering and Design, Vol. 5, pp. 349-365, 1967.

2.16   van Campen,D. H., "Mechanical and Thermal Stresses in Cylinder-to-Cylinder Intersection, of Equal or Nearly Equal Diameter," Proc. First International Conference on Pressure Vessel Technology, pp. 193-307, 1969.

2.17   Pan, K. C., and Beckett, R. E., "Stress and Displacement Analysis of a Shell Intersection," Journal of Engineering for Industries, pp. 303-308, 1970.

2.18   Robinson, M., "Lower Bound Limit Pressure of a Flush Radial Cylindrical Branch in a Cylindrical Pressure Vessel," Transactions of Third International Conference on Structural Mechanics in Reactor Vessel Technology,

paper No. G1/6, 1975.

2.19   Robinson, M., "Lower Bound Limit Pressure for the Cylinder to Cylinder Intersection, A Parametric Survey," Transactions of ASME, Journal of Pressure Vessel Technology, pp. 65-73, Vol. 100, 1978.

2.20   Ellyin, F., and Turkkan, N., "Lower Bound to Limit Pressure of Nozzle-to-Cylinder Shell Attachment," ASME paper no. 71, pvp-38, 1971.

2.21   Biron, A., and Courchese, A., "On Limit Analysis of Cylinder-to-Cylinder Intersections Subjected to Internal Pressure," Nuclear Engineering and Design, Vol. 36, pp. 68-80, 1976.

2.22   Goodall, I. W., "On the Design of Intersection in Pressure Vessels," Ph.D. thesis, University of Cambridge, 1967.

2.23   Cloud, R. L. and Rodabaugh, E. C., "Approximate Analysis of the Plastic Limite Pressure of Nozzle in Cylindrical Shells," Journal of Engineering for Power, Vol 90, No. 2, pp. 171-176, 1968.

2.24   Schroeder, J. and Rangarajan, P., "Upper Bounds to Limit Pressure of Branch Pipe Tee Connections," First International Conference on Pressure Vessel Technology, pp. 277-292, 1969.

2.25   Schroeder, J. and Roy, B. K., "Upper Bounds to Limit Pressure of Branch-Pipe Lateral Connections," ASME paper No. 71-PVP-43, 1971.

2.26   Hardenbergh, D. E., "Stresses in Contoured Openings of Pressure Vessels," Welding Research Bulletin No. 51, 1959.

2.27   Taylor, C. E., Lind, N. C., and Schweiker, W. E., "A Three Dimensional Photoelastic Study of Stresses Around Reinforced Outlets in Pressure Vessels," Welding Research Bulletin No. 51, 1959.

2.28   Mershon, J. L., "Preliminary Evaluation of PVRC Photo-elastic Test Data on Reinforced Opening in Pressure Vessels," Welding Research Council Bulletin No. 113, 1966.

2.29   Hardebergh, D. E., Zamrik, S. Y., and Edmondson, A. J., "Experimental Investigation of Stresses in Nozzles in Cylindrical Pressure Vessels," Welding Research Bulletin No. 89, 1963.

2.30   Hardenbergh, D. E., and Zamrik, S. Y., "Effects of External Loadings on Large Outlets in a Cylindrical Pressure Vessel," Welding Research Council Bulletin No. 96, 1964.

2.31   Riely, W. F., "Experimental Determination of Stress Distributions in Thin-Walled Cylindrical and Spherical Pressure Vessel with Circular Nozzles," Welding Research Council Bulletin No. 108, 1965.

2.32   Mehringer, F. J., and Cooper, W. E., "Experimental Determination of Stresses in the Vicinity of Pipe Appendages to a Cylindrical Shell," Society of Experimental Stress Analysis, Vol. XIV, No. 2.

2.33 Cranch, E. T., "An Experimental Investigation of Stresses in the Neighborhood of Attachment to a Cylindrical Shell," Welding Research Council Bulletin No. 60, 1960.

2.34 Taniguchi, K., Kono, K., Iki, T., and Setoguchi, K., "A Study of Local Stresses Around Nozzles of Pressure Vessels Under External Loadings," First International Conference on Pressure Vessel Technology, pp. 117-119, 1969.

2.35 Corum, J. M., Bolt, S. E., Greenstreet, W. L., and Gwaltney, R. C., "Experimental and Finite Element Stress Analysis of a Thin Shell Cylinder-to-Cylinder Model," ASME publication, paper No. 71-PVP-36.

2.36 Lind, N. C., Sherbourne, A. N., Ellyin, F., and Dainora,J., "Plastic Tests of Two Branch Pipes," Welding Research Council Bulletin No. 164, 1971.

2.37 Schroeder, J., Shrinivasaiah, K. R., and Graham, P., "Analysis of Test Data on Branch Connections Exposed to Internal Pressure and/or External Loads," Welding Research Council Bulletin No. 200, 1974.

2.38 Ellyin, F., "Experimental Investigation of Limit Loads of Nozzles in Cylindrical Vessel," Welding Research Council Bulletin No. 219, 1976.

2.39 Ellyin, F., "An Experimental Study of Elastic-Plastic Response of Branch-Pipe Tee Connection Subjected to Internal Pressure, External Couples and Combined Loadings," Welding Research Council Bulletin No. 230,

1977.

2.40   Maxwell, R. C., and Holland, R. W., "Collapse Test of a Thin Walled Cylindrical Pressure Vessel with Radially Attached Nozzle," Welding Research Council Bulletin No. 230, 1977.

2.41   Schroeder, J., and Tugcu, P., "Plastic Stability of Pipes and Tees Exposed to External Couples," Welding Research Council Bulletin No. 238 1978.

2.42   Prince, N., and Rashid, Y. R., "Structural Analysis of Shell Intersections," First International Conference on Pressure Vessel Technology, pp. 245-254, 1969.

2.43   Greste, O., "Finite Element Analysis of Tubular K-Joints," Report No. NCSESM 70-11, University of California, Berkeley, 1970.

2.44   Corum, J. M., Bolt, S. E., Greenstreet, W. L., and Gwaltney, R. C., "Theoretical and Experimental Stress Analysis of ORNL Thin-shell Cylinder-to-Cylinder Model No. 1," USAEC Report ORNL-4553, Oak Ridge National Laboratory.

2.45   Hellen, I. K., and Money, H. A., "The Application of Three Dimensional Finite Elements to a Cylinder-to-Cylinder Intersections," International Journal for Numerical Methods in Engineering, Vol. 2, 1970.

2.46   Bathe, K. J., Bolourchi, S., Ramaswamy, S., and Snyder, M. D., "Some Computational Capabilities for Nonlinear Finite Element Analysis," Nuclear Engineering and

Design, Vol. 46, 1978.

2.47   Ando, Y., Yagawa, G., Kikuchi, F., "Stress Distributions in Thin Walled Intersecting Cylindrical Shells Subjected to Internal Pressure and In-Plane Forces," First International Conference on Structural Mechanics in Reactor Technology, Berlin, pp. 20-24, 1971.

2.48   Argyris, J. H., Faust, G., Szimmat, J., Warnke, E. P., and William, K. J., "Recent Developments in the Finite Element Analysis of Prestressed Concrete Reactor Vessel," Nuclear Engineering and Design, Vol. 28, 1974.

2.49   Gwaltney, R. C., Corum, J. M., Bolt, S. E., and Bryson, J. W., "Experimental Stress Analysis of Cylinder-to-Cylinder Shell Models and Comparison with Theoretical Predictions," Journal of Pressure Vessel Technology, Vol. 98, pp. 283-290, 1976.

2.50   Gantayat, A. N., and Powell, G. H., "Finite Element Analysis of Thin and Thick-Walled Tubular Joints," Nuclear Engineering and Design, Vol. 46, 1978.

2.51   Kroenke, W. C., McKinley, D. A., "Experience in Comparing Elastic-Plastic Solutions with Nozzle Test Results," ASME 80-C2/PVP-10 Century 2 Pressure Vessel and Piping Conference, San Francisco, CA., August 1980.

2.52   Welding Research Council Bulletin No. 113, April 1963.

2.53   Chukwujekwu, S. E., "Reinforcement Method for Flush Nozzles in Pressure Vessels," First International Conference on Pressure Vessel Technology, Part 1,

pp. 165-174, 1969.

2.54   Cloud, R. L., and Radabaugh, E. C., "Proposed Reinforcement Design Procedure for Radial Nozzles in a Spherical Shell with Internal Pressure," WRC Bulletin No. 113, April 1963.

2.55   Atterbury, T. J., and Bert, C. W., "A New Approach for Design of Reinforcement of Thin Shells," Second Int. Conf. on Pressure Vessel Technology, Part 1, pp. 47-60, 1973.

2.56   Radabaugh, E. C., "Review of Service Experience and Test Data on Openings in Pressure Vessels with Non-integral Reinforcing," WRC Bulletin No. 166, October 1971.

2.57   ASME Boiler and Pressure Vessel Code, Section I, Power Boilers, and Section VIII, Unfired Pressure Vessels. Code for Pressure Piping, ASA B31.1, American Standard Association. API Recommendation Rules for Design and Construction of Large Welded Low Pressure Storage Tanks. API Standards 620, American Petroleum Institute.

2.58   B.5.1500 Fusion Welded Pressure Vessels, British Standard Institution, London, 1958.

2.59   B.S.3915 Steel Pressure Vessels for Primary Circuits of Nuclear Reactors, British Standard Institution, London 1965.

2.60   Markblatt, A. D., B9, Openings in Cylinders, Cones and Spheres Under Internal Pressure, DK 621-02-001-24,

Design of Pressure Vessels, January 1960.

3.1   Zienckiewicz, O. C., "The Finite Element Method," McGraw-Hill Book Company, 1977.

3.2   Cook, R. D., "Concepts and Applications of Finite Element Analysis," John Wiley & Sons, Inc., 1974.

3.3   Desai, C. S., Abel, J. F., "Introduction to the Finite Element Method," Litton Educational Publishing Inc., 1972.

3.4   Lopez, L. A., "FINITE: An Approach to Structural Mechanics Systems," Int. Journal for Numerical Methods in Engineering, Vol. II, pp. 851-866, 1977.

3.5   Lopez, L. A., Dodds, R. H.,Jr., Rehak,D. R., and Urzua, J., "POLO-FINITE. A Structural Mechanics System for Linear and Nonlinear Analysis," Civil Engineering Systems Laboratory, University of Illinois at Urbana-Champaign.

3.6   Vlasov, V. Z., "Thin Walled Elastic Beams," 2 nd Edition, The National Science Foundation, Washington D. C.

3.7   Taylor, C. E., and Lind, N. C., "Photoelastic Study of the Stresses Near Openings in a Pressure Vessel," Bulletin No. 113, Welding Research Council, April 1966.

3.8   Ahmad, S., Irons, B. M., and Zienkiewicz, O. C., "Analysis of Thick and Thin Shell Structures by Curved Finite Element," Int. Journal for Numerical Methods in Engineering, Vol. 2, pp. 419-451, 1970.

128

4.1   Gohn, G. R., "The Mechanism of Fatigue," Materials Research and Standards, Vol. 3, No. 2, pp. 106-115, February 1963.

4.2   Morrow, Jo Dean, "Cyclic Plasticity Strain Energy and Fatigue of Metals," ASTM STP No. 378, 1965.

4.3   Tuler, F. R., "Cyclic Stress-Strain Behavior of OFHC Copper," MS Thesis, Dept. of Theoretical and Applied Mechanics, University of Illinois at Urbana-Champagin, TAM Report No. 239, March 1963.

4.4   Benham, P. P., and Ford, H., "Low Endurance Fatigue of Mild Steel and Aluminum Alloy," Journal of Mechanical Engineering Science, Vol. 3, No. 2, pp. 119, 1961.

4.5   Landgraf, R. W., "High Fatigue Resistance in Metals and Alloys," ASTM STP No. 467, pp. 3-36, 1970.

4.6   Landgraf, R. W., Morrow, J. D., and Endo, T., "Determination of the Cyclic Stress-Strain Curve," Journal of Materials, Vol. 4, No. 1, pp. 178-188, March 1969.

4.7   Radziminski, J. B., Shrinivasan, R., Moore, D., Thraser, C., Munse, W. H., "Fatigue Data Bank and Data Analysis Investigation," SRS No. 405, University of Illinois at Urbana-Champaign, June 1963.

4.8   Brown, M. W. and Miller, K. J., "A Theory for Fatigue Failure under Multi-axial Stress-Strain Conditions," Proceedings, Institute of Mechanical Engineers, London, Vol. 187, pp. 745-755, 65/73.

4.9   Krempl, E., "The Influence of State of Stress on Low-cycle Fatigue of Structural Materials: A Literature Survey and Interpretive Report," ASTM, STP 549, 1974.

4.10   Halford, G. R., "The Energy Required for Fatigue," Journal of Materials, Vol. 1, No. 1, pp. 3-18, March 1966.

4.11   Garud, Y. S., "A New Approach to the Evaluation of Fatigue Under Multi-axial Loadings," ASTM and SAE Workshop on Elasto-plastic Material Behavior and Component Fatigue Analysis, pp. 247-263, April 1980.

4.12   Manson, S. S., "Thermal Stress and Low Cycle Fatigue," McGraw-Hill Book Company, 1966.

4.13   Section III, Div. 1, Nuclear Power Plant Components, Subsection NA, Appendix XIV, ASME Boiler and Pressure Vessel Code, The American Society of Mechanical Engineers, New York, 1974.

4.14   Mason, W. P., "Internal Friction, Plastic Strain and Fatigue in Metals and Semi-Conductors," Basic Mechanism of Fatigue, ASTM STP No. 237, pp. 36-50, 1958.

4.15   Coffin, L. F. Jr., "Experimental Support for Generalized Equation Predicting Low Cycle Fatigue," Transactions, American Society of Mechanical Engineers, Vol. 84 Series D., Journal of Basic Engineering, December 1962, pp. 533-554.

4.16   Basquin, O. H., "The Exponential Law of Endurance Tests," Proceedings, ASTM, Vol. 10, Part II, pp.

625-630, 1910.

4.17   Morrow, J. D., "Modern View of Material Testing," Mechanical Behavior of Materials, Vol. 5, The Society of Materials Science, pp. 362-379, 1972.

4.18   Ohji, Miller, W. R. and Marin, J., "Cumulative Damage and Effect of Mean Strain in Low Cycle Fatigue of a 2024-T351 Aluminum Alloy," Journal of Basic Engineering (series D of ASME Transactions), Vol. 88, pp. 801-810, December 1966.

4.19   Sandor, B. I., "Fundamentals of Cyclic Stress and Strain," The University of Wisconsin Press, 1972.

4.20   Richards, F. D., LePointe, N. R., and Wetzel, R. M., "A Cycle Counting Algorithm for Fatigue Damage Analysis," Society of Automative Engineers, SAE No. 740278, New York, 1974.

4.21   Socie, D. F., "Fatigue Life Estimation Techniques," Technical Report No. 145, Dept. of Mechanical and Industrial Engineering, University of Illinois at Urbana-Champaign, August 1980.

4.22   Miner, M.N., "Cumulative Damage in Fatigue," Transactions, American Society of Mechanical Engineers, Vol. 67, pp. A 159, 1945.

5.1   Mendelson, A., "Plasticity: Theory and Application," The MacMillan Company, New York.

5.2   Prager, W., "The Theory of Plasticity--A survey of Recent Achievements," Proceedings, Institute of Mechanical Engineers, London, No. 169, 41, 1955.

131

5.3 Axelsson, K., and Samuelsson, A., "Finite Element Analysis of Elastic-Plastic Materials Displaying Mixed Hardening," Int. Journal for Numerical Methods in Engineering, Vol. 14, pp. 211-225, 1979.

5.4 Westergaard, H. M., "On the Resistance of Ductile Materials to Combined Stresses," J. Franklin Institute, pp. 627-640, 1920.

5.5 Hill, R., "Mathematical Theory of Plasticity," Oxford, 1950.

5.6 Perrone, N. and Hodge, P. G., Jr., "Applications of a Consistent Theory for Strain Hardening of Plastic Solids," PIBAL Report No. 403, Polytechnique Institute of Brooklyn, New York, September 1957.

5.7 Ziegler, H., "A Modification of Prager's Hardening Rule," Quarterly of Applied Mathematics, Vol. 17, 1959-60.

5.8 Mroz, Z., "An Attempt to Describe the Behavior of Metals Under Cyclic Loads Using a More General Work Hardening Model," Acta Mechanica, Vol. 7-8, pp. 99-112, 1969.

5.9 Drucker, D. C., "Some Implications of Work Hardening and Ideal Plasticity," Quarterly of Applied Mathematics, Vol. 7, No. 4, 1950.

5.10 Prandtl, L., "Spannungsverteilung in Plastichen Koerpen," Proceedings of First Int. Congress on Applied Mechanics, Delf Technische Boekhandel en Druckerij, J. Wattman Jr., pp. 43-44, 1925.

5.11   Reuss, E., "Beruecksichtigung der Elastichen and Formaenderungen in der Plastizitaetastheorie," Z. Agnew, Math. Mech. 10, pp. 266-274, 1930.

5.12   Dodds, R. H., Jr., "Numerical and Software Requirements for General Nonlinear Finite Element Analysis," SRS No. 454, University of Illinois at Urbana-Champaign, 1978.

5.13   Isakson, A., Armen, H., Jr. and Pifko, A., "Discrete-Element Methods for the Plastic Analysis of Structures," NASA CR-803, Washington D.C., October 1967.

5.14   Kalev, I., and Gluck, J., "Finite Element Analysis," Journal of the Engineering Mechanics Division, pp. 189-201, February 1977.

5.15   Nayak, G. C., "Plasticity and Large Deformation Problems by the Finite Element Method," unpublished Ph.D. Thesis, University of Wales, Swansea, 1971. (C/H/15/1971).

6.1   Prager, W., and Hodge, P. G., Jr., "Theory of Perfectly Plastic Solids," John Wiely & Sons Inc. 1951.

6.2   Crews, J. H., Jr., "Elastoplastic Stress-Strain Behavior at Notch Roots in Sheet Specimens under Constant Amplitude Loading," NASA TN D-5253, National Aeronautical and Space Administration, Washington D. C., June 1969.

6.3   Mahoney, J. B., and Salerno, V. L., "Analysis of a Circular Cylindrical Shell Perforated by a Large Number

of Radial Holes," ASME Publication Paper 66-WA/PVP-1, 1966.

6.4   ASME Boiler and Pressure Vessel Code, Section III.

6.5   Harvey, J. F., "Theory and Design of Modern Pressure Vessels," 2 nd Edition, Von Nostrand Reinhold, 1974.

TABLE 6.1

REINFORCED INTERSECTIONS

Designation	Reinf. Type 1		Reinf. Type 2		Reinf. Type 3	
	Length (in)	Thickness (in)	Length (in)	Thickness (in)	Length (in)	Thickness (in)
TRF1	--	--	--	--	--	--
TRF2	--	--	2.24	0.05	--	--
TRF3	--	--	1.12	0.1	--	--
TRF4	--	--	2.24	0.1	--	--
TRF5	--	--	1.06	0.2	--	--
TRF6	--	--	0.7	0.3	--	--
TRF7	--	--	0.53	0.4	--	--
TRF8	--	--	0.4	0.5	--	--
TRF9	1.125	0.1	--	--	--	--
TRF10	--	--	--	--	1.125	0.1
TRF11	0.742	0.1	1.0	0.1	--	--
TRF12	--	--	1.22	0.1	1.22	0.1

TABLE 6.2

ASPECT RATIO STUDY

Cylinder Diameter, D = 10 in.

Cylinder Thickness, T = 0.1 in.

Cylinder Half Length, L = 19.5 in.

Nozzle Length, ℓ = 19.5 in.

Designation	Nozzle Diameter (in)	Nozzle Thickness (in)	Aspect Ratio (d/D)
T1	2.5	0.025	0.25
T2	5.0	0.05	0.5
T3	6.0	0.06	0.6
T4	7.0	0.07	0.7
T5	8.0	0.08	0.8
T6	9.0	0.09	0.9
T7	10.0	0.1	1.0

TABLE 6.3

NON-RADIAL NOZZLES

Nozzle Diameter, d = 5 in.

Nozzle Thickness, t = 0.05 in.

Nozzle Length, ℓ = 19.5 in.

Cylinder Diameter, D = 10 in.

Cylinder Thickness, T = 0.1 in.

Cylinder Half Length, L = 19.5 in.

Designation	Angle of Intersection
T2	90°
Y1	60°
Y2	45°
Y3	30°
K1	60°
K2	45°
K3	30°

TABLE 6.4

EQUIVALENT STRESS-STRAIN HISTORY FOR STRUCTURE TNL2
ON INSIDE CORNER OF THE NOZZLE AT $\phi = 0^{O}$

At Internal Pressure of 425 psi:

    Equivalent Stress $\bar{\sigma}_e max = 29,279$ psi (tensile)

    Equivalent Strain $\bar{\epsilon}_e max = 1.8025 \times 10^{-3}$ (tensile)

At Internal Pressure of 0 psi:

    Equivalent Stress $\bar{\sigma}_e min = 16,958$ psi (compressive)

    Equivalent Strain $\bar{\epsilon}_e min = 0.4675 \times 10^{-3}$ (compressive)

Mean Equivalent Stress $\bar{\sigma}_e mean = 6,160.5$ psi (tensile)

Equivalent stress amplitude $\Delta\bar{\sigma}_{e/2} = 23,118.5$ psi

Mean equivalent strain $\bar{\epsilon}_e mean = 0.6675 \times 10^{-3}$ (tensile)

Equivalent strain amplitude $\Delta\epsilon_{e/2} = 1.135 \times 10^{-3}$
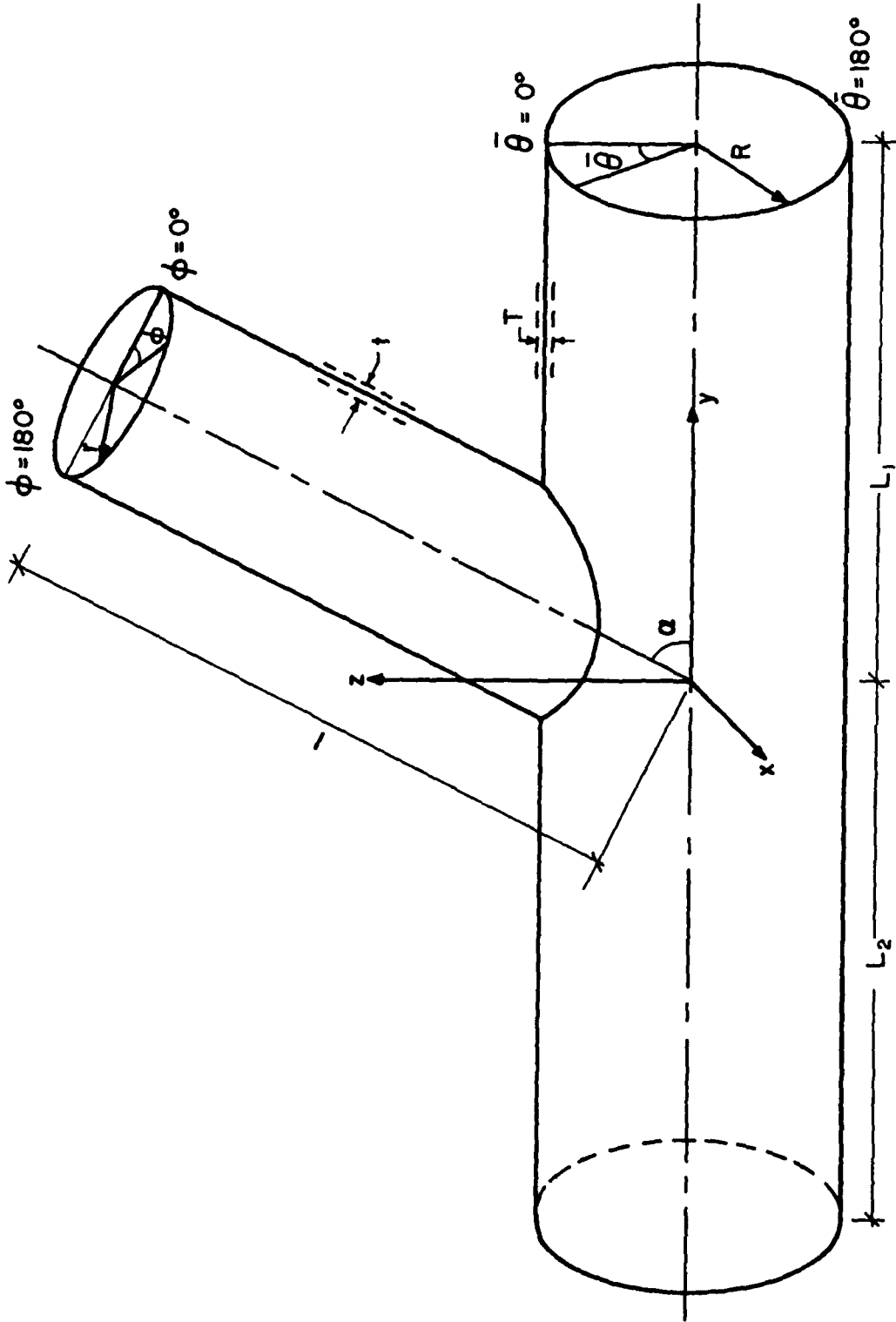
Fig. 2.1 Geometry and Dimensions of Intersecting Cylinders

Nozzle
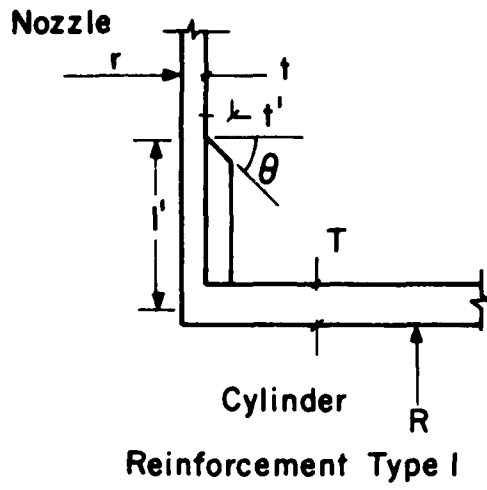
Reinforcement Type I

Nozzle

Reinforcement Type 2

Nozzle
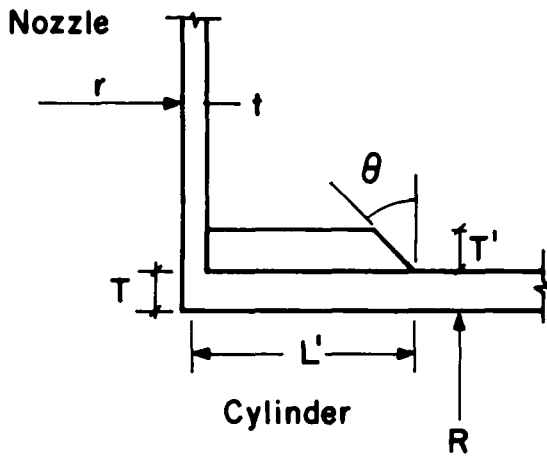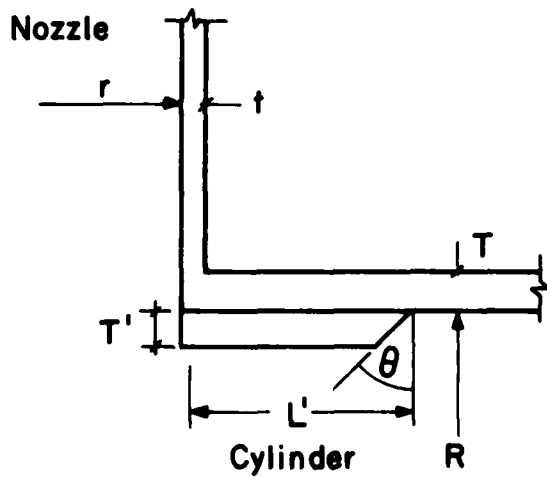
Reinforcement Type 3

Fig. 2.2 Basic Reinforcement Configuration
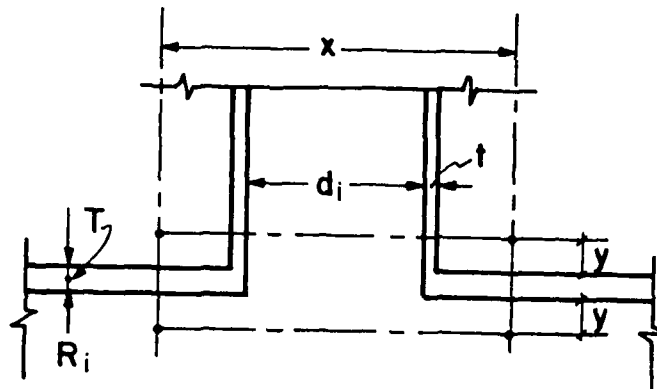
ASME STANDARD

x = Greater of $2d_i$ or $d_i + 2(t + T)$

y = Smaller of $2 1/2 T$ or $2 1/2 t$

Fig. 2.3.1 ASME Standards for Reinforcement Area
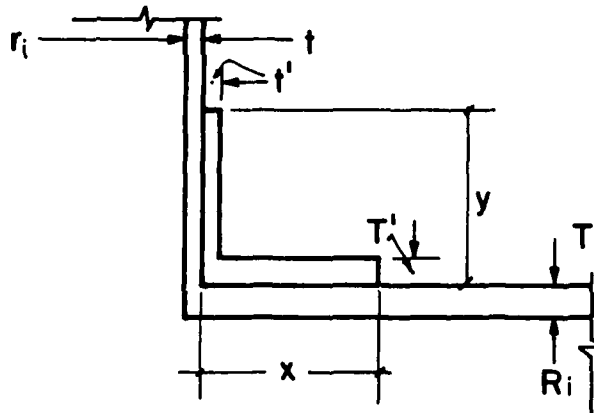
British Standards Institute x = Smaller r_i or $\sqrt{2 \cdot R_i (T + t')}$

$$y = \sqrt{2 \cdot r_i (t + t')}$$

German Standard $x = \sqrt{2 \cdot R_i (T + T')}$

$$y = \sqrt{2 \cdot r_i (t + t')}$$

Fig. 2.3.2 Effective Lengths of Reinforcement

141

ABB'A'   NOZSHELL
BCC'B'   TRANSITION ZONE
BDD'B'   NOZSOL
DFF'D'   CYLSOL
EFF'E'   TRANSITION ZONE
BFF'B'   SOLID
FGHH'GF'   CYLSHELL
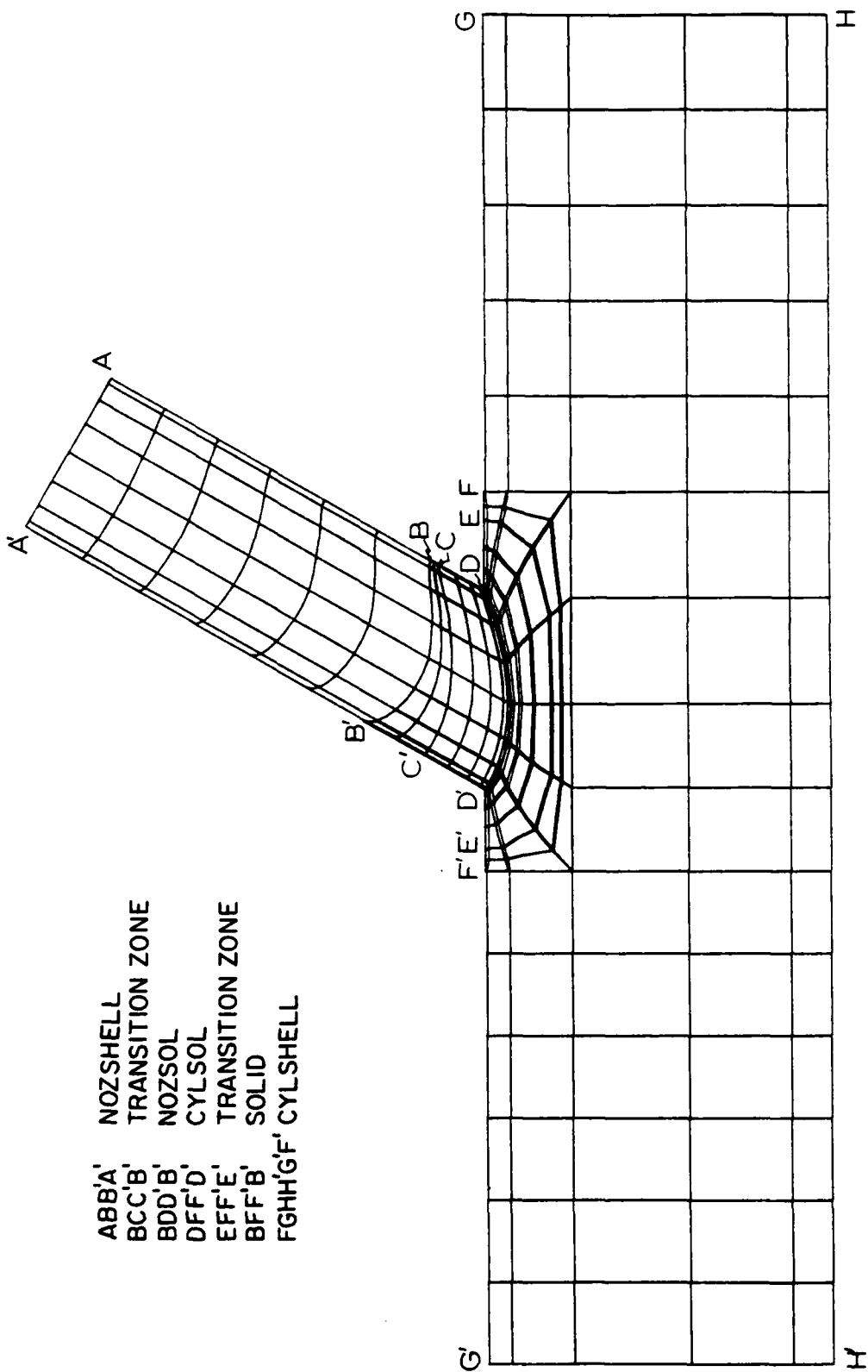
Fig. 3.1 Intersecting Cylinders Finite Element Model

x y z Element local axis
x'y'z' Point local axis

Transformed D.O.F.
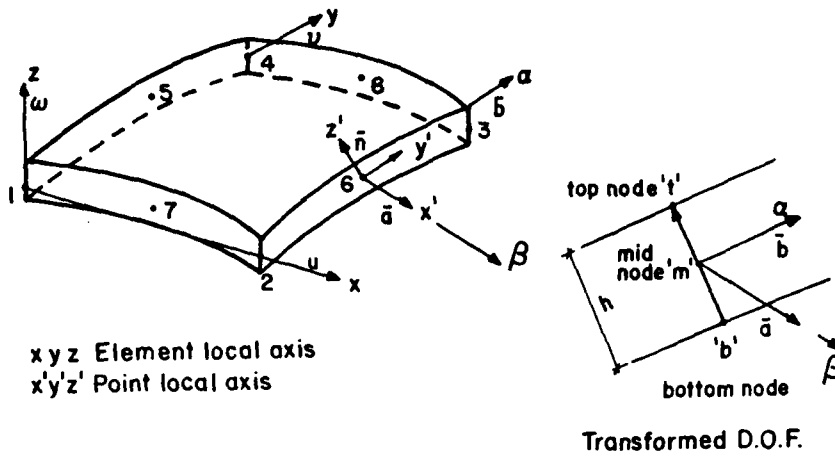
AHMAD'S SHELL ELEMENT

Fig. 3.2 Elements Used in Regions NOZSHELL and CYLSHELL

Q3DISOP

TS16ISOP
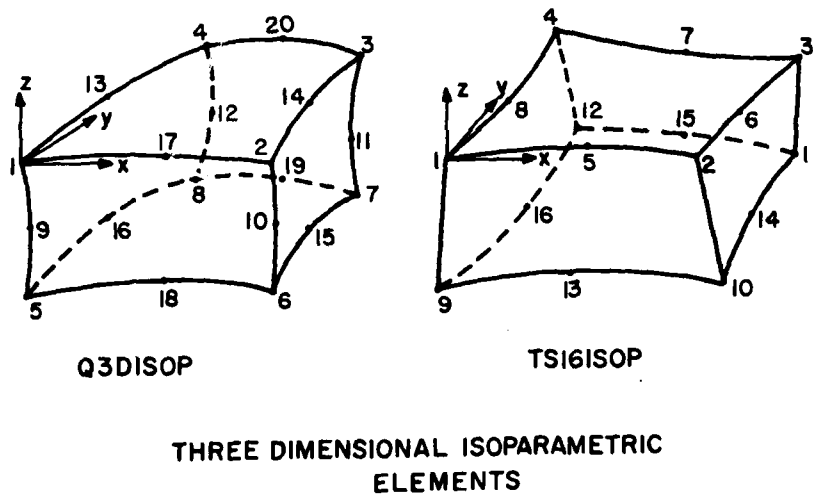
THREE DIMENSIONAL ISOPARAMETRIC
ELEMENTS

Fig. 3.3 Elements Used in Regions NOZSOL and CYLSOL
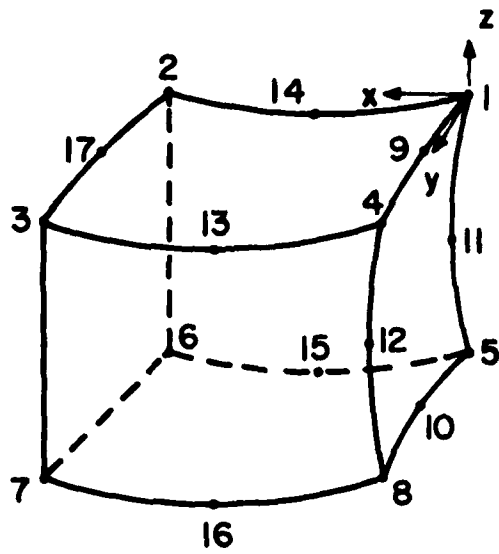
Q3DISTRQ
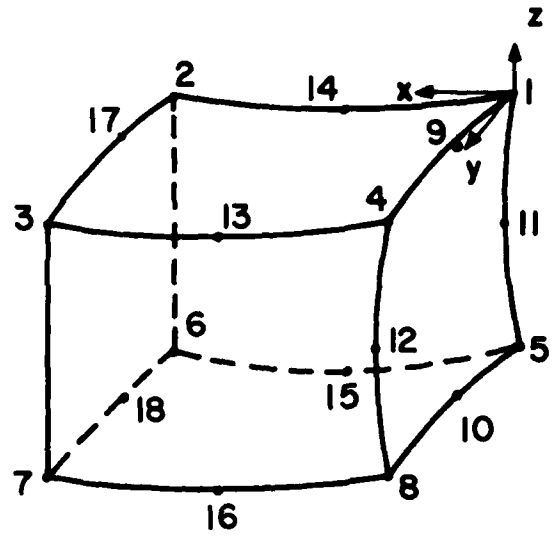
Q3DISTRS

THREE DIMENSIONAL ISOPARAMETRIC
TRANSITION ELEMENTS
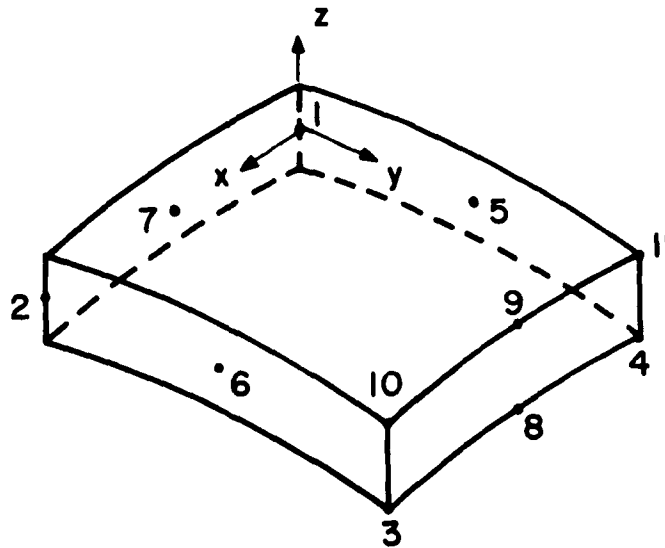
QTSHELL
TRANSITION SHELL ELEMENT

Fig. 3.4 Elements Used in Transition Zone

144

o NODE TO BE CONDENSED
WITH LINEAR IDEALIZATION
THROUGH THICKNESS

a) 16 NODED ISOPARAMETRIC ELEMENTS

b) 20 NODED ISOPARAMETRIC ELEMENTS
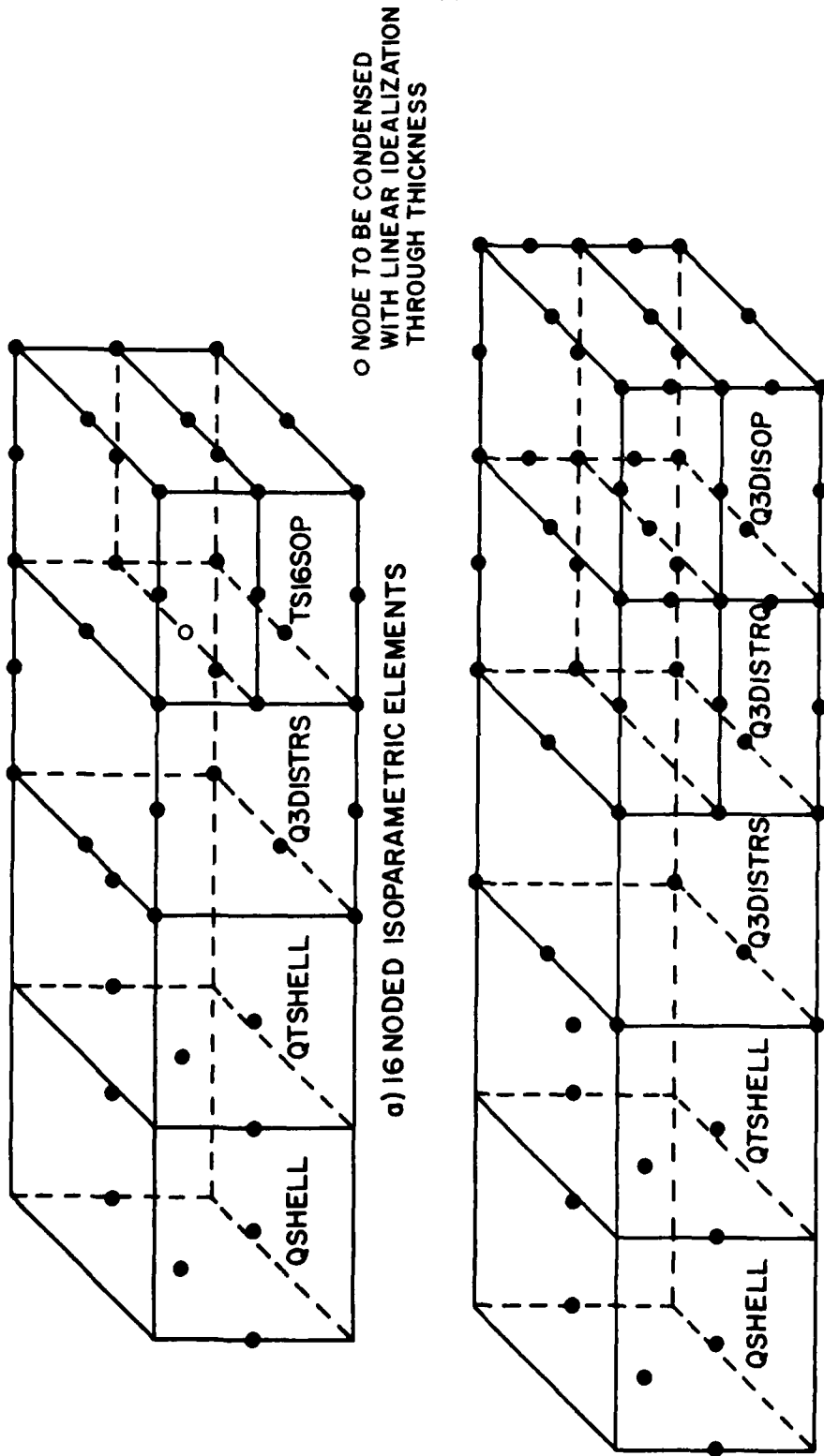
Fig. 3.5   Transition Element Array to Achieve Layering Scheme
in Region SOLID
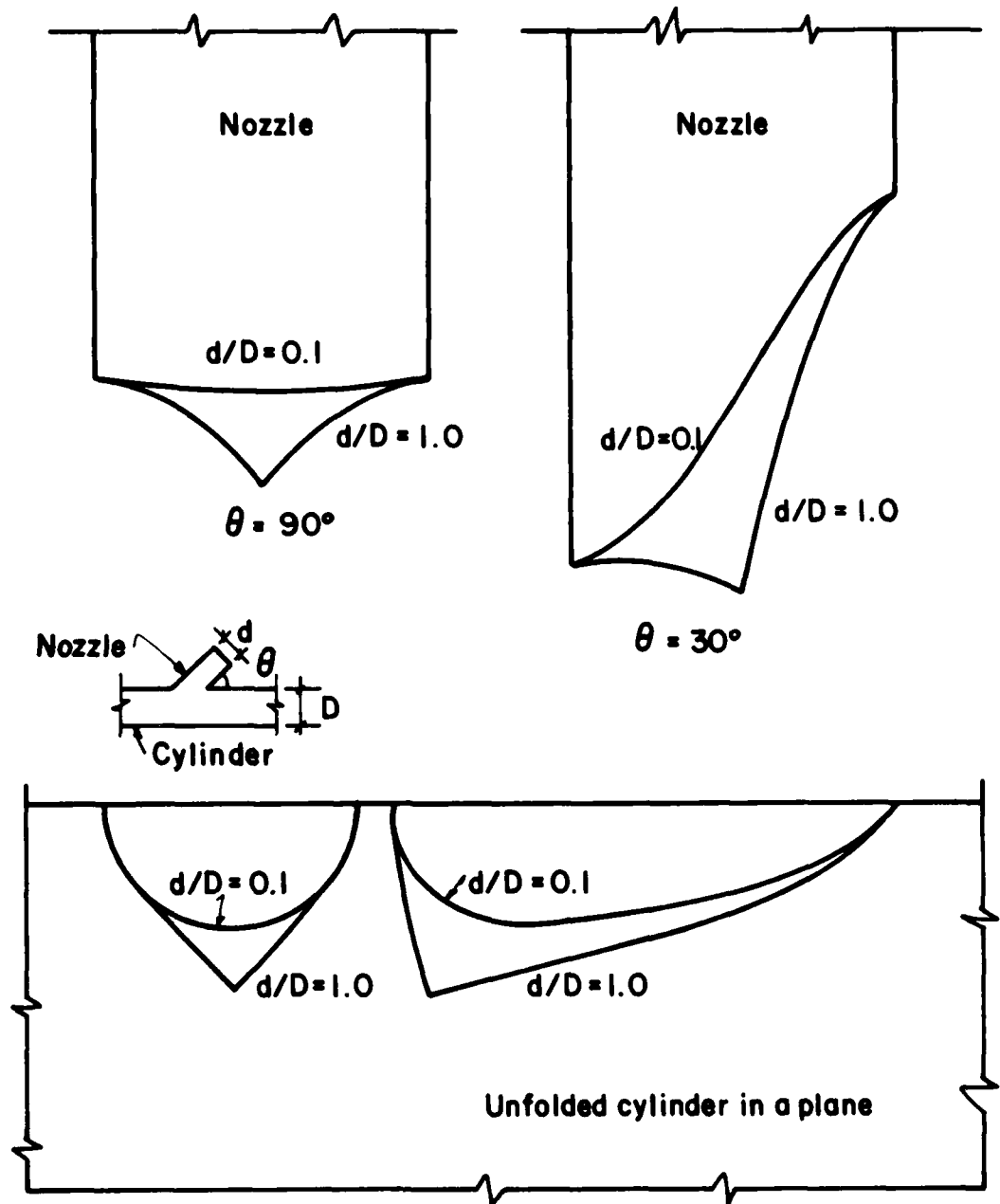
Fig. 3.6   Influence of Aspect Ratios and Angle of Intersection on
Shapes of Curves of Intersection
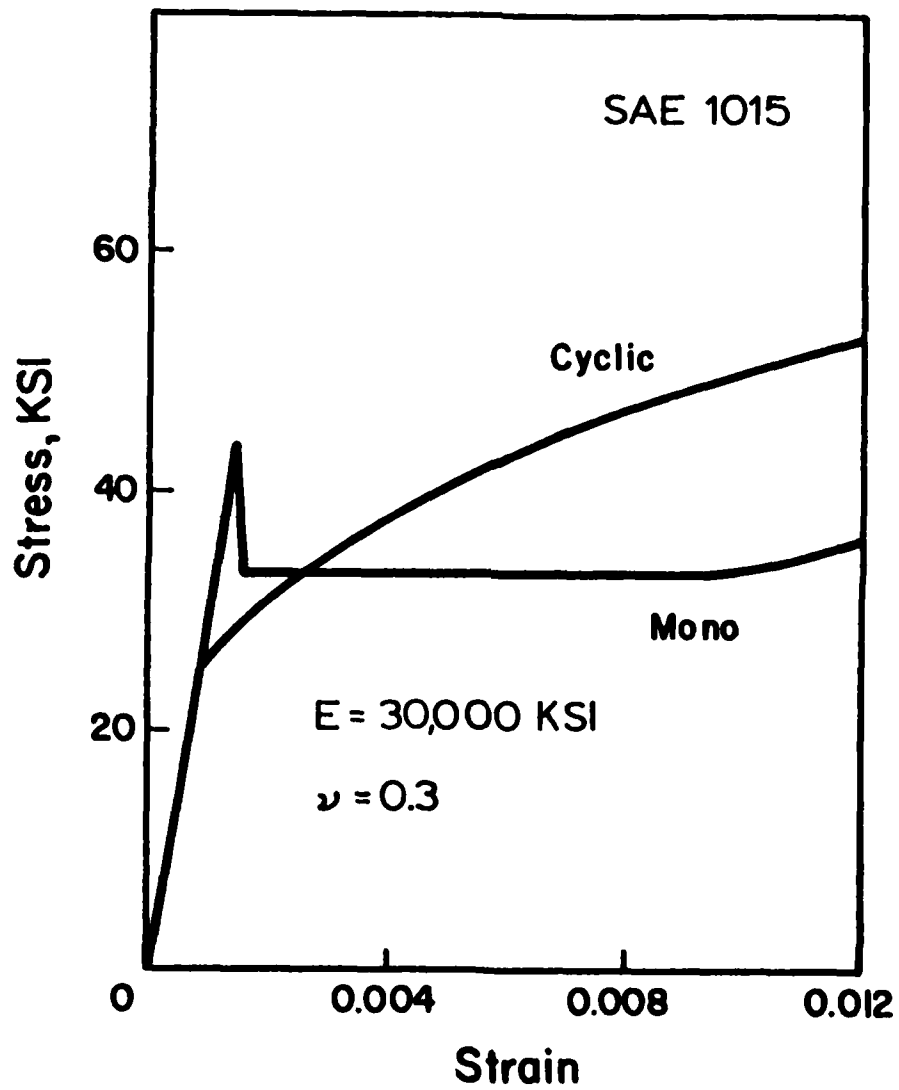
Fig. 4.1 Uniaxial Monotonic and Cyclic Stress-Strain Curve
          for SAE 1015
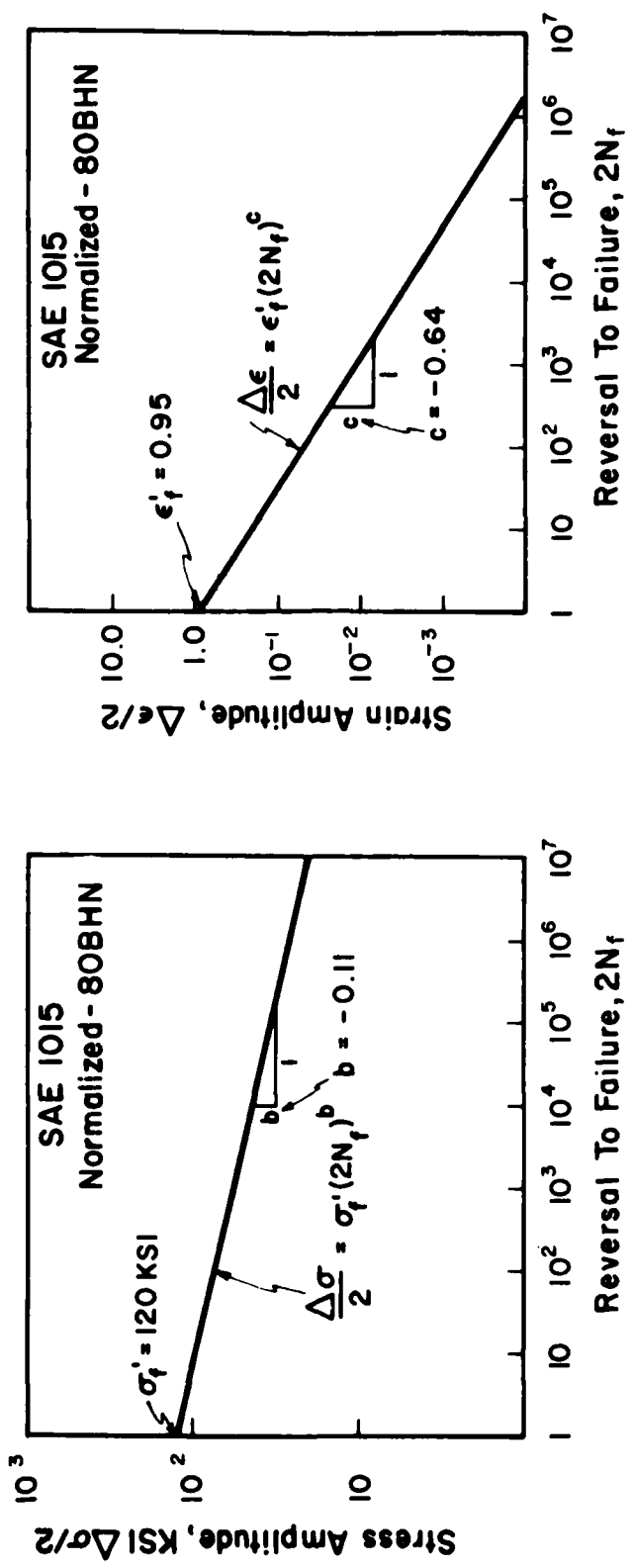
Strain Amplitude - Fatigue Life

Stress Amplitude - Fatigue Life

Fig. 4.2 Fatigue Life Curves for SAE 1015
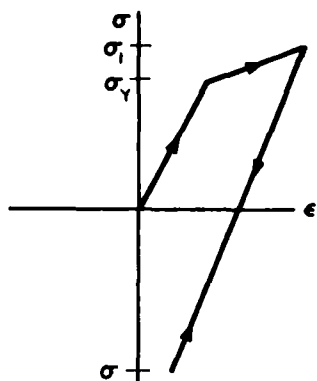
$\sigma - \epsilon$ loop for constant stress
amplitude – isotropic hardening
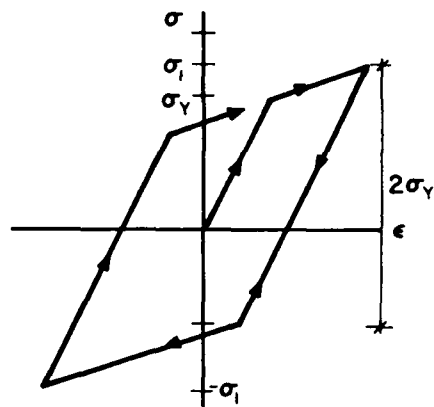
$\sigma - \epsilon$ loop for constant stress
amplitude - kinematic hardening

Fig. 5.1   Isotropic Hardening   Fig. 5.2   Kinematic Hardening
            Material Response   Material Response
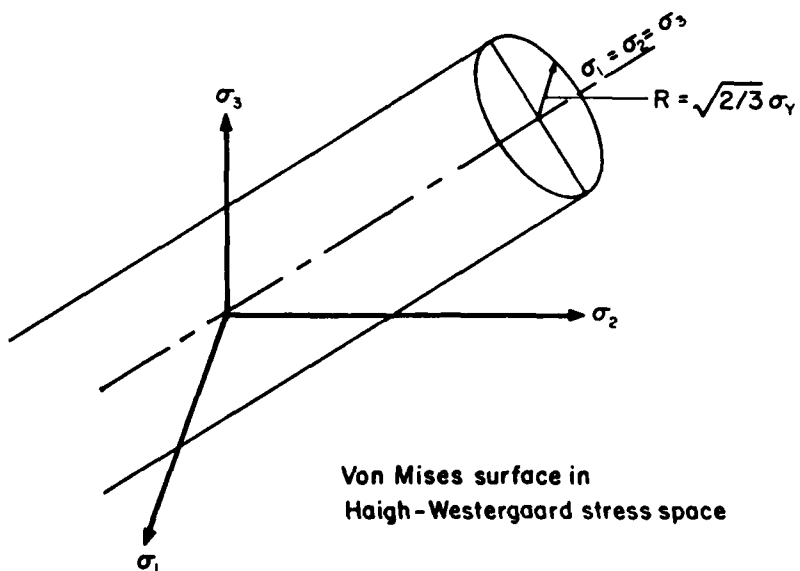
Von Mises surface in
Haigh-Westergaard stress space

Fig. 5.3   Von Mises Yield Cylinder
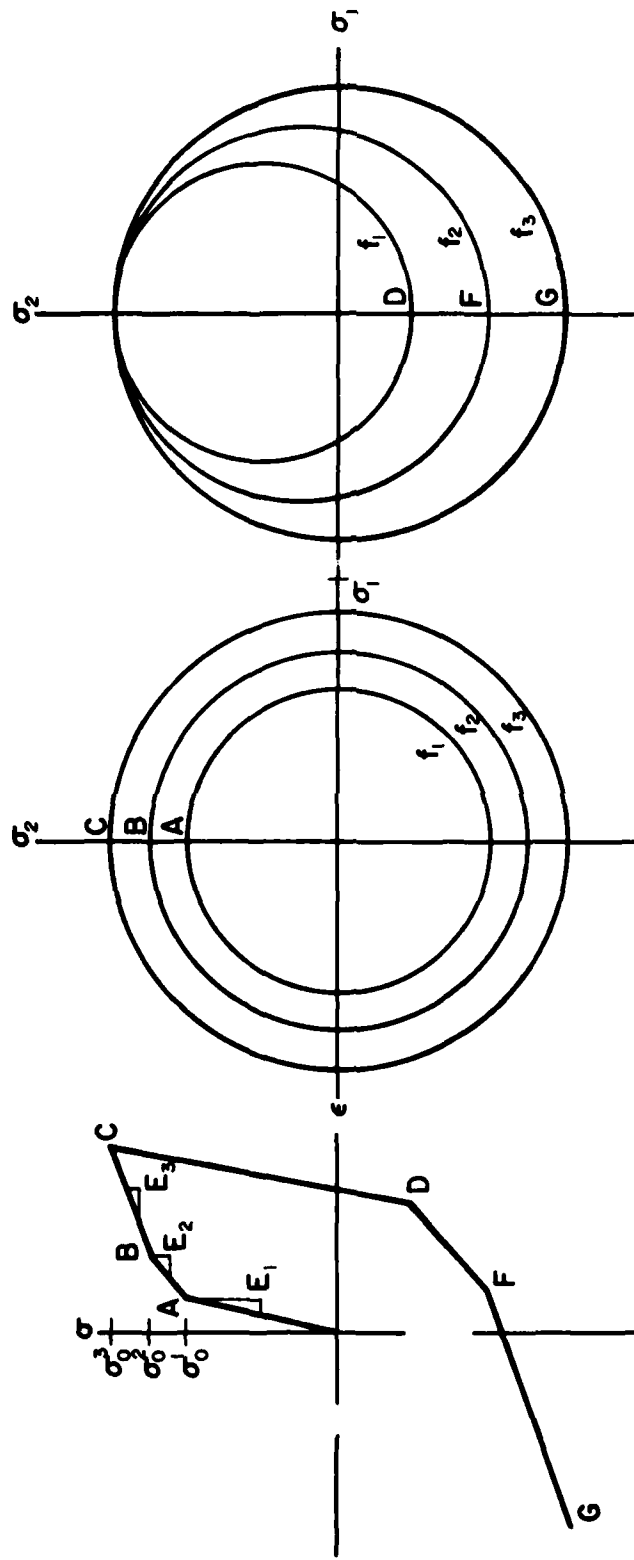
Uniaxial Stress-Strain
Curve

Fields of Work Hardening Moduli
and Corresponding Hyper-Surfaces
for a Virgin Material

Hyper-Surfaces at the End of
Loading

Fig. 5.4   Schematic Representation of Kinematic Hardening
Material Model
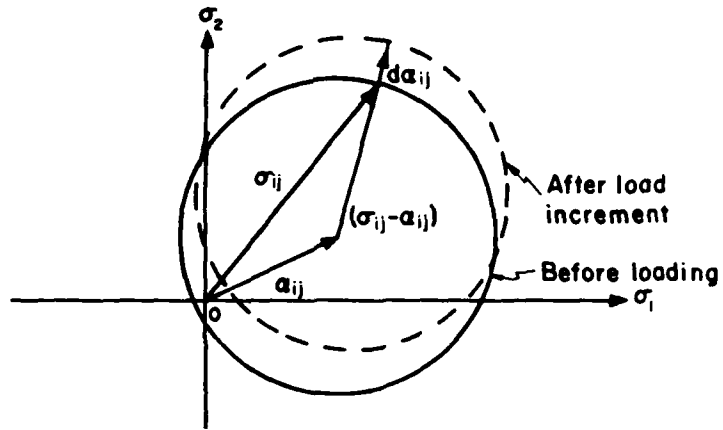
Fig. 5.5 Hyper-Surface Translation for Ziegler Material Model
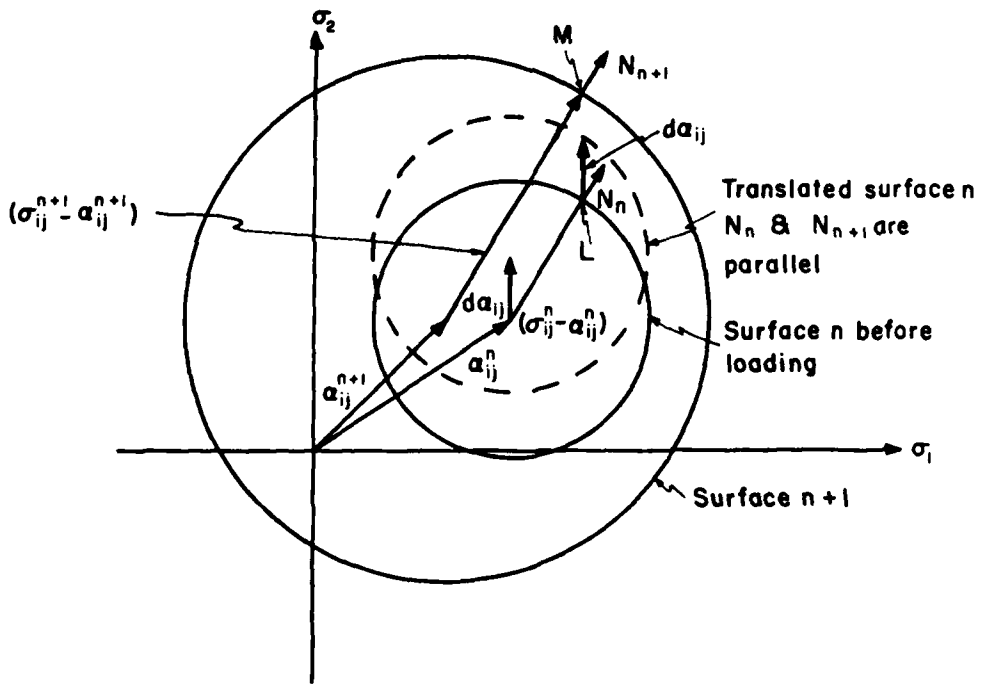
Fig. 5.6 Hyper-Surface Translation for Mroz Material Model
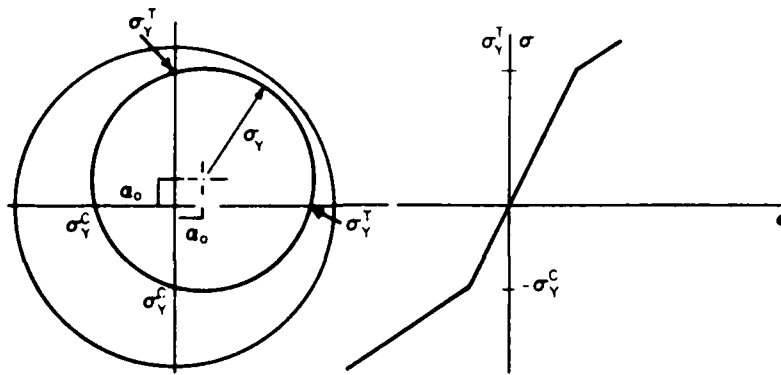
Fig. 5.7   Hyper Surface for Initial Anisotropy

AB Tension
CD Compression
AD, BC Transition
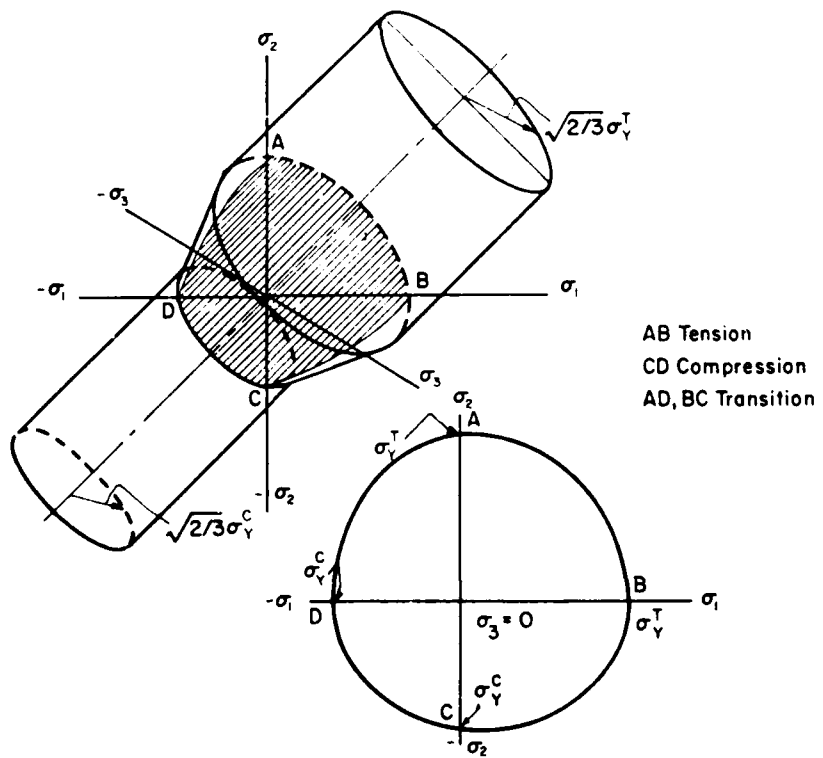
Fig. 5.8   Hyper Surface for Permanent Anisotropy
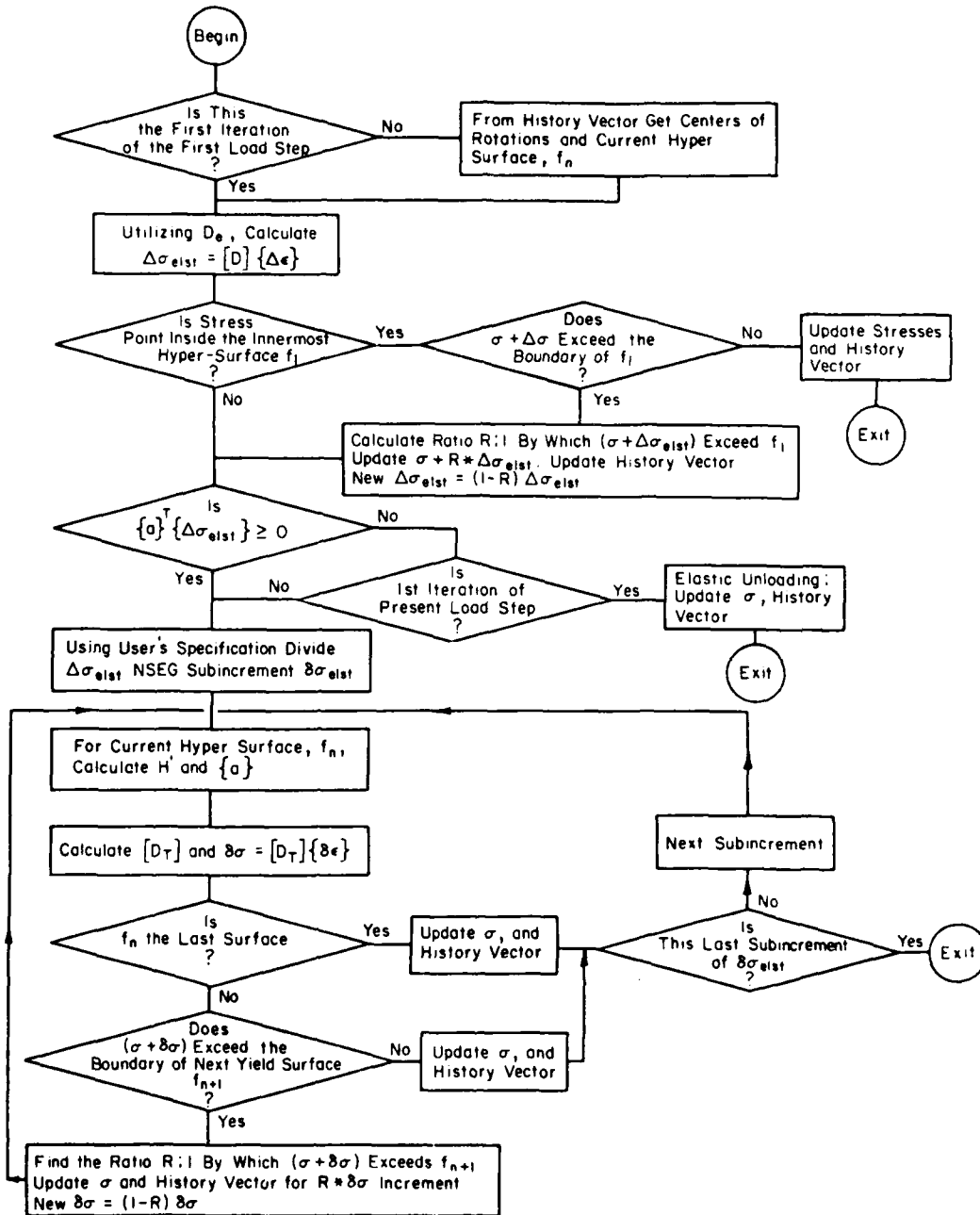
Fig. 5.9 Solution Process for Kinematic Material Model

Fig. 6.1.2 Outward Displacements of
Thick Walled Cylinder

Fig. 6.1.1 Thick Walled Cylinder Dimensions,
Material Properties and
Finite Element Model

154
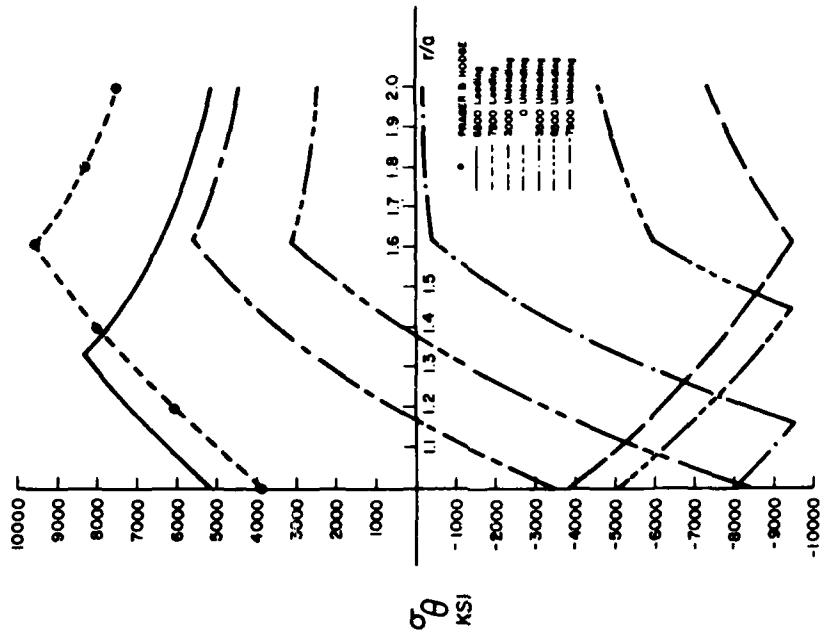
Fig. 6.1.4 Circumferential Stress Distribution for Thick Walled Cylinder
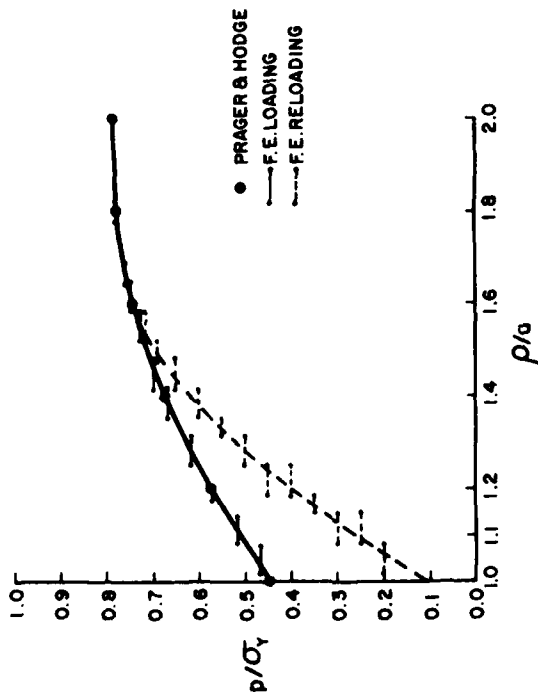
Fig. 6.1.3 Progression of the Yield Envelope for Thick Walled Cylinder

Fig. 6.1.6 Axial Stress Distribution
for Thick Walled Cylinder

Fig. 6.1.5 Radial Stress Distribution
for Thick Walled Cylinder
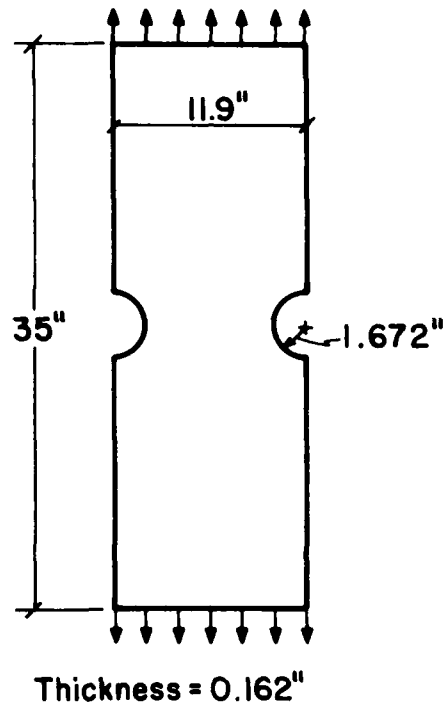
Fig. 6.2.1   Notched Plate Dimensions and Geometry
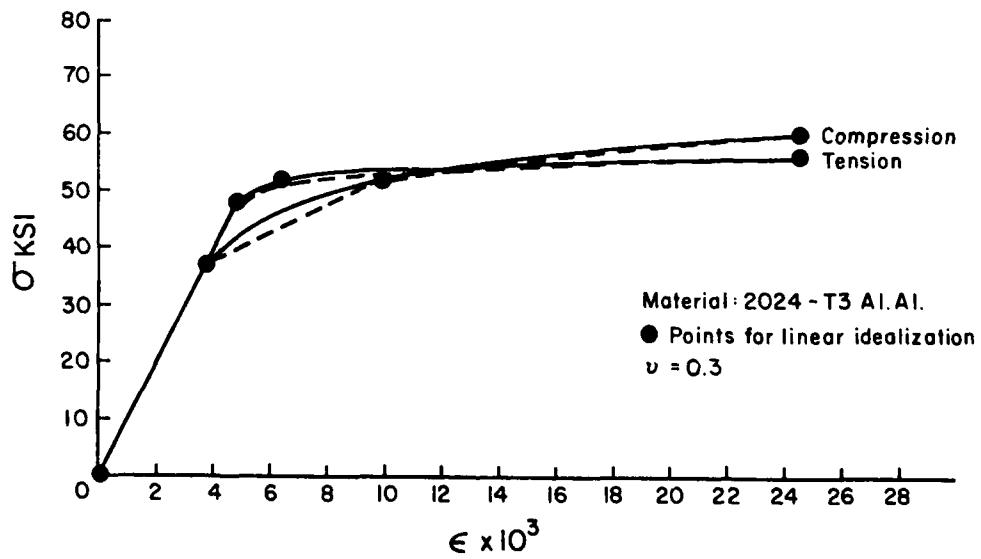
Fig. 6.2.2   Material Properties for Notched Plate
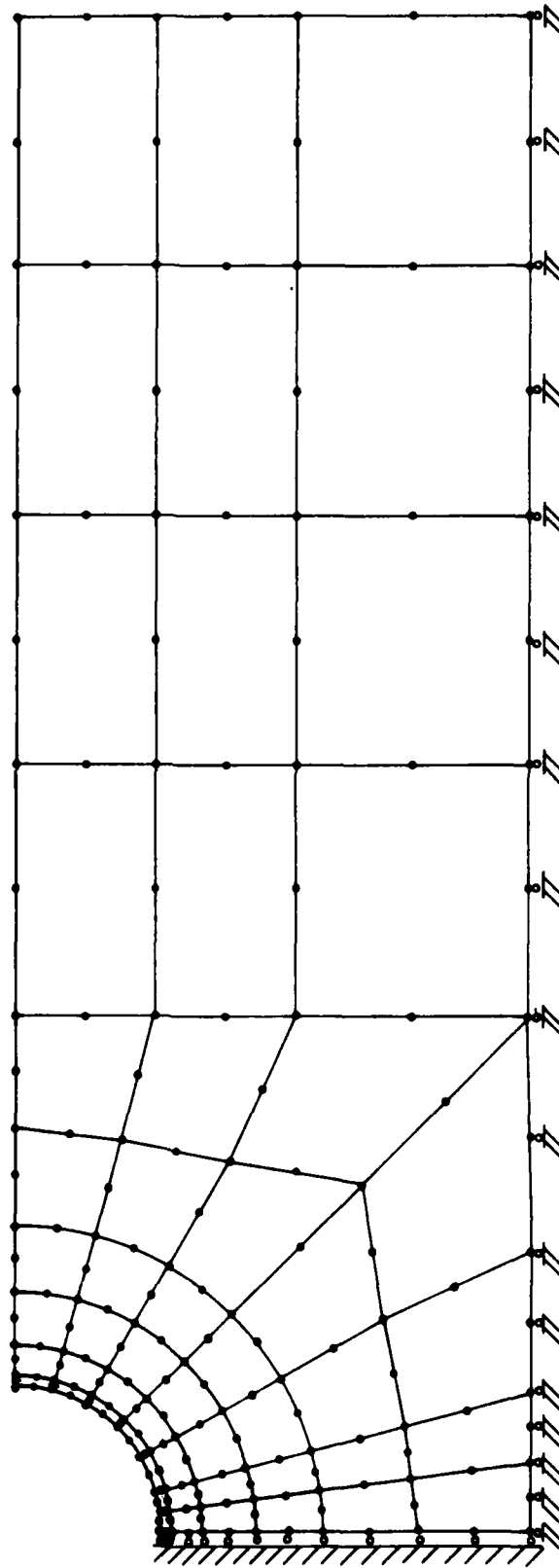
Fig. 6.2.3   Notched Plate Finite Element Models
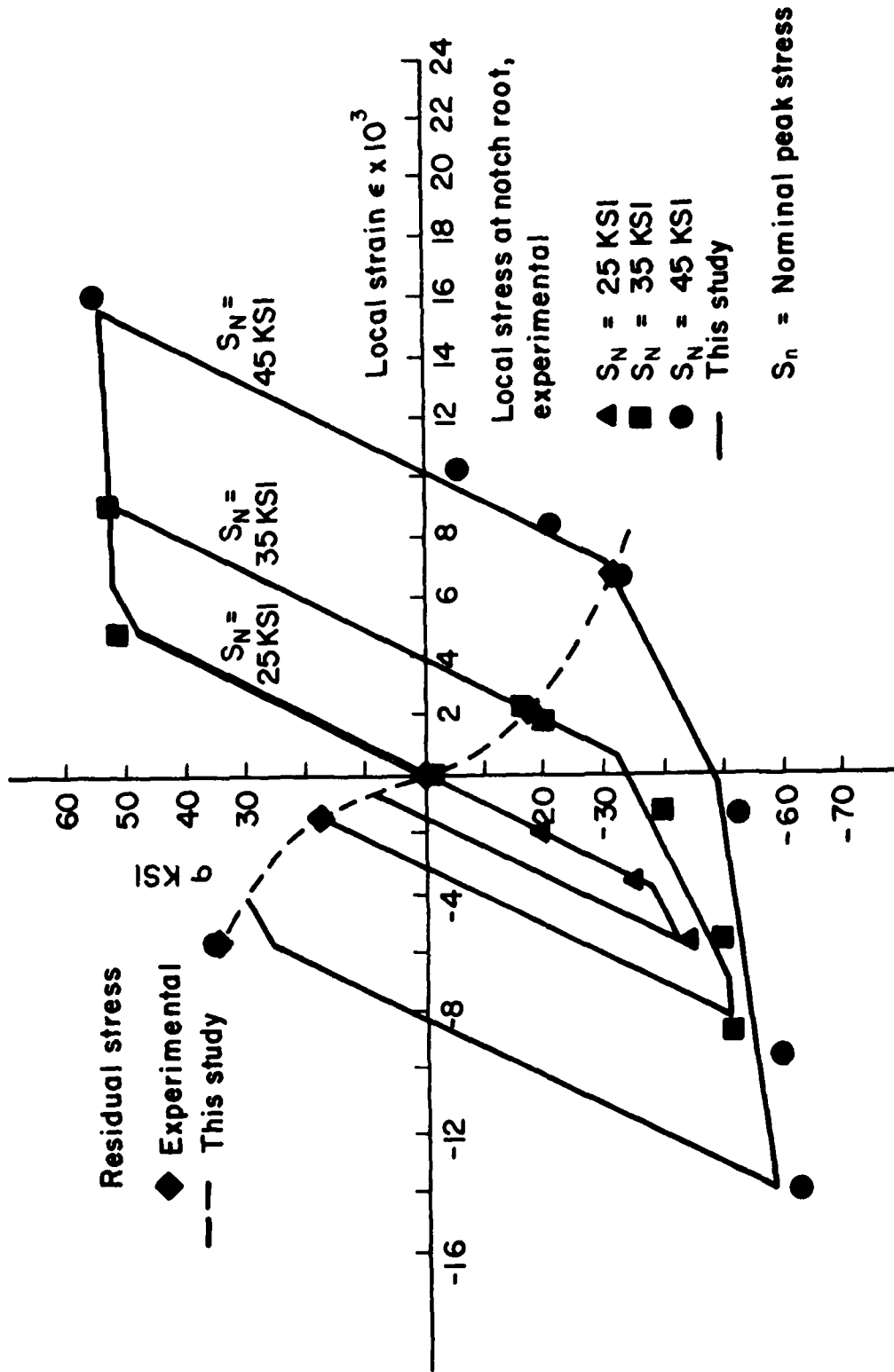
Fig. 6.2.4 Notch-Root Stress-Strain Response for Notched Plate
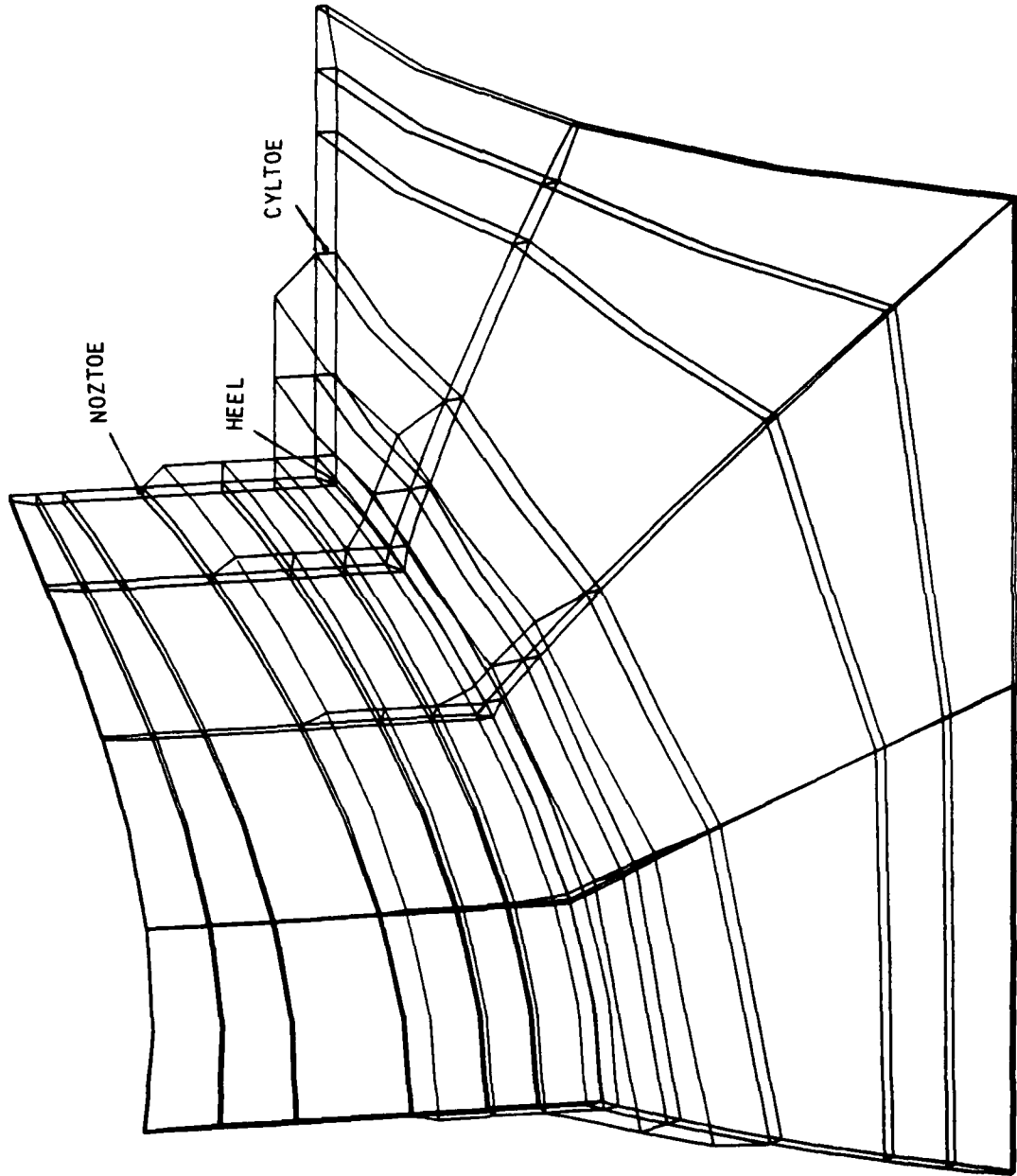
Fig. 6.3.1 Typical Finite Element Discretization of Region SOLID
Reinforced Cylinder Intersection
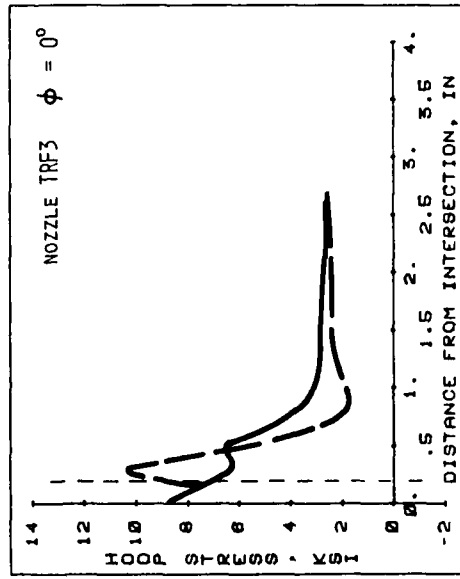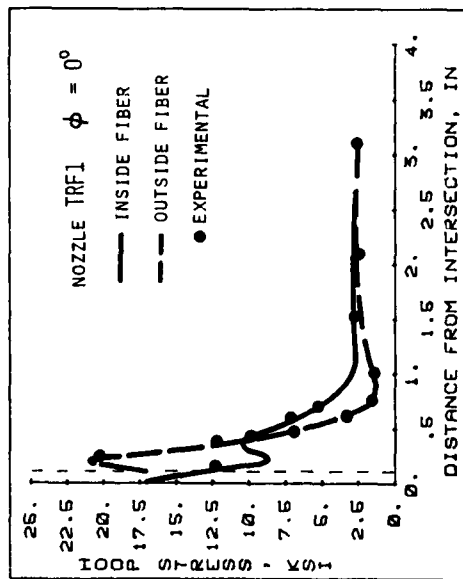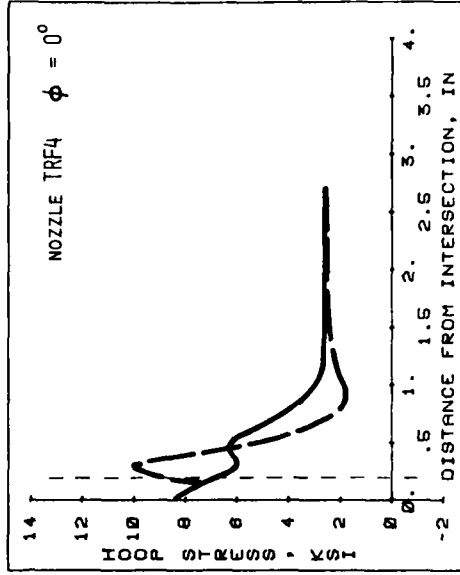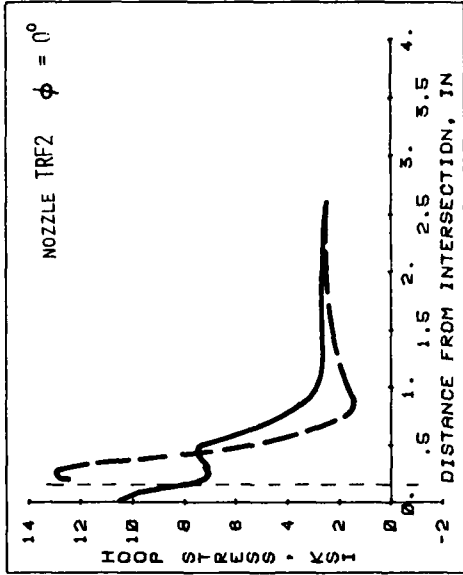
Fig. 6.3.2 Hoop Stress in Nozzle at $\phi = 0^O$
Reinforced Cylinder Intersection

161

Fig. 6.3.2 (contd.) Hoop Stress in Nozzle at $\phi = 0^o$ Reinforced Cylinder Intersection

162

Fig. 6.3.2 (contd.) Hoop Stress in Nozzle at $\phi = 0^{o}$ Reinforced Cylinder Intersection

163

Fig. 6.3.3 Axial Stress in Nozzle at $\phi = 0^{\circ}$
Reinforced Cylinder Intersection

Fig. 6.3.3 (contd.) Axial Stress in Nozzle at $\phi = 0^O$ Reinforced Cylinder Intersection

Fig. 6.3.3 (contd.) Axial Stress in Nozzle at $\phi = 0^0$ Reinforced Cylinder Intersection
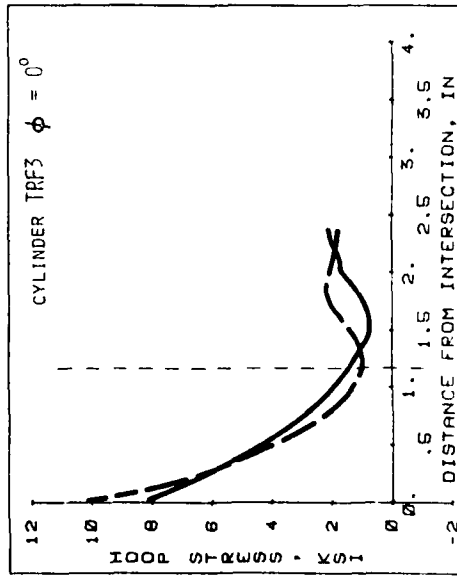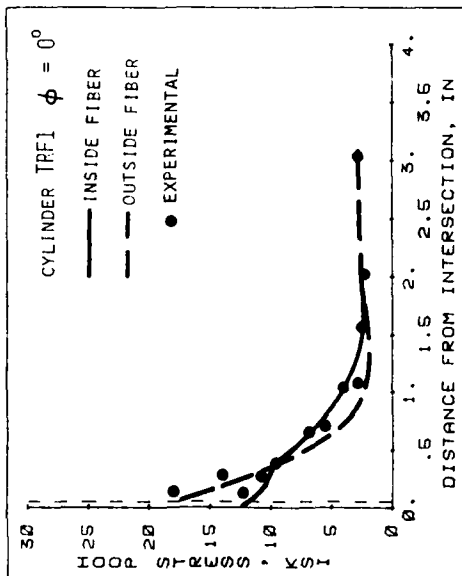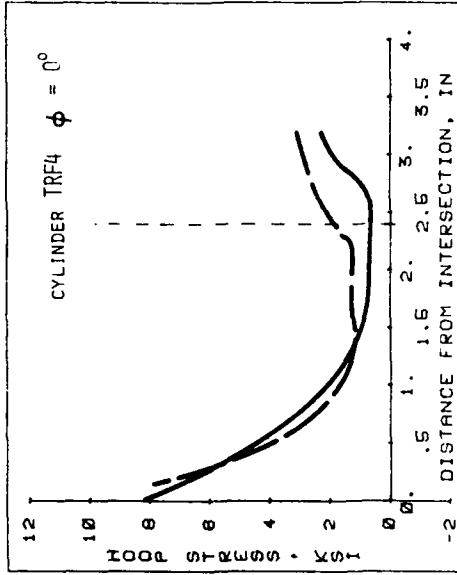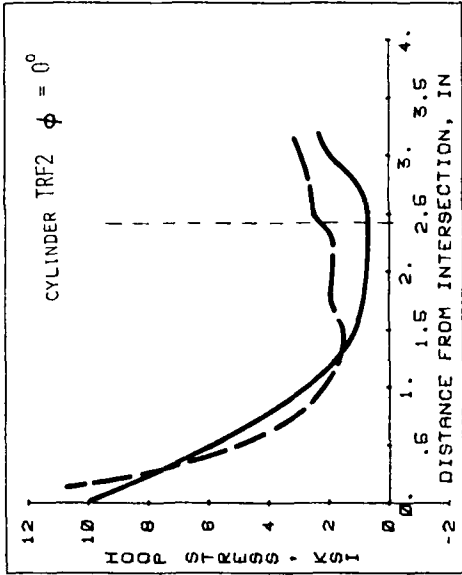
Fig. 6.3.4 Hoop Stress in Cylinder at $\phi = 0^o$
Reinforced Cylinder Intersection
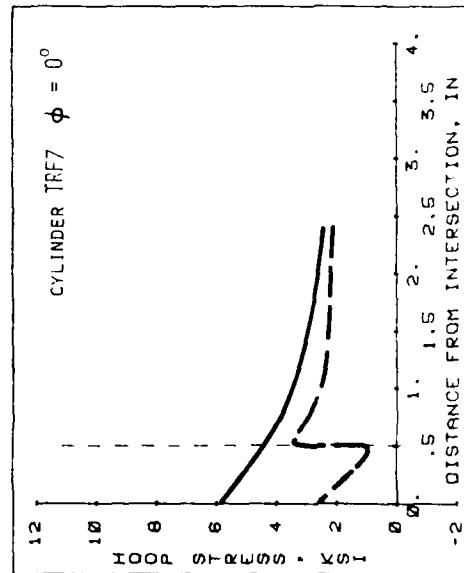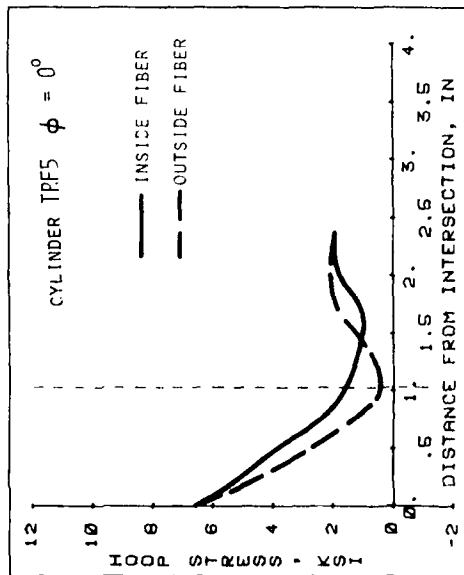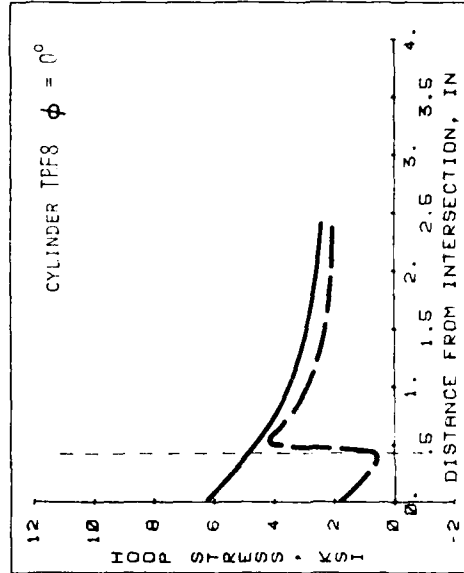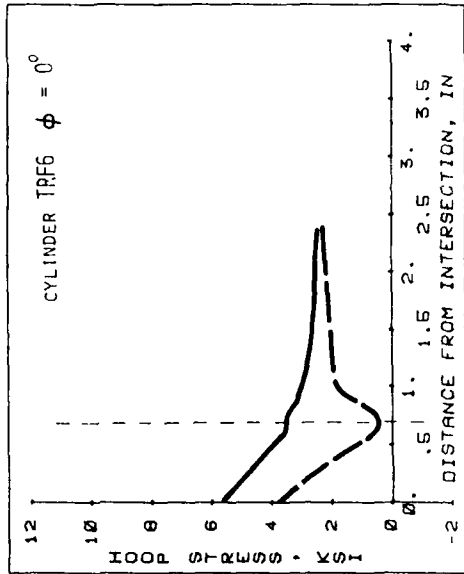
Fig. 6.3.4 (contd.)   Hoop Stress in Cylinder at $\psi = 0^{\circ}$
Reinforced Cylinder Intersection
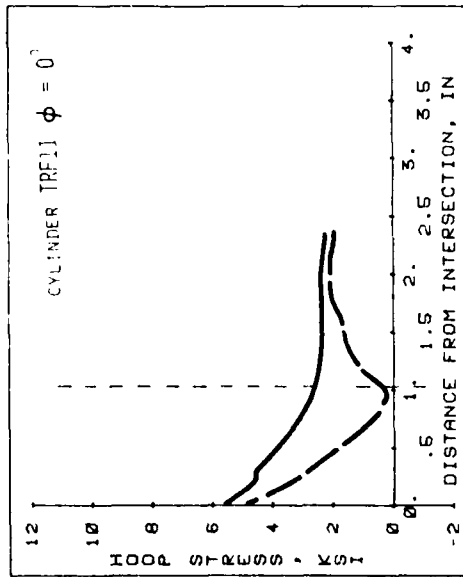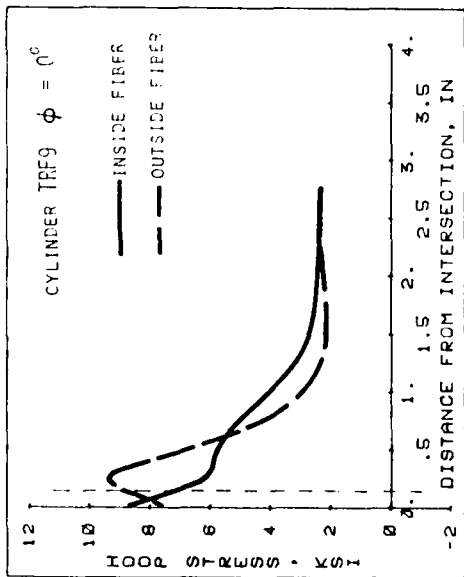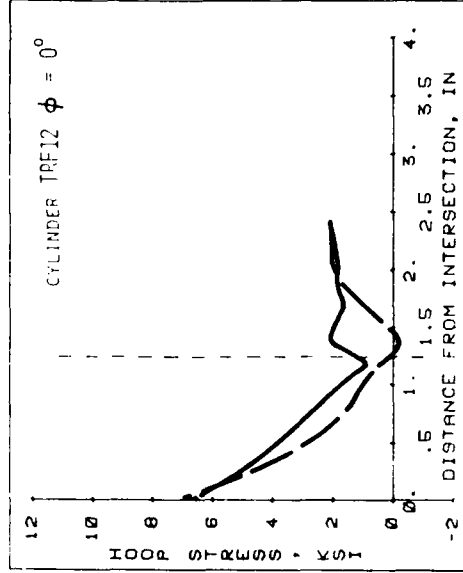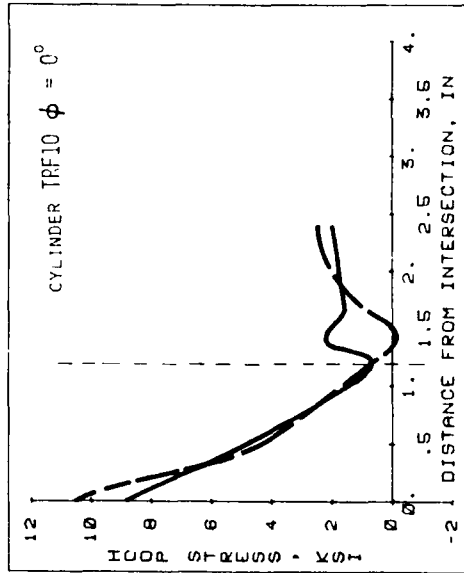
Fig. 6.3.4 (contd.) Hoop Stress in Cylinder at $\phi = 0^{\circ}$
Reinforced Cylinder Intersection
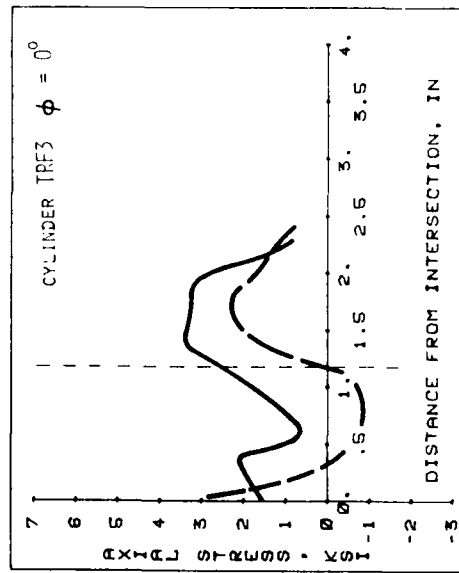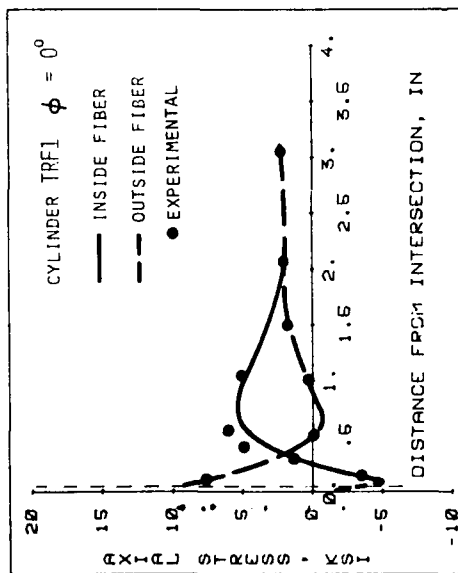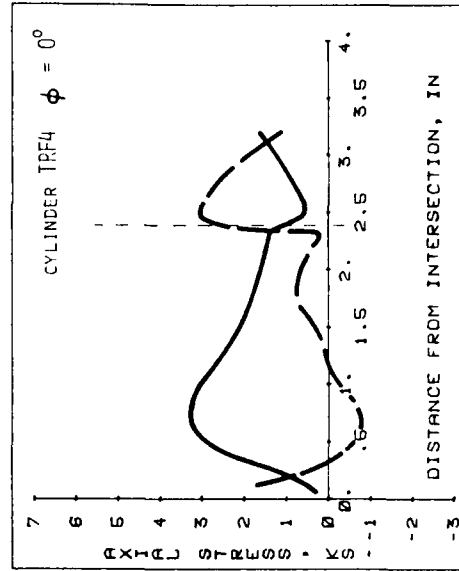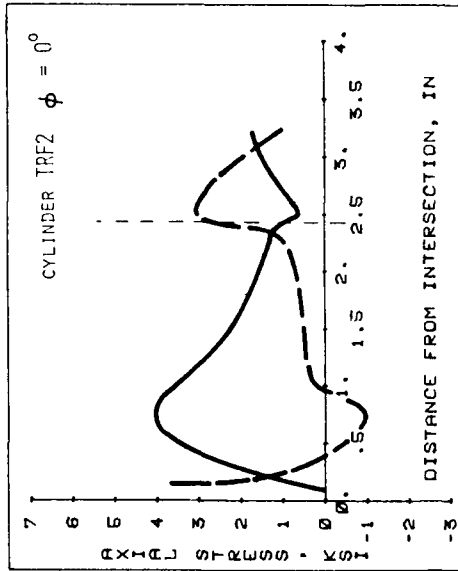
Fig. 6.3.5 Axial Stress in Cylinder at $\phi = 0^0$
Reinforced Cylinder Intersection
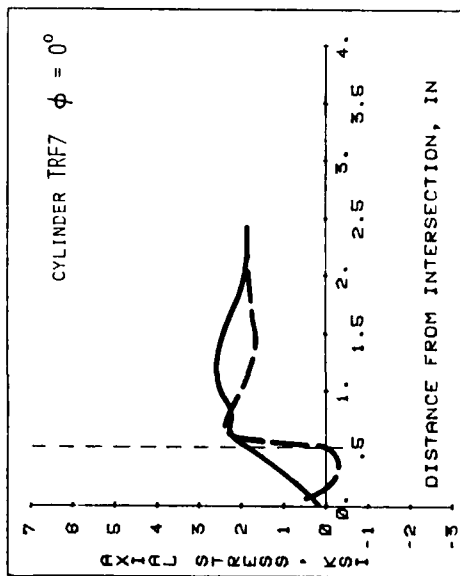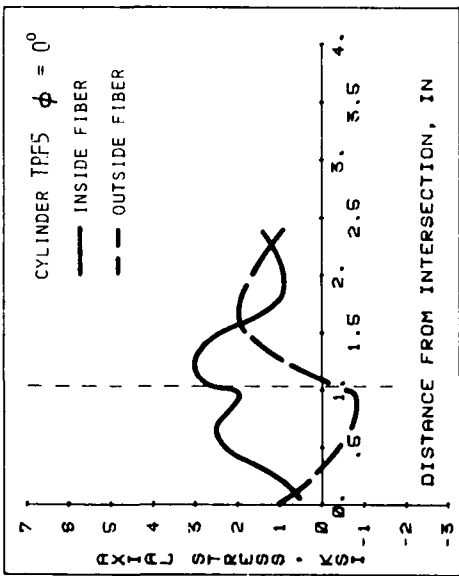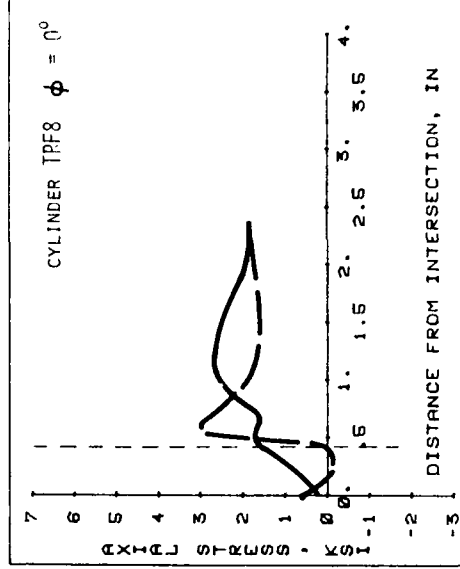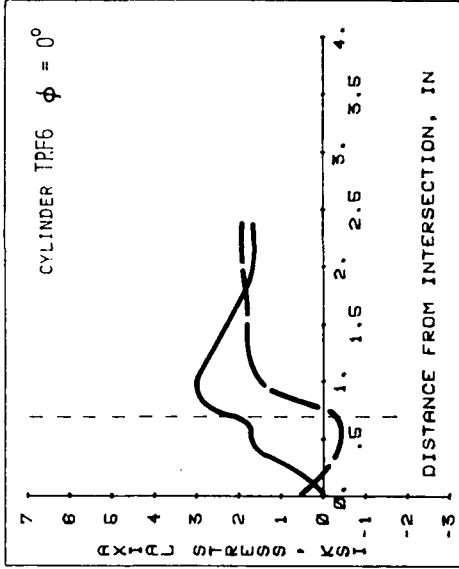
Fig. 6.3.5 (contd.) Axial Stress in Cylinder at $\phi = 0°$
Reinforced Cylinder Intersection
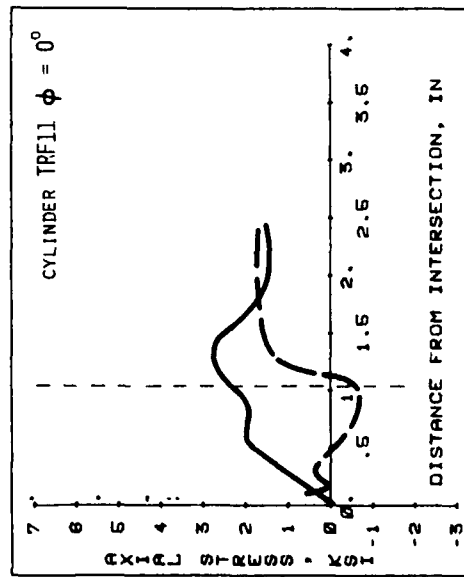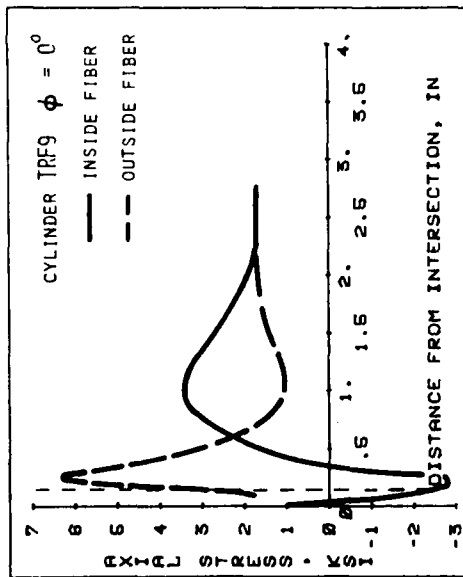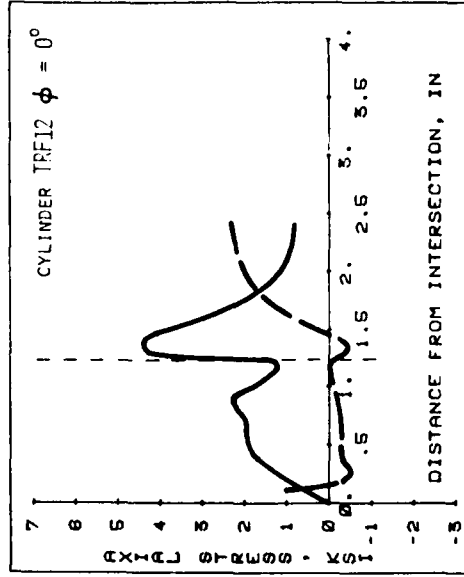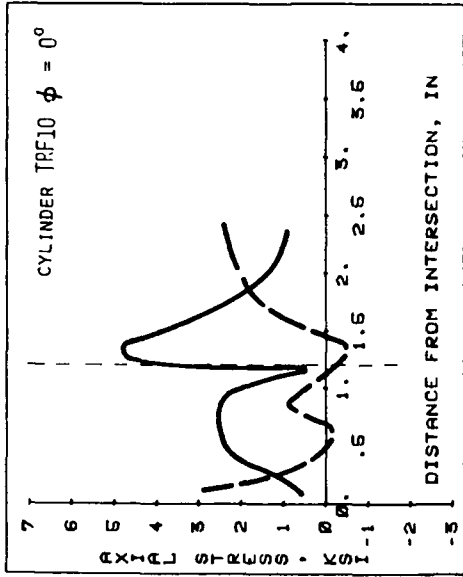
Fig. 6.3.5 (contd.) Axial Stress in Cylinder at $\phi = 0^o$ Reinforced Cylinder Intersection
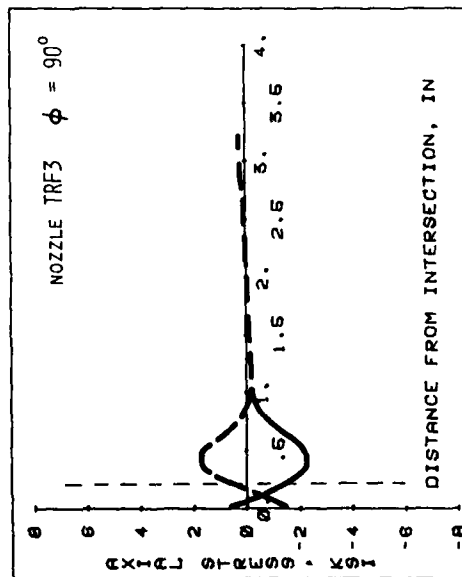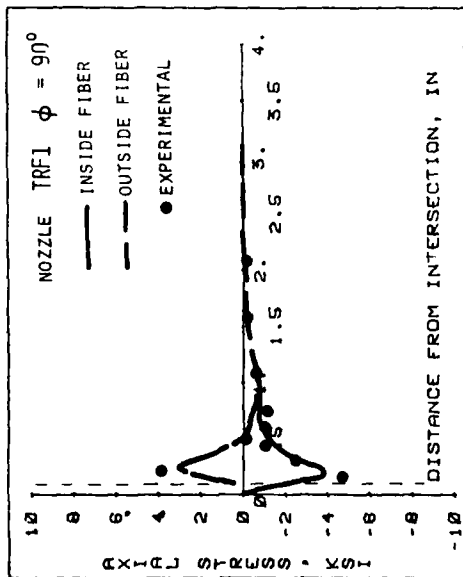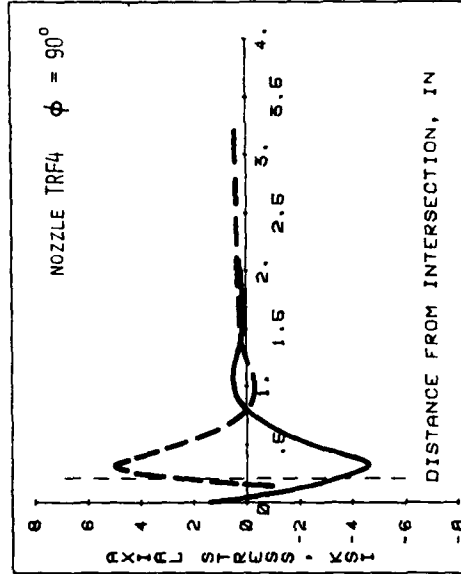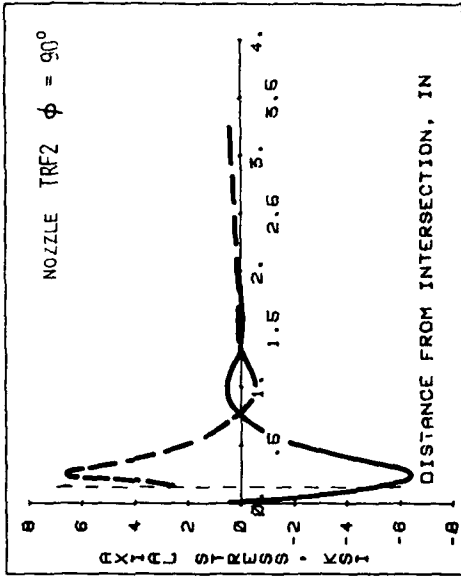
Fig. 6.3.6   Axial Stress in Nozzle at $\phi = 90^{\circ}$
Reinforced Cylinder Intersection
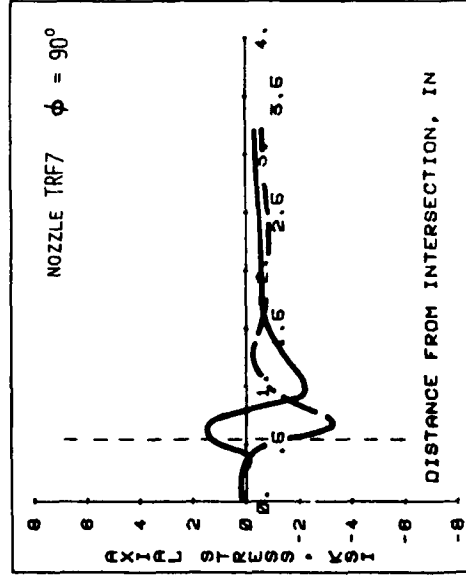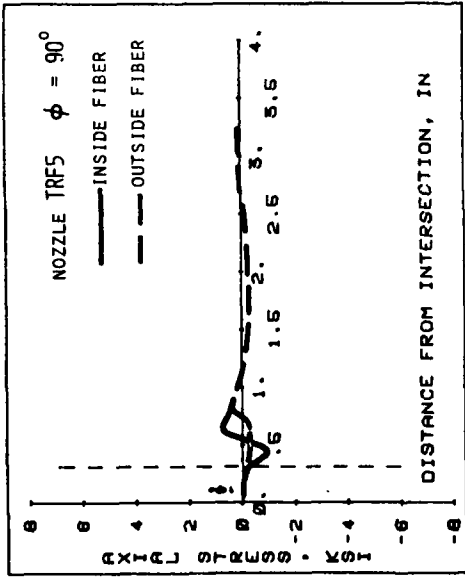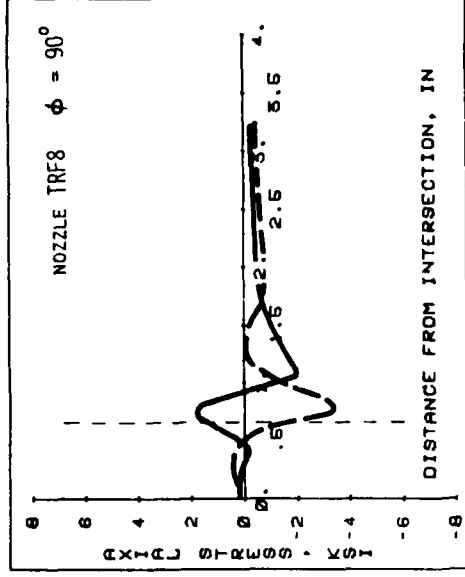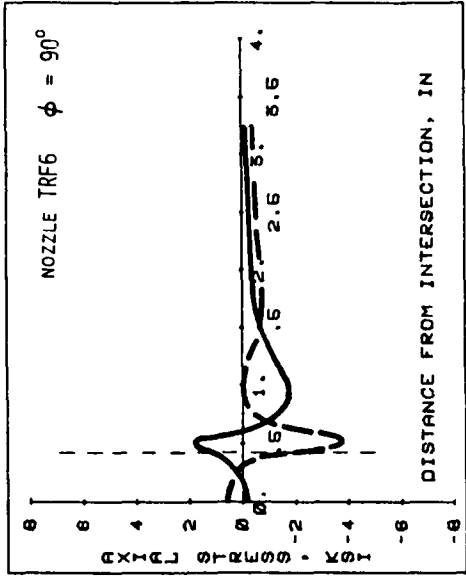
Fig. 6.3.6 (contd.) Axial Stress in Nozzle at $\phi = 90^{\circ}$
Reinforced Cylinder Intersection

Fig. 6.3.6 (contd.) Axial Stress in Nozzle at $\phi = 90^{\circ}$ Reinforced Cylinder Intersection

175
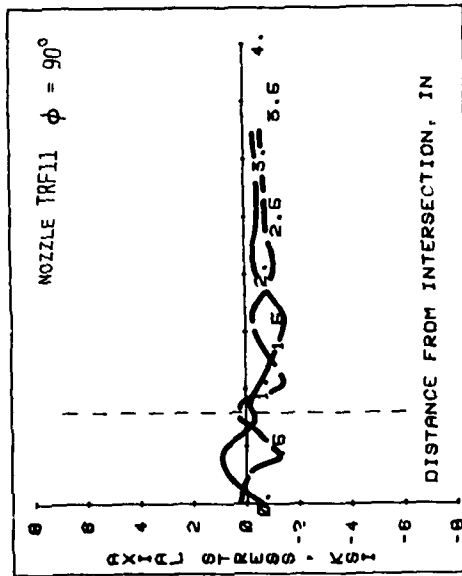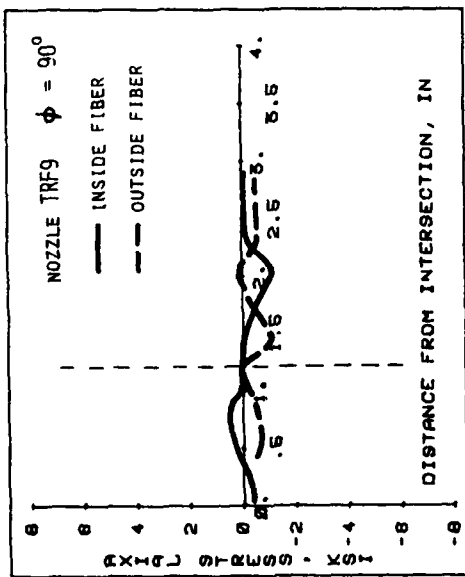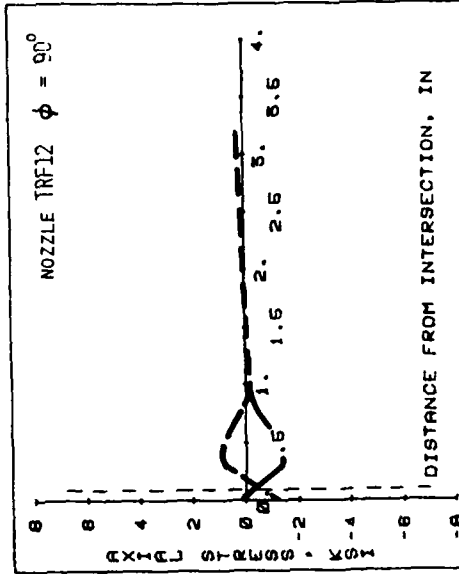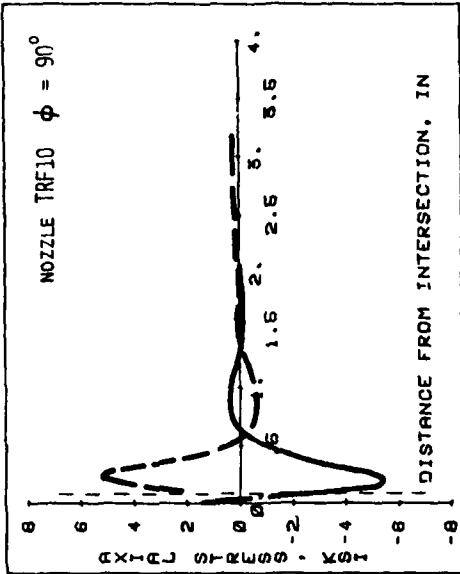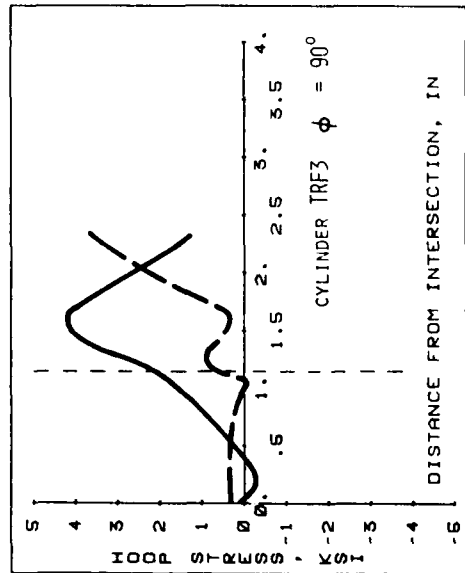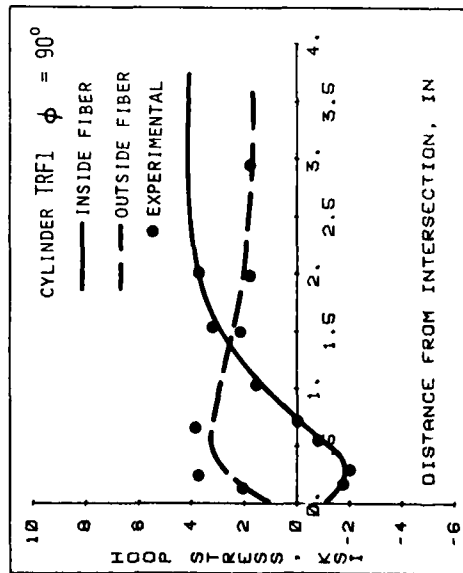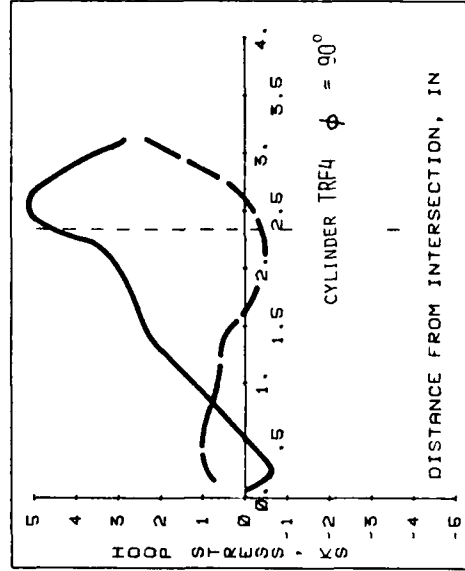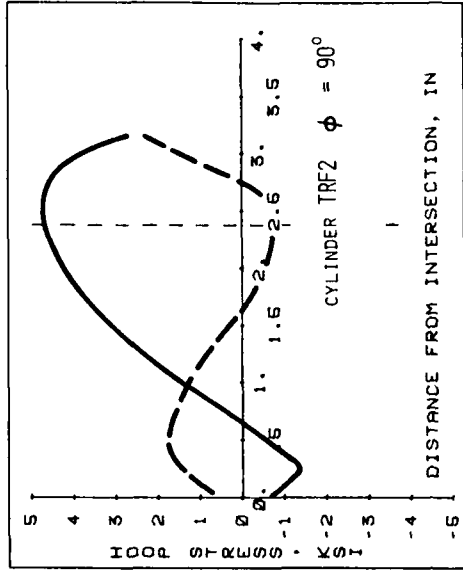
Fig. 6.3.7 Hoop Stress in Cylinder at $\phi = 90^o$
Reinforced Cylinder Intersection

176
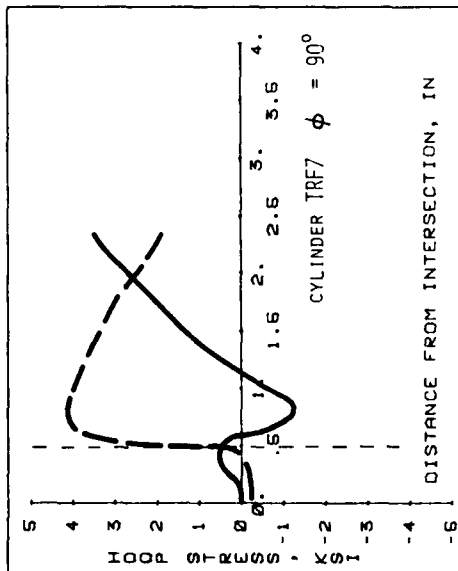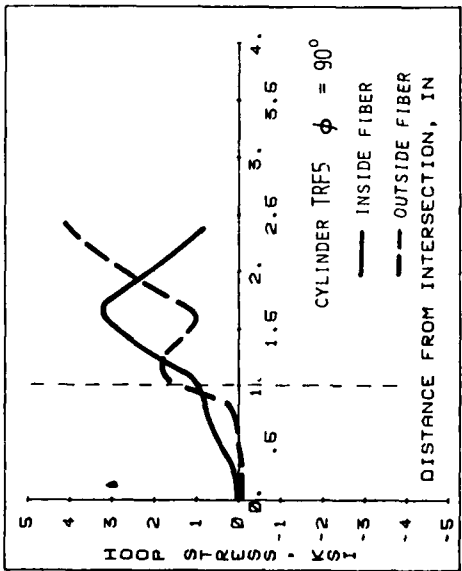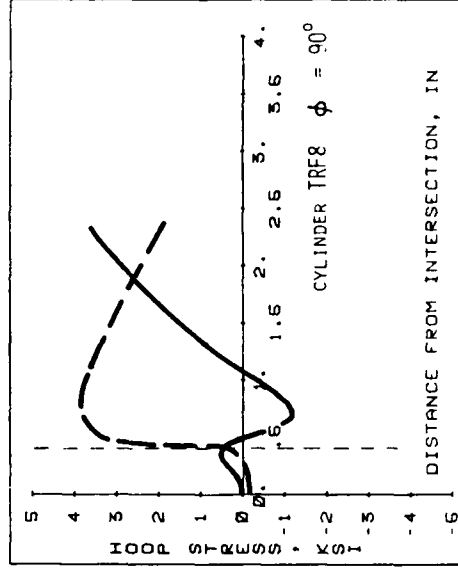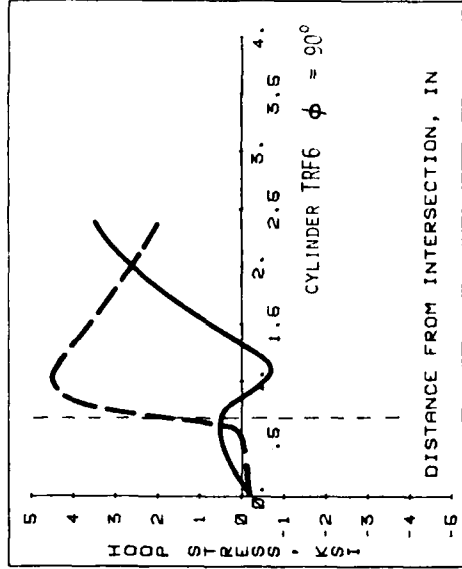
Fig. 6.3.7 (contd.)   Hoop Stress in Cylinder at $\phi = 90°$
Reinforced Cylinder Intersection
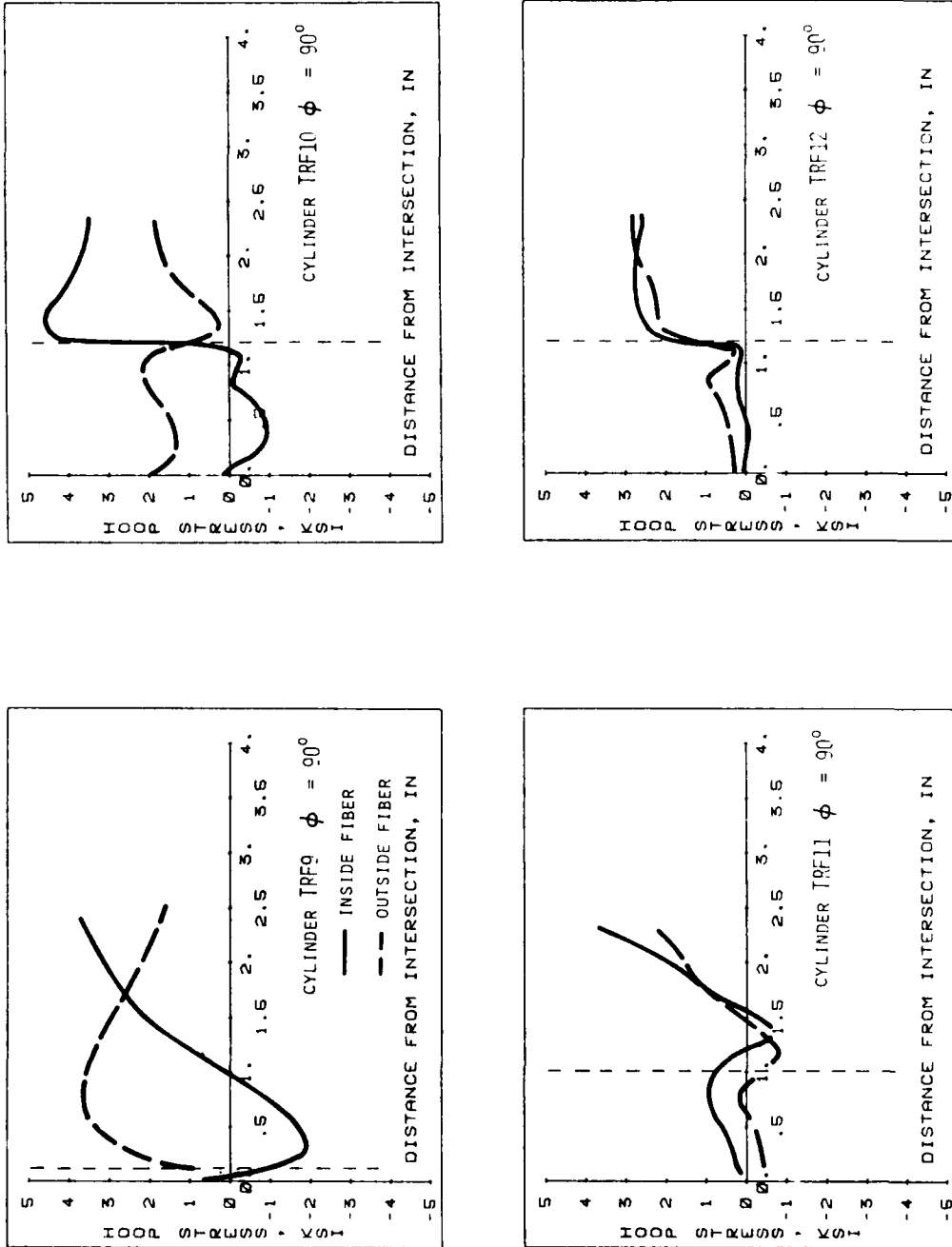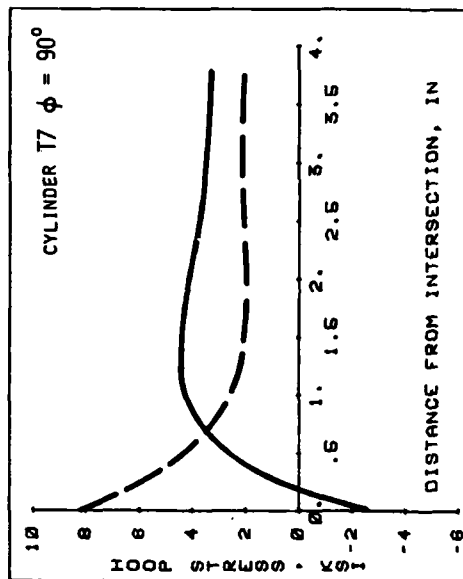
Fig. 6.3.7 (contd.) Hoop Stress in Cylinder at $\phi = 90^\circ$ Reinforced Cylinder Intersection
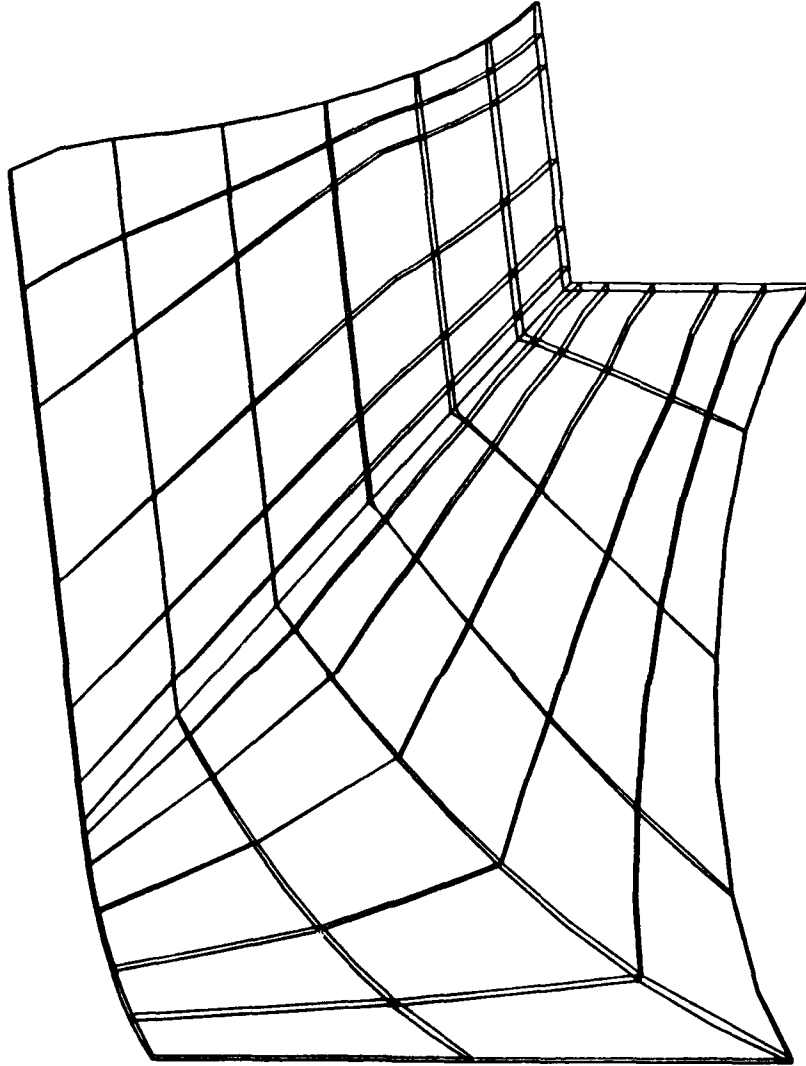
Aspect Ratio = d/D = 1.0

Fig. 6.4.1 Typical Finite Element Discretization of Region SOLID
Aspect Ratio Study
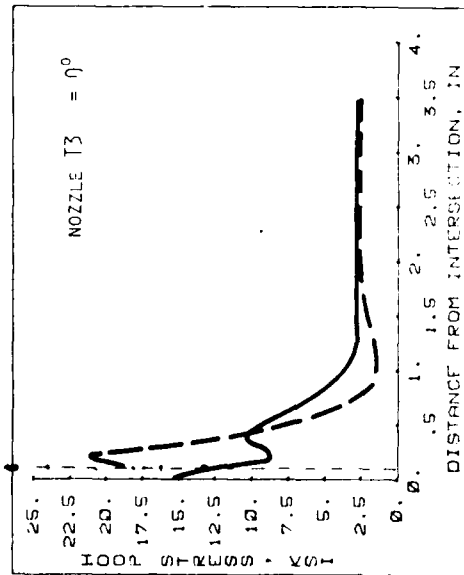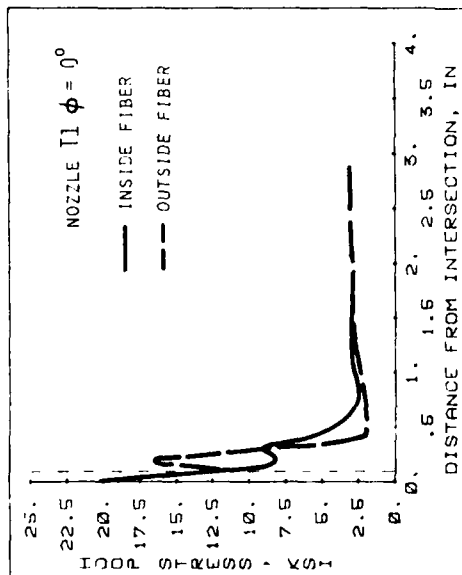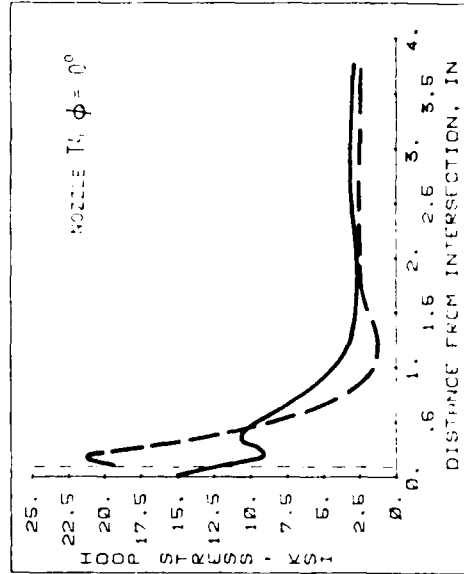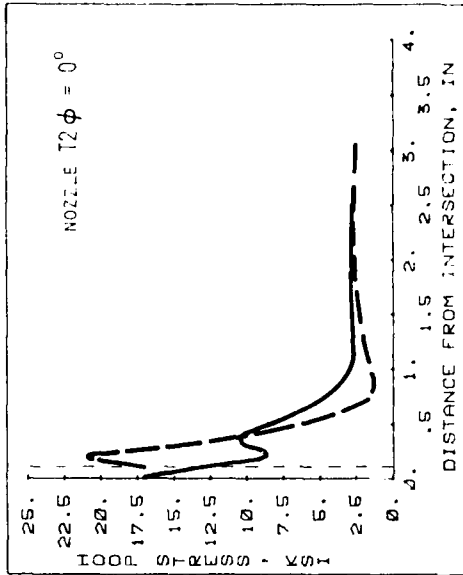
Fig. 6.4.2 Hoop Stress in Nozzle at $\phi = 0^{\circ}$
Aspect Ratio Study
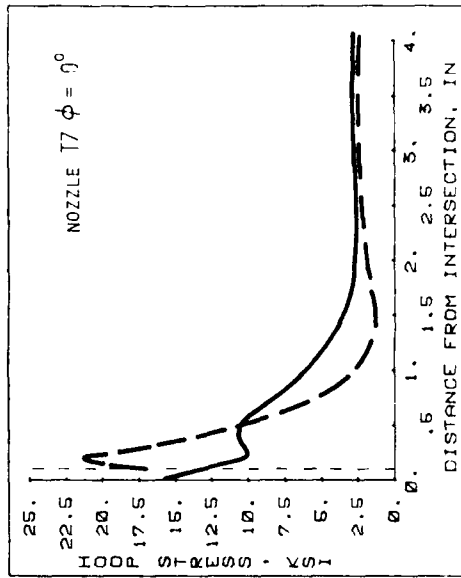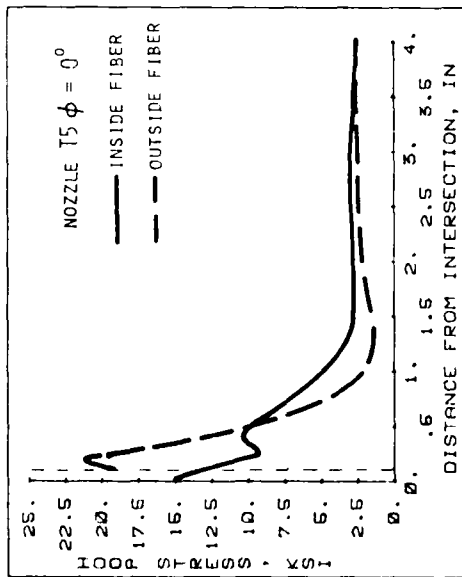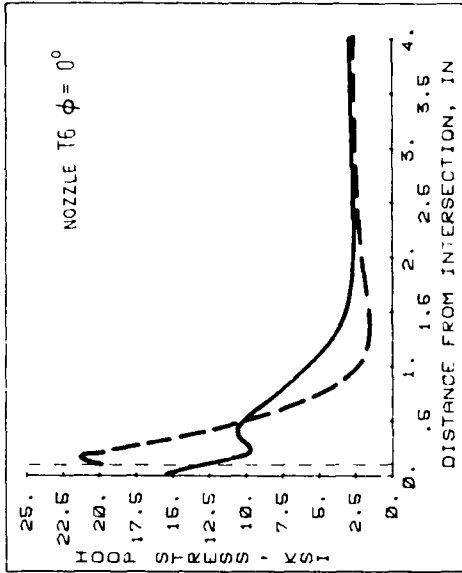
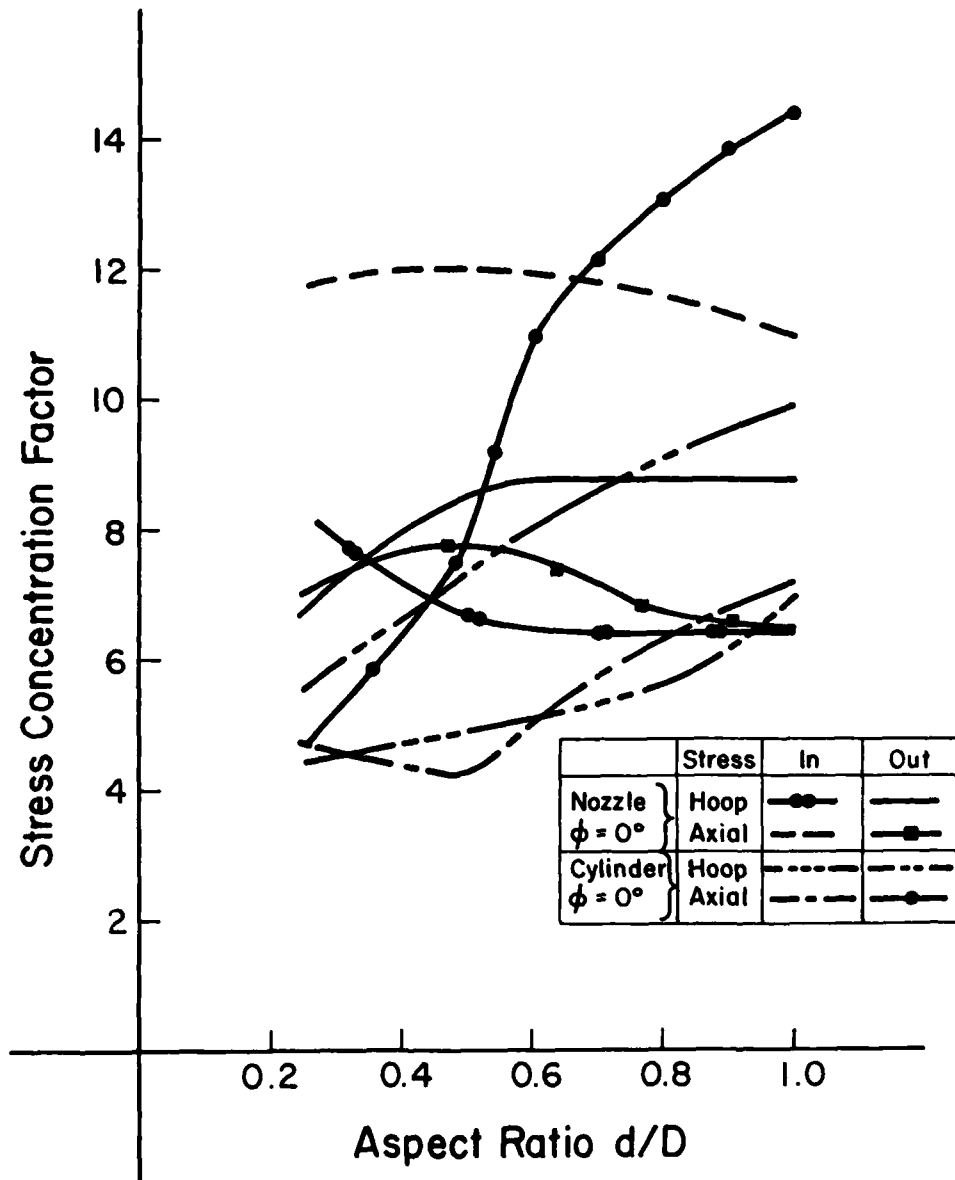Fig. 6.4.2 (contd.) Hoop Stress in Nozzle at $\psi = 0^{\circ}$
Aspect Ratio Study

Fig. 6.4.3 Axial Stress in Nozzle at $\phi = 0^o$
Aspect Ratio Study

1.0

2.8   2.5

3.2

2.2

3.6

4.0   2.0

1.1

1.8

1.25   1.4   1.6

MICROCOPY RESOLUTION TEST CHART
NATIONAL BUREAU OF STANDARDS-1963-A
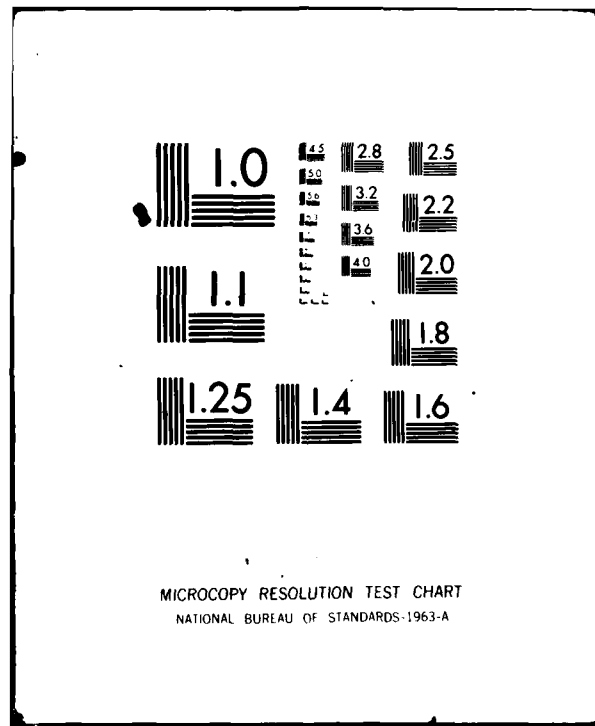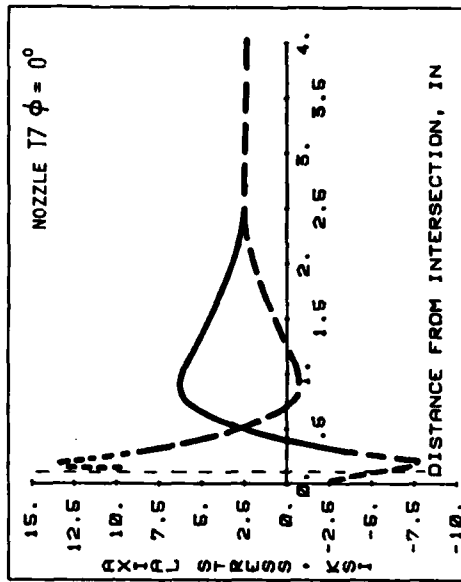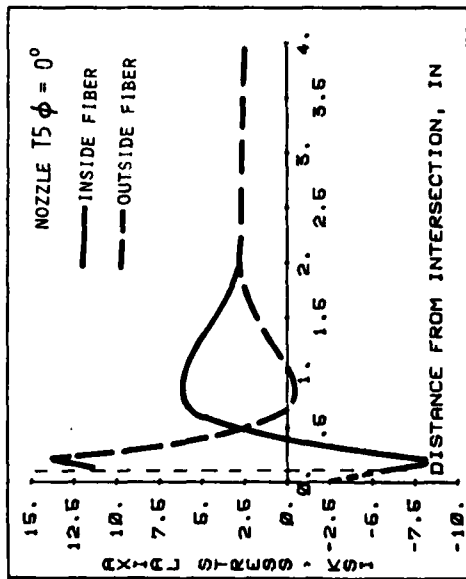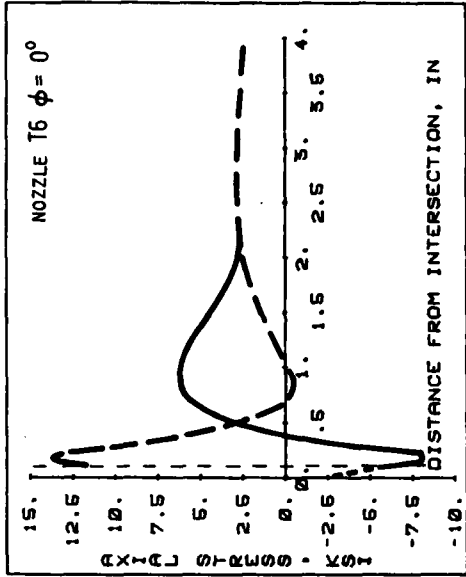
Fig. 6.4.3 (contd.) Axial Stress in Nozzle at $\phi = 0^{\circ}$
Aspect Ratio Study

Fig. 6.4.4 Hoop Stress in Cylinder at $\phi = 0^O$
Aspect Ratio Study

Fig. 6.4.4 (contd.)   Hoop Stress in Cylinder at $\phi = 0°$
Aspect Ratio Study
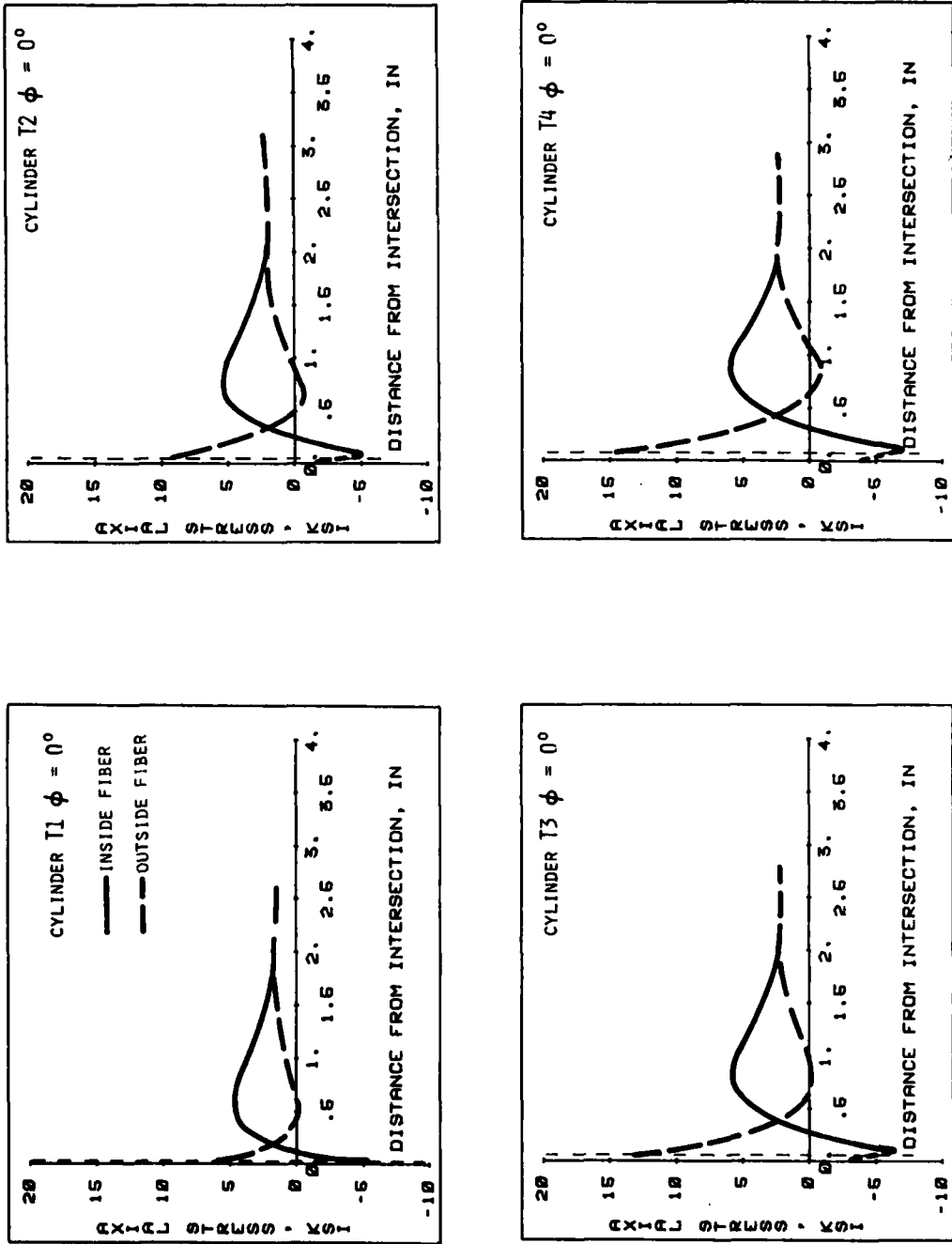
Fig. 6.4.5 Axial Stress in Cylinder at $\phi = 0^o$
Aspect Ratio Study
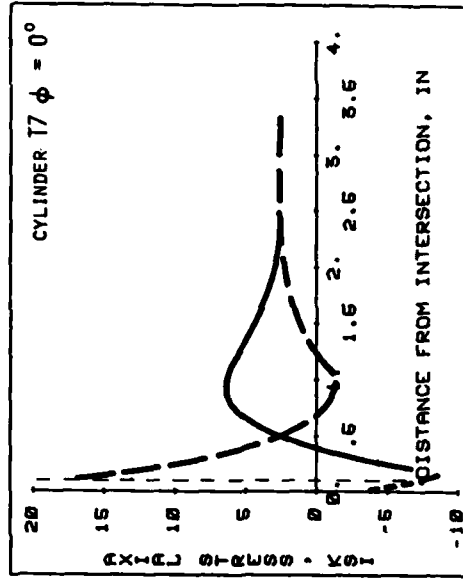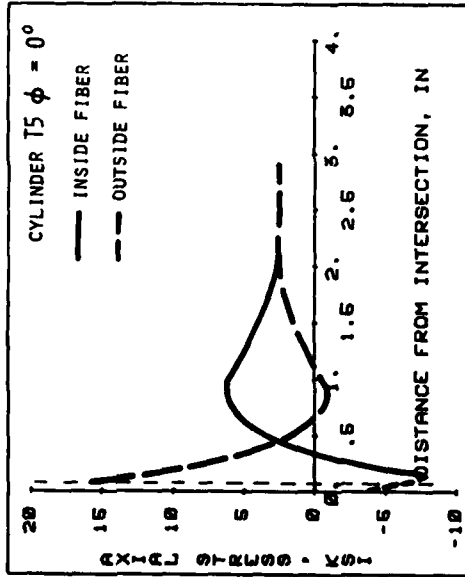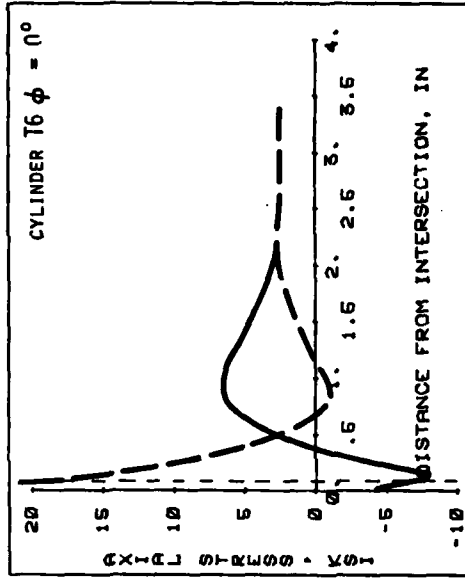
Fig. 6.4.5 (contd.) Axial Stress in Cylinder at $\phi = 0^o$
Aspect Ratio Study
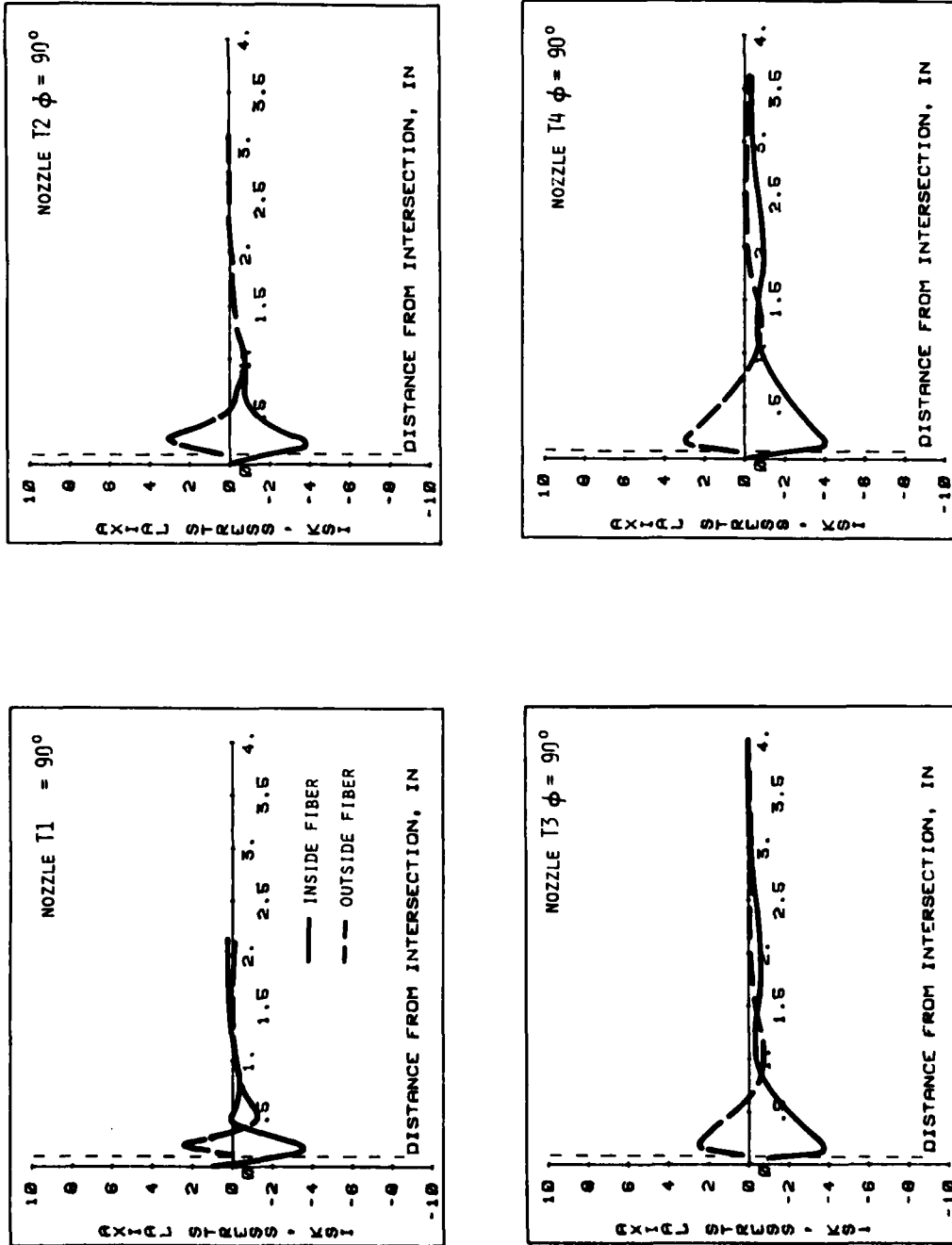
Fig. 6.4.6 Axial Stress in Nozzle at ϕ = 90°
Aspect Ratio Study
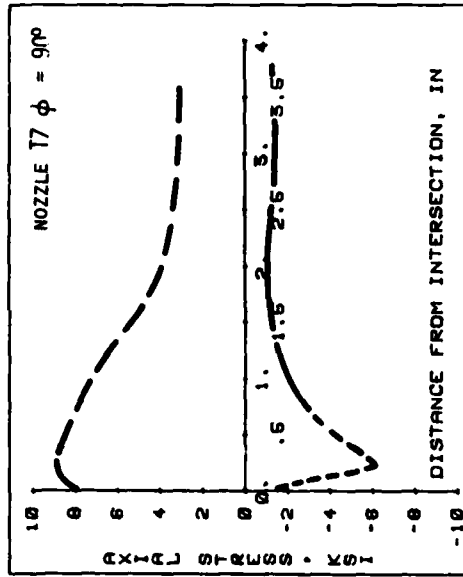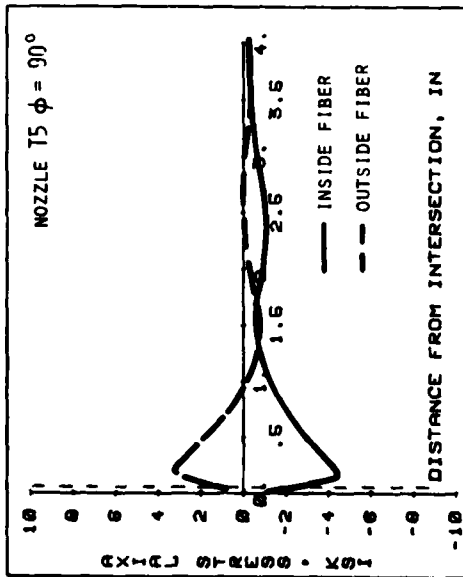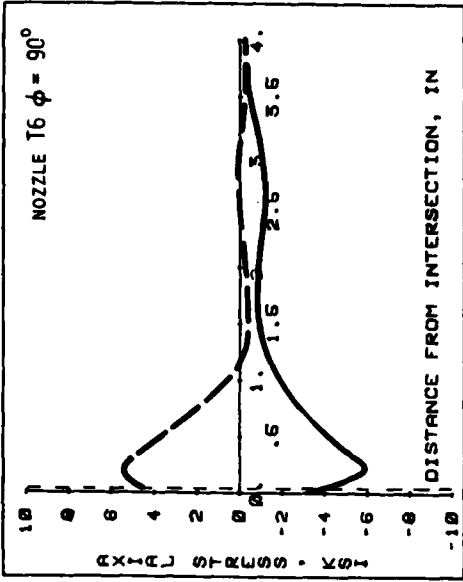
Fig. 6.4.6 (contd.) Axial Stress in Nozzle at φ = 90°
Aspect Ratio Study
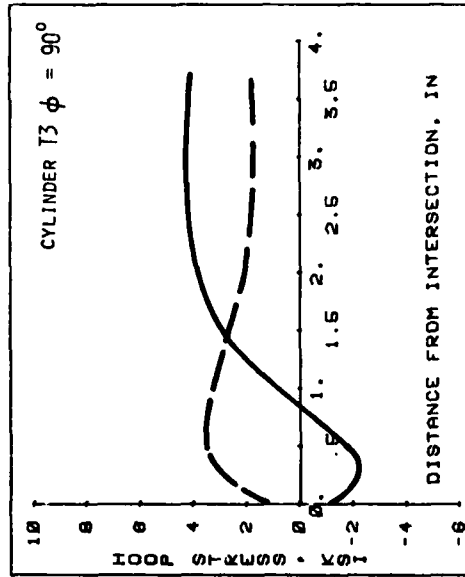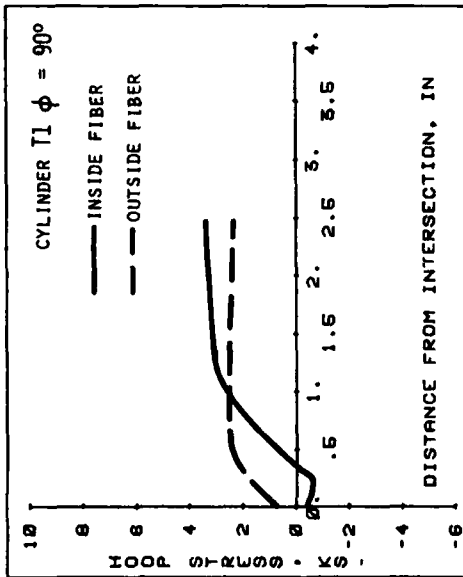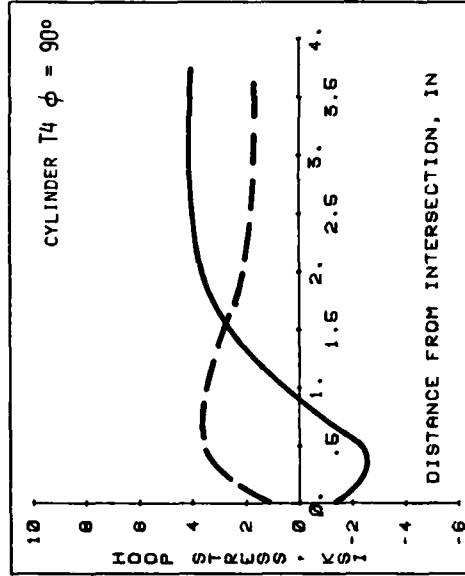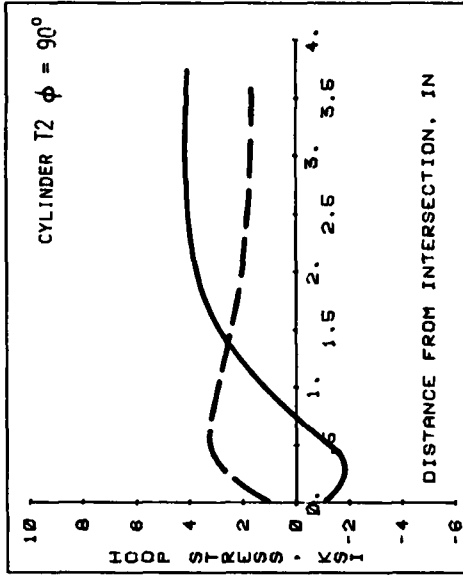
Fig. 6.4.7 Hoop Stress in Cylinder at ϕ = 90°
Aspect Ratio Study

Fig. 6.4.7 (contd.) Hoop Stress in Cylinder at $\phi = 90^\circ$
Aspect Ratio Study

Fig. 6.4.8 Stress Concentration Factors for
Different Aspect Ratios
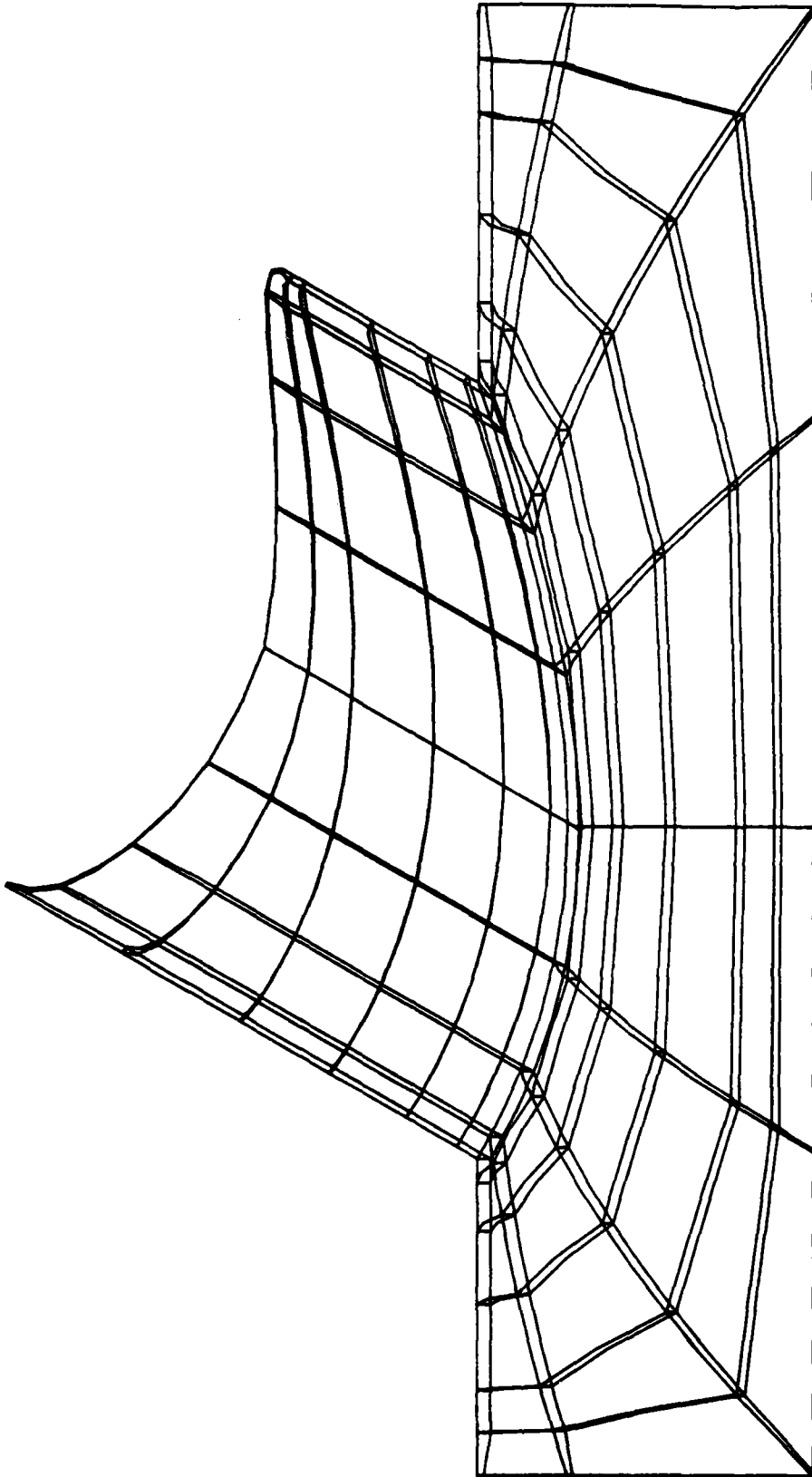
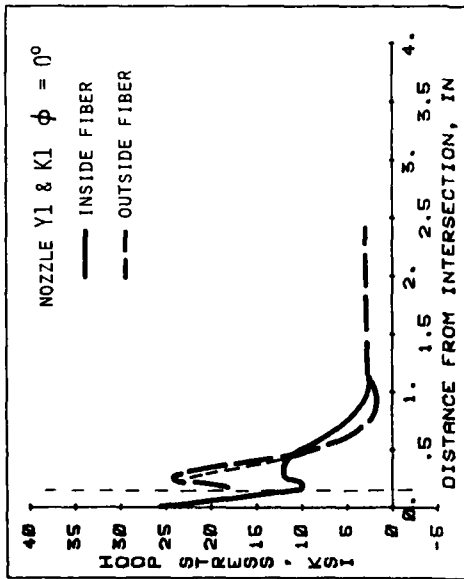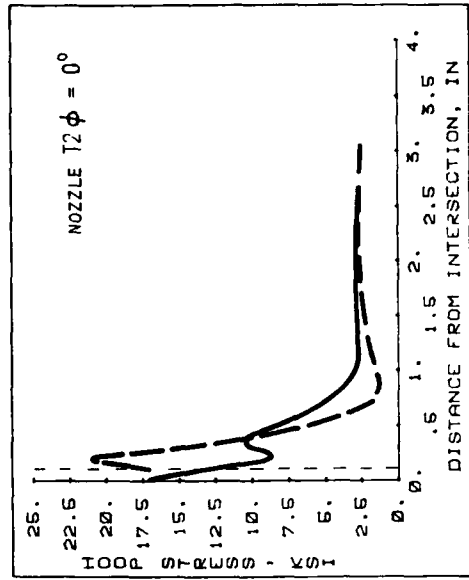Fig. 6.5.1 Typical Finite Element Discretization of Region SOLID
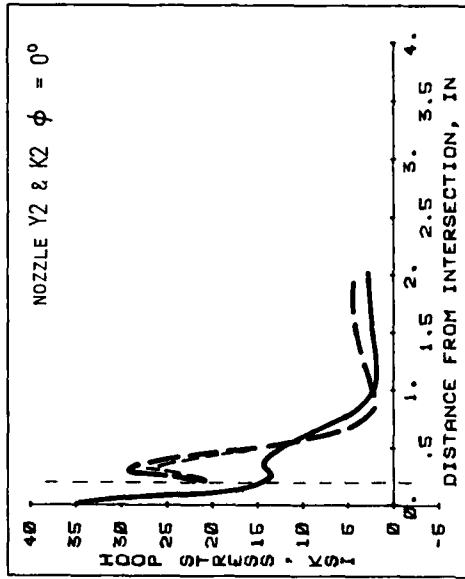Non-Radial Intersection
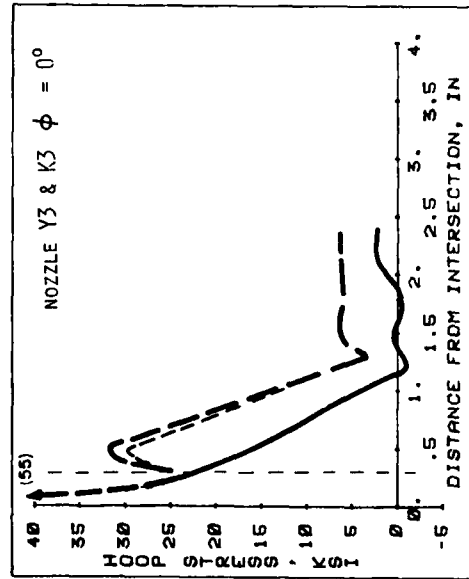
Fig. 6.5.2 Hoop Stress in Nozzle at $\phi = 0^0$
Non-Radial Intersection
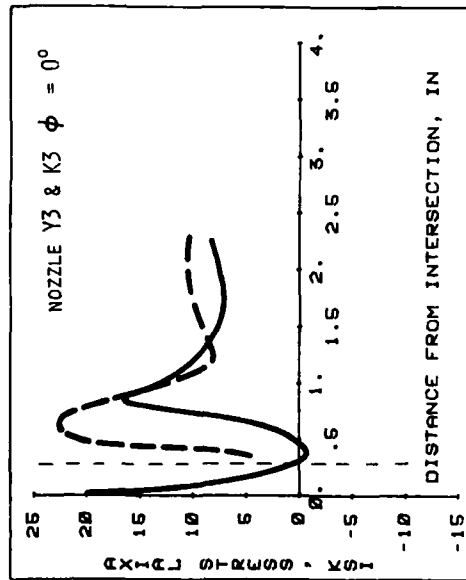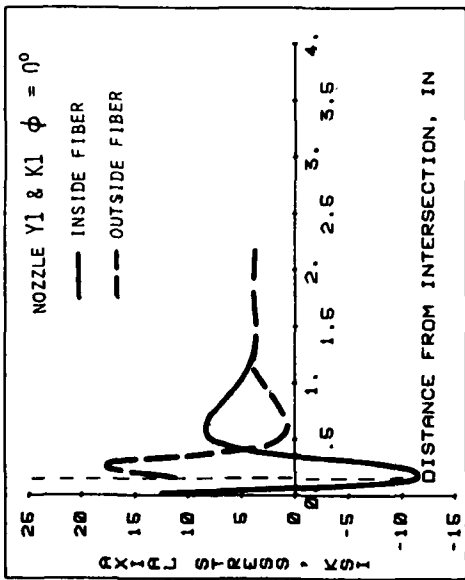
Fig. 6.5.3 Axial Stress in Nozzle at $\phi = 0^o$
Non-Radial Intersection

Fig. 6.5.4 Hoop Stress in Cylinder at $\phi = 0^{\circ}$
Non-Radial Intersection
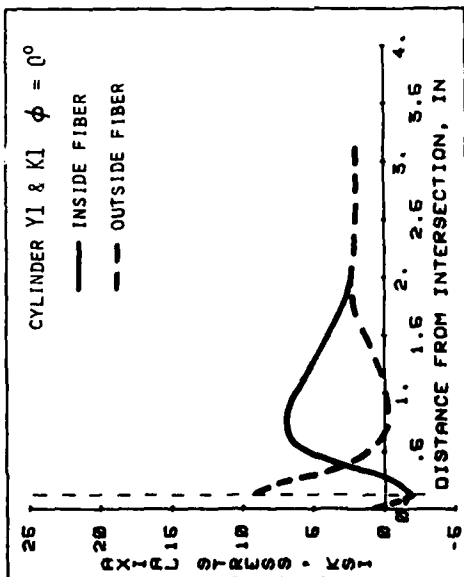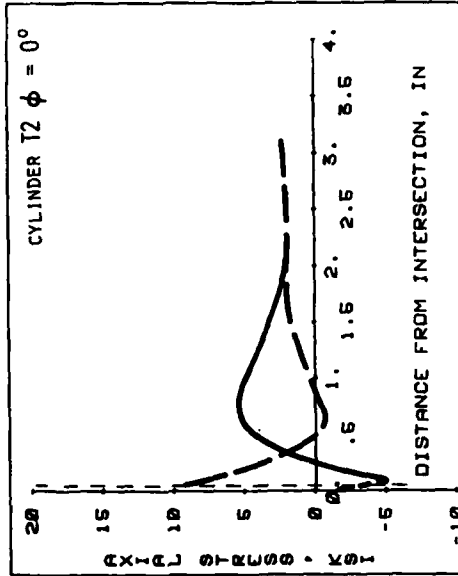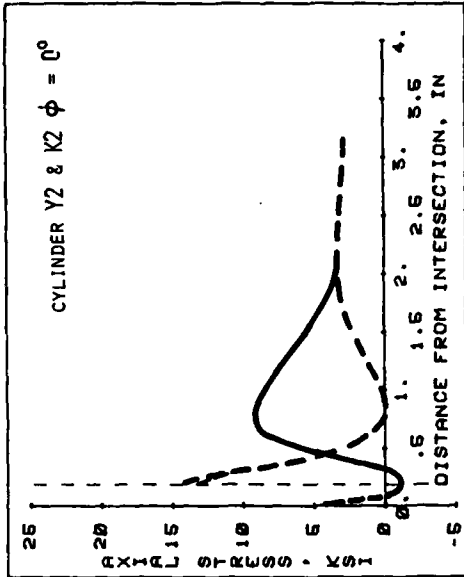
Fig. 6.5.5   Axial Stress in Cylinder at $\phi = 0^o$
Non-Radial Intersection
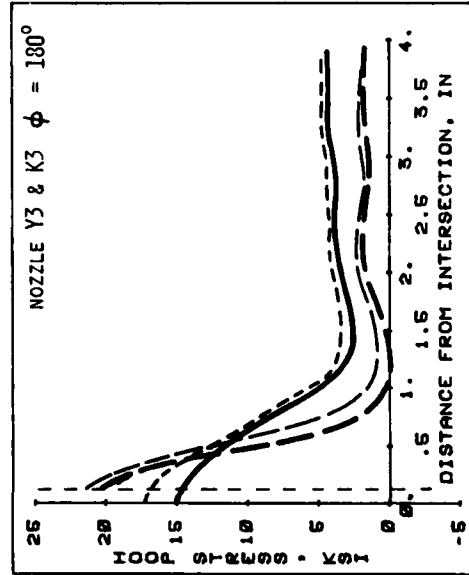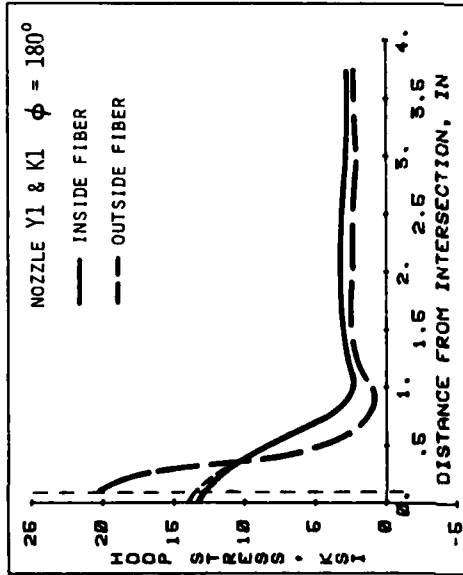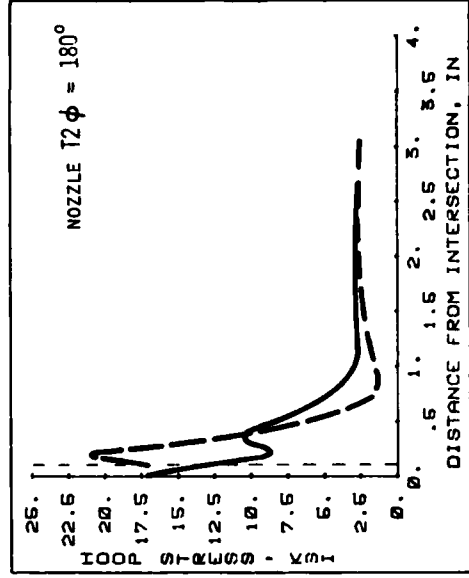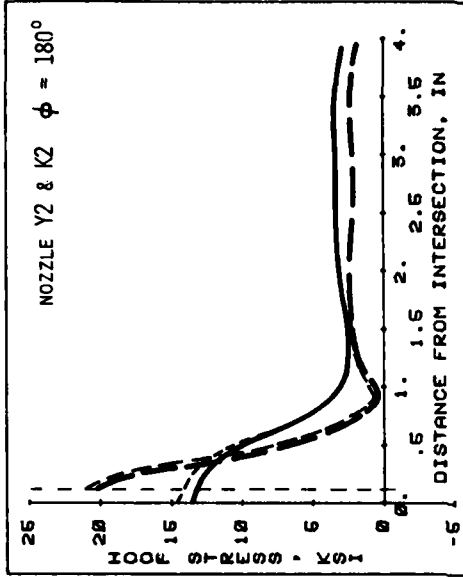
Fig. 6.5.6   Hoop Stress in Nozzle at $\phi = 180^O$
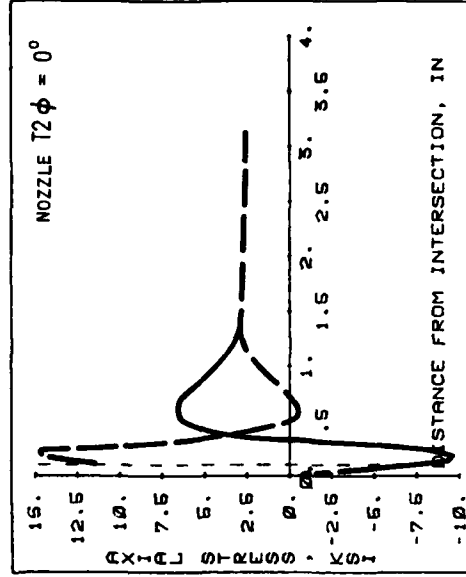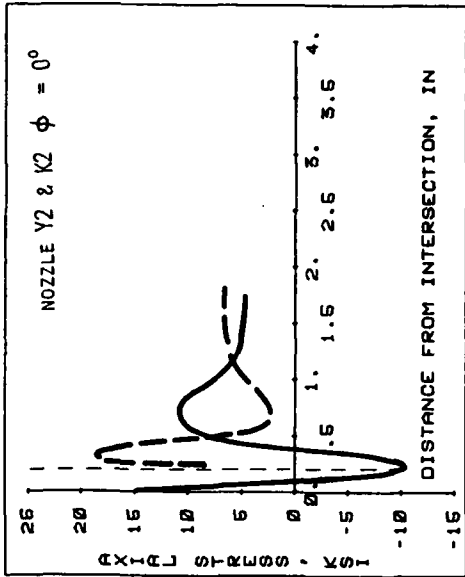Non-Radial Intersection

Fig. 6.5.7   Axial Stress in Nozzle at $\phi = 180^o$
Non-Radial Intersection
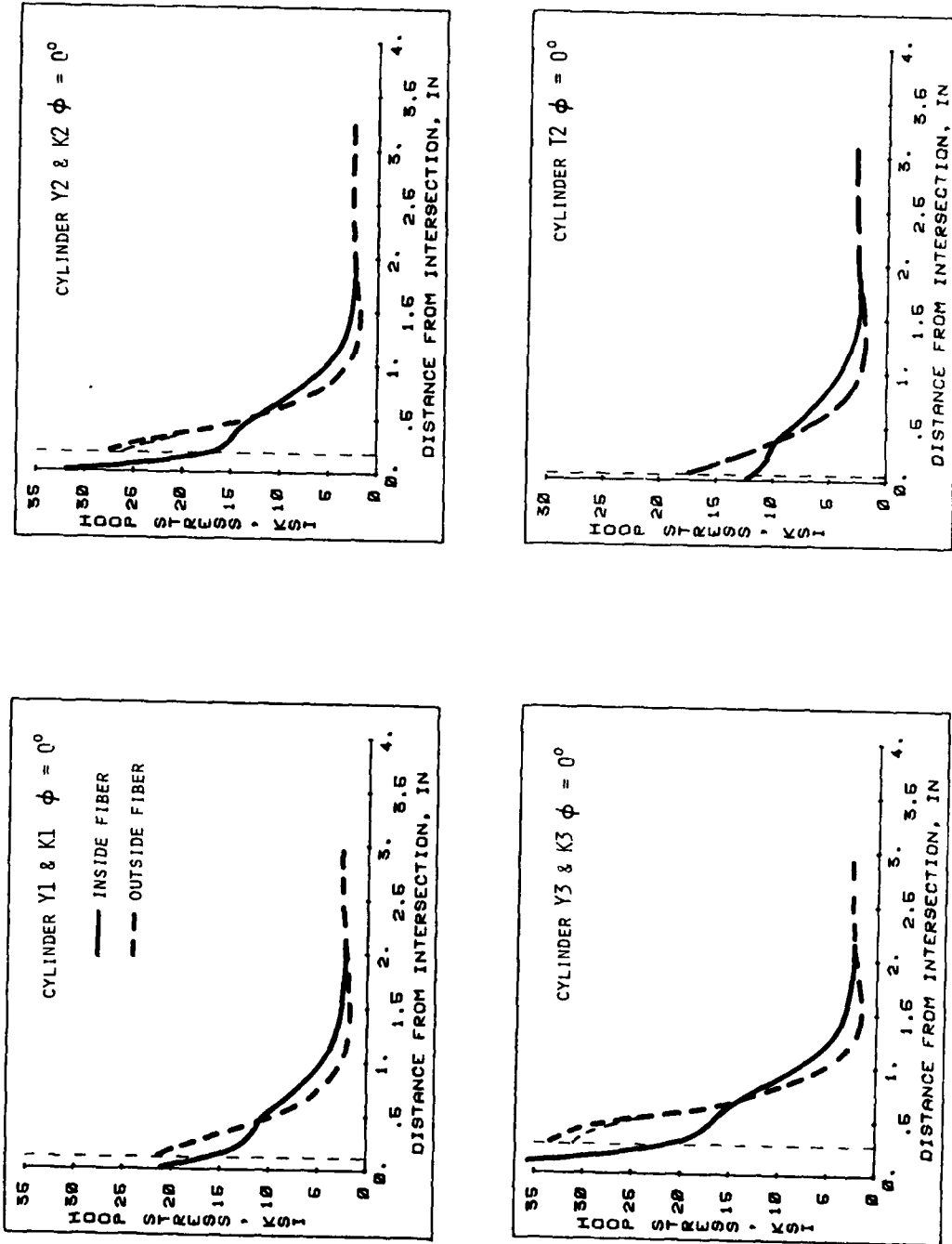
Fig. 6.5.8 Hoop Stress in Cylinder at $\phi = 180^\circ$
Non-Radial Intersection
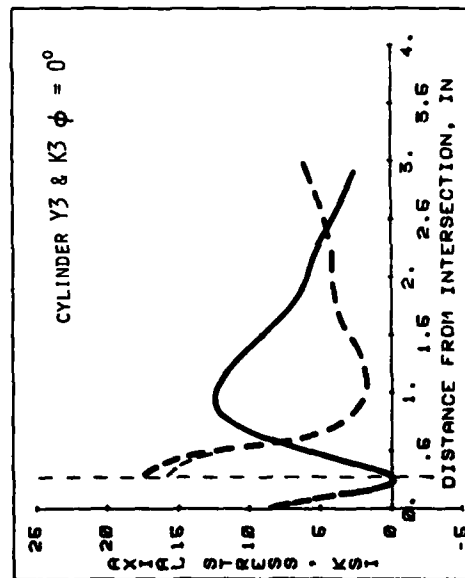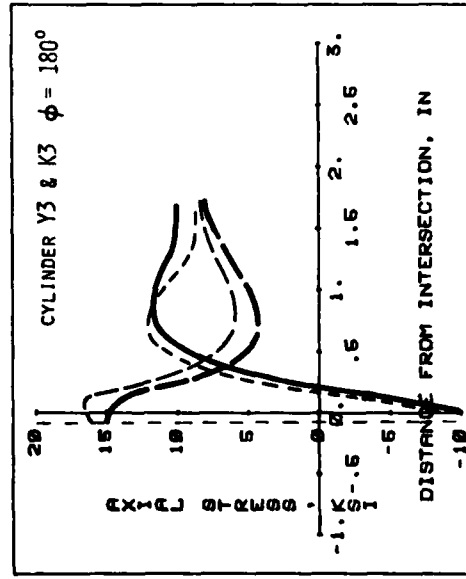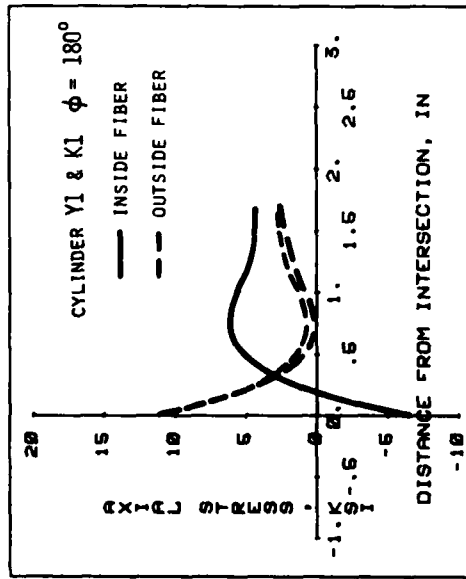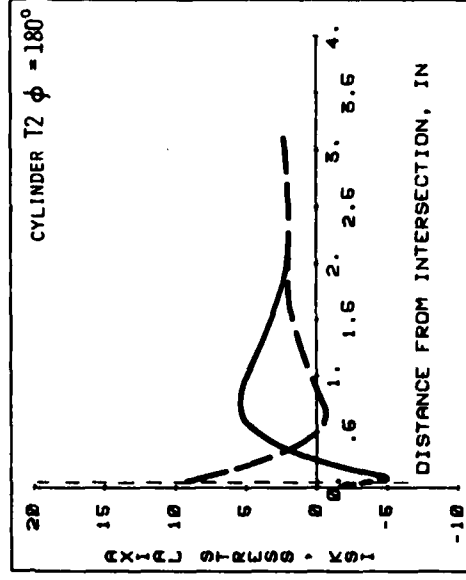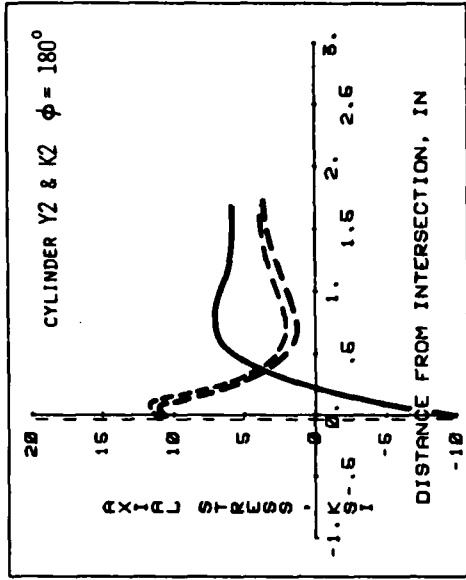
Fig. 6.5.9 Axial Stress in Cylinder at $\phi = 180^O$
Non-Radial Intersection
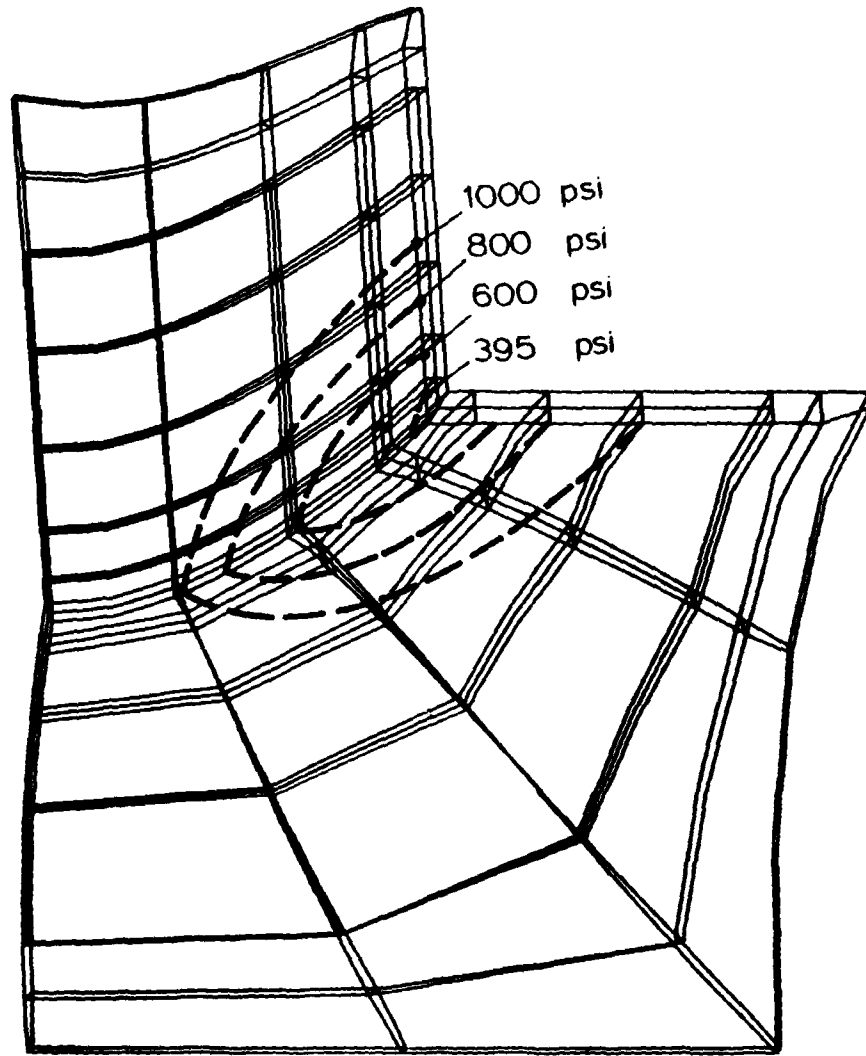
Fig. 6.6.1 Finite Element Model for Region SOLID
of Structure TNL1, with Spread of
Plastic Zone on Inface
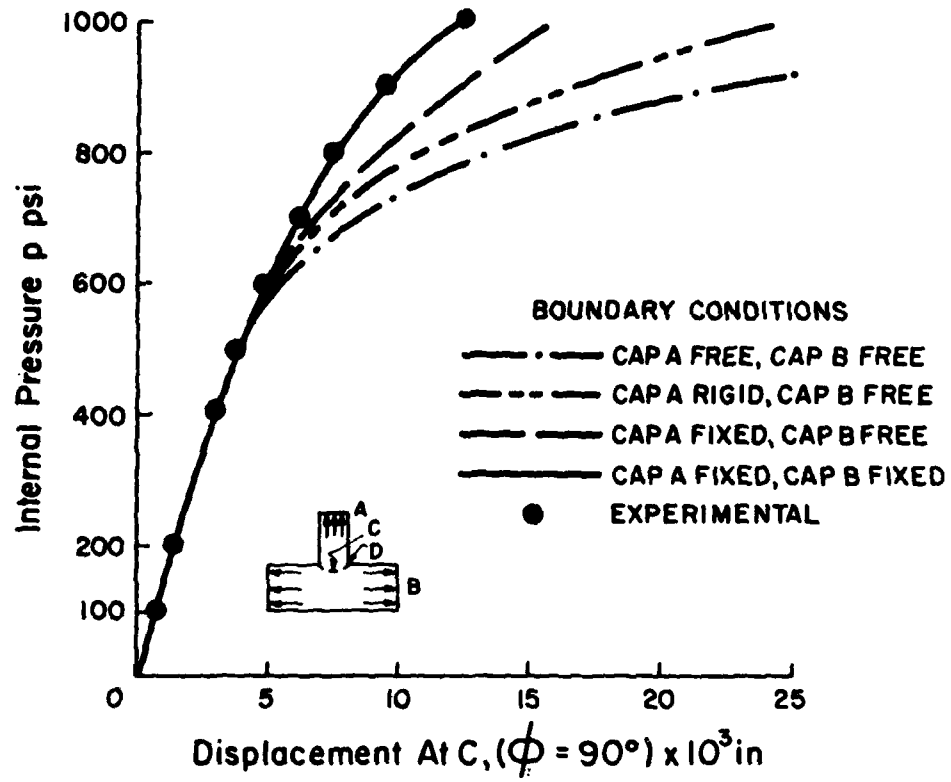
Fig. 6.6.2 Displacements for Various Boundary Conditions of
End Caps for Structure TNL1
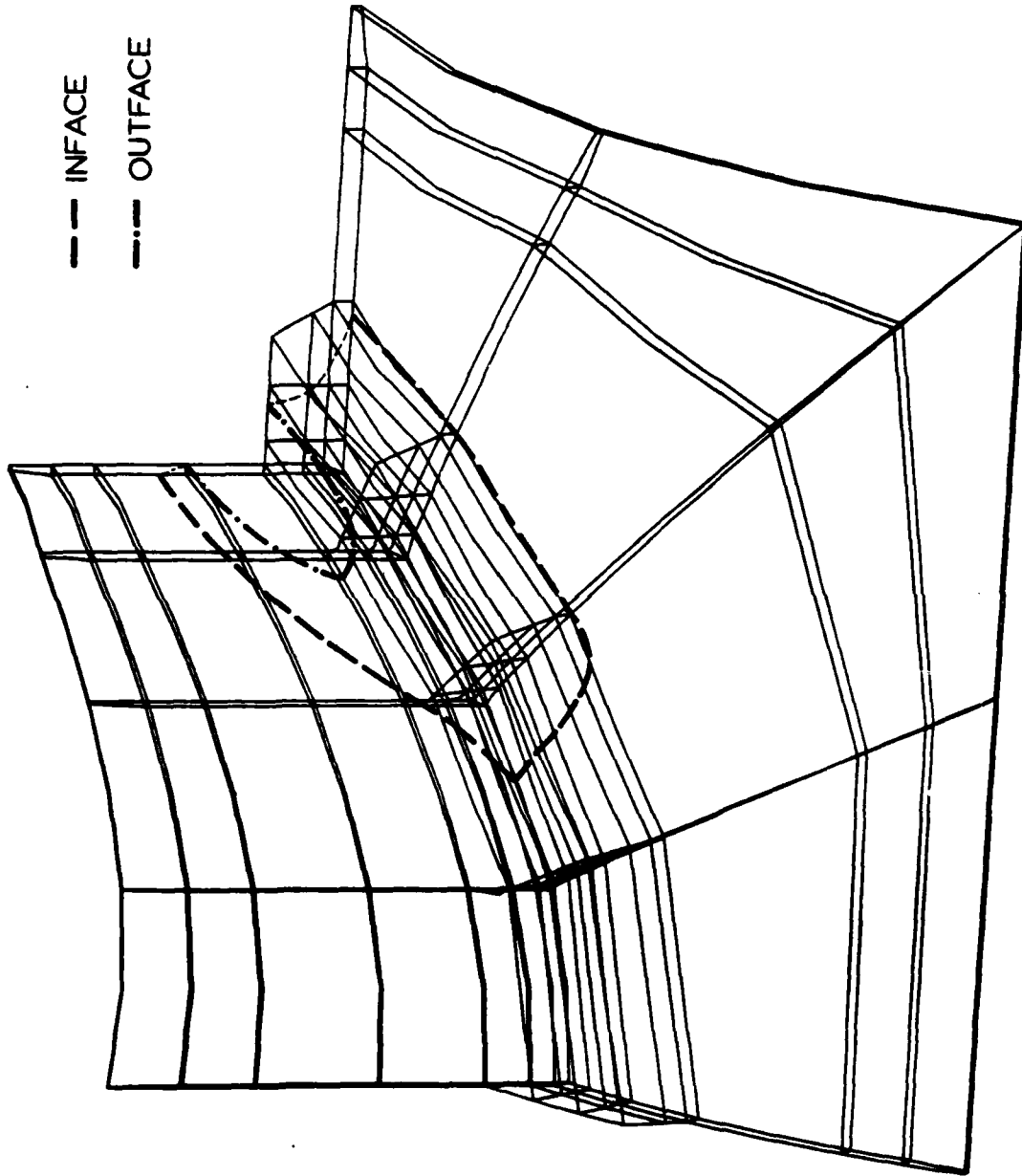
Fig. 6.7.1 Finite Element Model for Region SOLID of Structure TNL2, with Yield Envelope at Internal Pressure of 425 psi

INFACE
OUTFACE
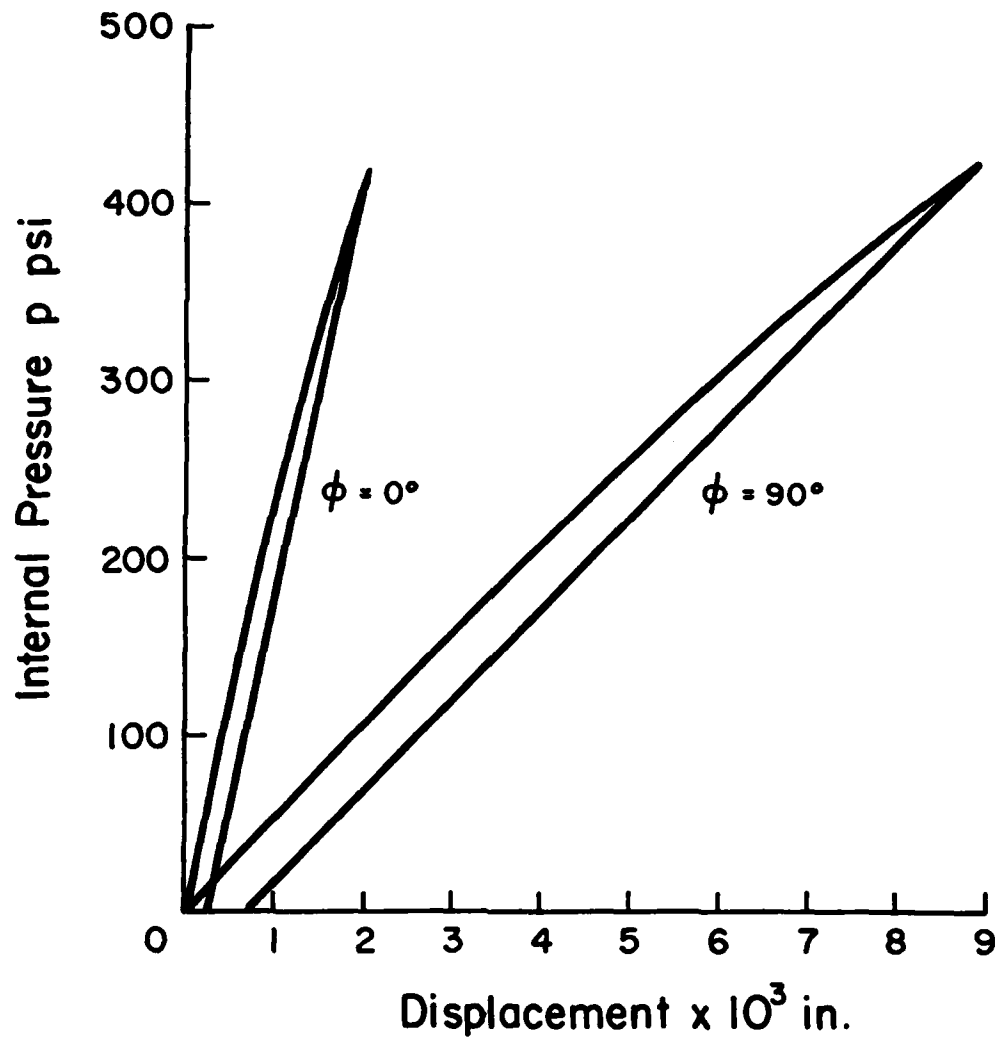
Fig. 6.7.2 Radial Nozzle Displacements of TNL2
at Curve of Intersection
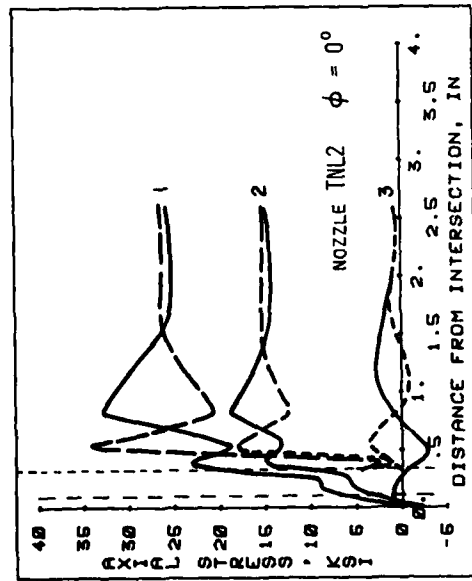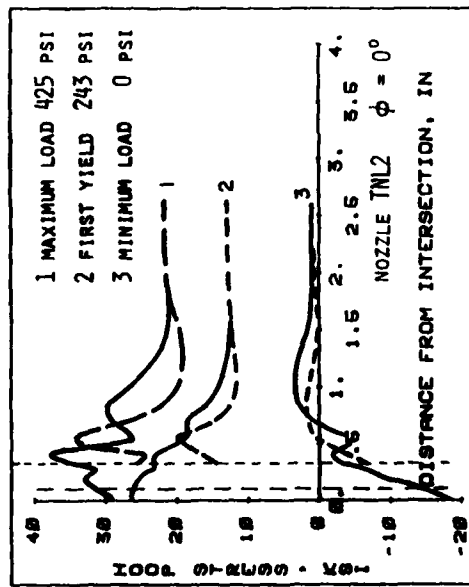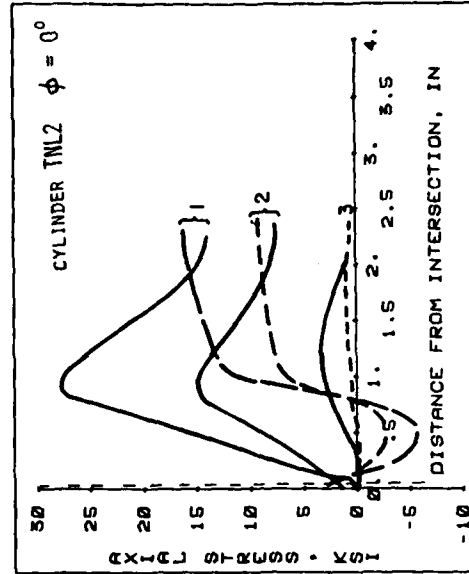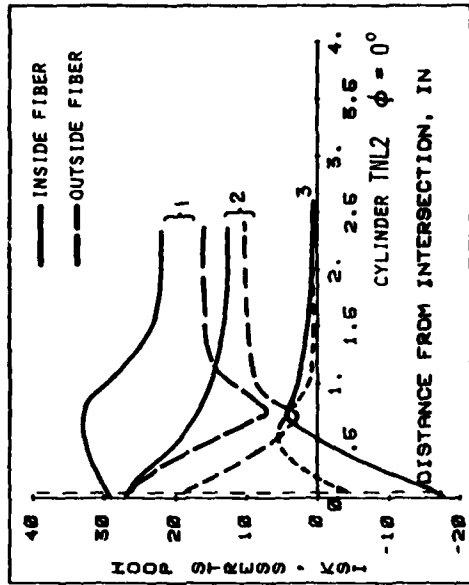
Fig. 6.7.3   Stress Pattern for Nonlinear Analysis of Cylinder
Intersection TNL2
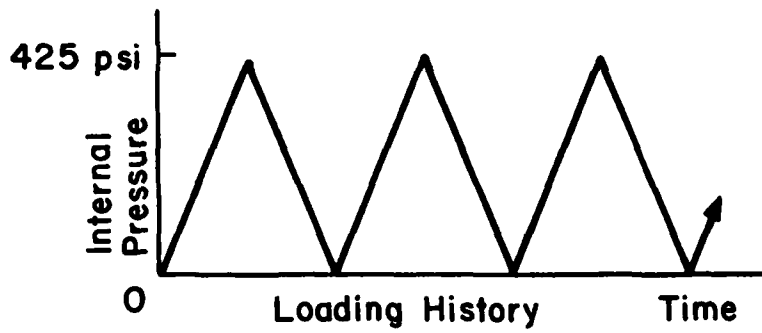
Fig. 6.7.4 Loading History for Structure TNL2

$$\frac{\Delta \epsilon}{2} = 0.9493(2N_f)^{-0.64} + 0.003365(2N_f)^{-0.11}$$

Reversals To Failure, $2N_f$
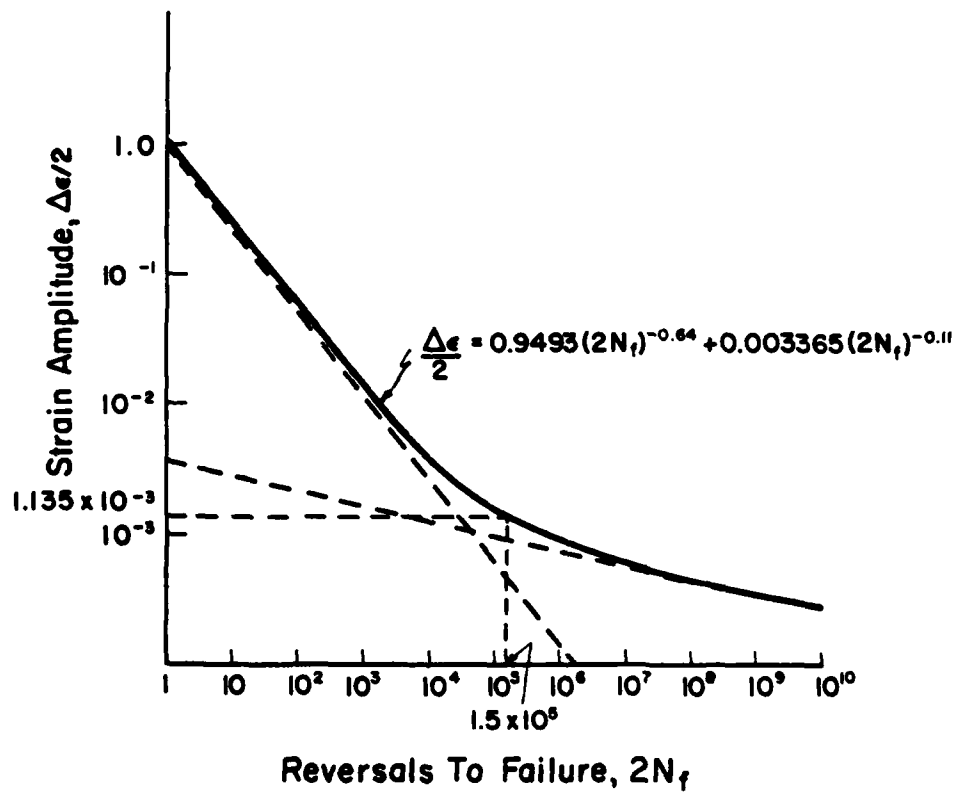
Fig. 6.7.5 Strain Amplitude-Fatigue Life Curve for Structure TNL2

APPENDIX A

INPUT COMMANDS FOR MESH GENERATOR AND DEFAULT VALUES
OF VARIOUS PARAMETERS

Commands and variables to control the configuration of

the mesh (Fig. 3.1) are listed as follows:

1. DEFAULT

2. CYLINDER

    RADIUS <R> THICKNESS <T> LENGTH <L_1 L_2>

    (STRESS CONCENTRATION)FACTORS<CSF0 CSF90 CSF180>

    SOLID (ELEMENT PROPORTION) <CF_1 CF_2 CF_3 CF_4>

    SHELL (ELEMENT PROPORTION) <CF>

3. NOZZLE

    RADIUS <r> THICKNESS <t> LENGTH <ℓ>

    (STRESS CONCENTRATION) FACTORS <NSF_0 NSF_{90} NSF_{180}>

    (ROWS OF) THREE (ELEMENTS) <TDRN>

    SOLID (ELEMENT PROPORTION) <NF_1 NF_2 . . . NF_{TDRN}>

    SHELL (ELEMENT PROPORTION) <NF>

4. ANGLE (OF INTERSECTION) <α>

5. LAYERS (THROUGH THICKNESS) <NL>

6. REINFORCEMENT

    TYPE <RF> LENGTH <RFL> THICKNESS <RFT>

    ELEMENT (CONFIGURATION) <$RFNE_1$ $RFNE_2$>

    ANGLE (OF OFFSET) <$RF\theta$>

7. SUBSTRUCTURE SOLID

8. GENERATE   NOZZLE
                     CYLINDER
                     SOLID   Q3D1SOP
                                 TS161SOP

                     ALL   Q3D1SOP
                                 TS161SOP

9. END

VARIABLE	DEFAULT	REMARK
DEBUG	FALSE	Prints various variables in the process of mesh generation
R		Mid surface radius of the cylinder
T		Thickness of the cylinder
L_1		RHS length of the cylinder
L_2		LHS length of the cylinder
CSF_0	1.1	Multiplying factor to $2.45\sqrt{R \cdot T}$ @ $\phi = 0$ *
CSF_{90}	1.5	Multiplying factor to $2.45\sqrt{R \cdot T}$ @ $\phi = 90^O$*
CSF_{180}	1.1	Multiplying factor to $2.45\sqrt{R \cdot T}$ @ $\phi = 180^O$*
CF_1	0.2	Length proportionality factor for row 1#
CF_2	0.4	" " " " " 2#
CF_3	0.6	" " " " " 3#
CF_4	0.7	" " " " " 4#
CF	1.0	Ratio of length to width for this shell elements for CYLSHELL
r		Midsurface radius of the nozzle
t		Thickness of the nozzle
ℓ		Length of the nozzle
NSF_0	1.2	Multiplying factor to $2.45\sqrt{r \cdot t}$ @ $\phi = 0^O$ *
NSF_{90}	1.7	Multiplying factor to $2.45\sqrt{r \cdot t}$ @ $\phi = 90^O$ *
NSF_{180}	1.2	" " " " " @ $\phi = 180^O$*
TDRN	4	Number of rows of three dimensional elements in nozzle
NF_i		Length proportionality of various rows of TDRN #
NF	1.0	Ratio of length to width for the shell element for NOZSHELL

*To get region of stress concentration for SOLID

#Number of rows counted from the curve of intersection.

VARIABLES	DEFAULT	REMARK
α	90°	Angle of Intersection of Nozzle and Cylinder
NL	1	Layers of three dimensional elements, through thickness, for SOLID
RF		Type of reinforcement TYPES = 1 or 2 or 3
RFL		Length of the reinforcement
RFT		Thickness of the reinforcement
$RFNE_1$		Number of rows of elements through length
$RFNE_2$	1	Layers of elements through thickness
$RF\theta$		Angle of offset at the end of the reinforcement
SUBSTRUCT	.FALSE.	Substructures in $0 \le \phi \le 90^{\circ}$ $90^{\circ} \le \phi \le 180^{\circ}$

APPENDIX B

TRANSFORMATION OF SHELL TO THREE DIMENSIONAL DEGREE OF FREEDOM

Displacement fields for the Ahmad's shell elements are assumed to be linear through thickness, along the outward normal vector. Considering the thickness of the element at node point m, the displacements of top surface point 't' and bottom surface point 'b', Fig. 3.2 , can be written in the form

$$
\begin{Bmatrix} u_t \\ v_t \\ w_t \end{Bmatrix} = \begin{Bmatrix} u_m \\ v_m \\ w_m \end{Bmatrix} + \frac{h}{2} \begin{bmatrix} a - b \end{bmatrix} \begin{Bmatrix} \alpha \\ \beta \end{Bmatrix}
\tag{B.1}
$$

and

$$
\begin{Bmatrix} u_b \\ v_b \\ w_b \end{Bmatrix} = \begin{Bmatrix} u_m \\ v_m \\ w_m \end{Bmatrix} - \frac{h}{2} \begin{bmatrix} a - b \end{bmatrix} \begin{Bmatrix} \alpha \\ \beta \end{Bmatrix}
\tag{B.2}
$$

Adding (B.1) and (B.2)

$$
\begin{Bmatrix} u_m \\ v_m \\ w_m \end{Bmatrix} = \begin{bmatrix} \frac{1}{2} & 0 & 0 & \frac{1}{2} & 0 & 0 \\ 0 & \frac{1}{2} & 0 & 0 & \frac{1}{2} & 0 \\ 0 & 0 & \frac{1}{2} & 0 & 0 & \frac{1}{2} \end{bmatrix} \begin{Bmatrix} u_t \\ v_t \\ w_t \\ u_b \\ v_b \\ w_b \end{Bmatrix}
\tag{B.3}
$$

subtracting (B.2) from (B.1)

$$
h\,[a-b]\begin{Bmatrix}\alpha\\\beta\end{Bmatrix} = \begin{bmatrix} 1 & 0 & 0 & -1 & 0 & 0 \\ 0 & 1 & 0 & 0 & -1 & 0 \\ 0 & 0 & 1 & 0 & 0 & -1 \end{bmatrix} \begin{Bmatrix} u_t \\ v_t \\ w_t \\ u_b \\ v_b \\ w_b \end{Bmatrix} \tag{B.4}
$$

i.e.

$$
\begin{Bmatrix}\alpha\\\beta\end{Bmatrix} = \frac{1}{h}\begin{Bmatrix} a \\ -b \end{Bmatrix} \begin{bmatrix} 1 & 0 & 0 & -1 & 0 & 0 \\ 1 & 0 & 0 & -1 & 0 & 0 \\ 0 & 0 & 1 & 0 & 0 & -1 \end{bmatrix} \begin{Bmatrix} u_t \\ v_t \\ w_t \\ u_b \\ v_b \\ w_b \end{Bmatrix} \tag{B.5}
$$

In local coordinate system rotation components are

$$
\begin{Bmatrix} \theta_{xm} \\ \theta_{ym} \\ \theta_{zm} \end{Bmatrix} = [b \quad a]\begin{Bmatrix}\alpha\\\beta\end{Bmatrix} \tag{B.6}
$$

substituting (B.5) in (B.6)

$$
\begin{Bmatrix} \theta_{xm} \\ \theta_{ym} \\ \theta_{zm} \end{Bmatrix} = \frac{1}{h}[b \quad a]\begin{Bmatrix} a \\ -b \end{Bmatrix} \begin{bmatrix} 1 & 0 & 0 & -1 & 0 & 0 \\ 0 & 1 & 0 & 0 & -1 & 0 \\ 0 & 0 & 1 & 0 & 0 & -1 \end{bmatrix} \begin{Bmatrix} u_t \\ v_t \\ w_t \\ u_b \\ v_b \\ w_b \end{Bmatrix} \tag{B.7}
$$

from (B.3) and (B.7)

$$
\begin{Bmatrix} u_m \\ v_m \\ w_m \\ \theta_{xm} \\ \theta_{ym} \\ \theta_{zm} \end{Bmatrix} = \begin{bmatrix} \frac{1}{2} & 0 & 0 & \frac{1}{2} & 0 & 0 \\ 0 & \frac{1}{2} & 0 & 0 & \frac{1}{2} & 0 \\ 0 & 0 & \frac{1}{2} & 0 & 0 & \frac{1}{2} \\ 0 & -A & -B & 0 & A & B \\ A & 0 & -C & -A & 0 & C \\ B & C & 0 & -B & -C & 0 \end{bmatrix} \begin{Bmatrix} u_t \\ v_t \\ w_t \\ u_b \\ v_b \\ w_b \end{Bmatrix}
\qquad (B.8)
$$

or

$$
\{u_{sh}\} = [T] \{u_{3D}\}
\qquad (B.9)
$$

where,

$$
A = \frac{1}{h} (a_1 b_2 - a_2 b_1)
$$

$$
B = \frac{1}{h} (a_1 b_3 - a_3 b_1)
$$

$$
C = \frac{1}{h} (a_2 b_3 - a_3 b_2)
$$

APPENDIX C

DERIVATION FOR PERMANENT ANISOTROPY

The behavior of a material with permanent anisotropy for plane stress case is simulated by changing the shape function. It is assumed that material is homogeneous displaying same yield stresses in all the direction. Hence in the σ_1, σ_2 stress plane the yield surface can be represented by circular arcs in the tensile quadrant and the compressive quadrant connected by smooth transition curves as shown in Fig. 5.8. In Haigh-Westergaard stress space this transition curve is represented by a frustra of a cone. Assuming linear transition along the σ_m axis, the radius of this hypersurface is

$$\sigma_r = m \, \bar{\sigma}_m + C \tag{C.1}$$

For uniaxial tensile yield $\sigma_r = \sqrt{2/3} \; \sigma_Y^T$ at $\bar{\sigma}_m = \frac{1}{3} \sigma_Y^T$, hence from (C.1):

$$\sqrt{2/3} \; \sigma_Y^T = \frac{1}{3} \sigma_Y^T \, m \; + C \tag{C.2}$$

For uniaxial compressive yield $\sigma_r = \sqrt{2/3} \; \sigma_Y^C$ at $\bar{\sigma}_m = -\frac{1}{3} \sigma_Y^C$ substituting this condition in (C.1):

$$\sqrt{2/3} \; \sigma_Y^C = -\frac{1}{3} \sigma_Y^C \, m + C \tag{C.3}$$

Solving simultaneous equations presented by Eqs. C.2 and C.3 yields:

$$\sigma_r = \sqrt{3/2} \; \{ \frac{3(\sigma_Y^T - \sigma_Y^C)}{(\sigma_Y^T + \sigma_Y^C)} \quad \sigma_m + \frac{2 \; \sigma_Y^T \; \sigma_Y^C}{(\sigma_Y^T + \sigma_Y^C)} \} \tag{C.4}$$

Recognizing

$$\sigma_r = \sqrt{2/3}\ \sigma_Y^{tr} \tag{C.5}$$

$$\sigma_Y^{tr} = \frac{3(\sigma_Y^T - \sigma_Y^C)}{(\sigma_Y^T + \sigma_Y^C)}\ \bar{\sigma}_m + \frac{2\ \sigma_Y^T\ \sigma_Y^C}{(\sigma_Y^T + \sigma_Y^C)}\ \ \text{for}\ -\frac{1}{3}\ \sigma_Y^C < \sigma_m < \frac{1}{3}\ \sigma_Y^T \tag{C.6}$$

Similarly, the elastic modulus can have different values E^T and E^C in tensile quadrant and in compressive quadrant respectively with an assumption of linear transition in connecting region. Hence,

$$E^{tr} = m \cdot \bar{\sigma}_m + C \tag{C.7}$$

Substituting conditions, $E^{tr} = E^T$ for $\sigma_m = \frac{1}{3}\ \sigma_Y^T$ and

$E^{tr} = E^C$ for $\sigma_m = -\frac{1}{3}\ \sigma_Y^C$ in Eq. (C.7) yields simultaneous equations as:

$$E^T = \frac{1}{3}\ \sigma_Y^T \cdot m + C \tag{C.8}$$

and

$$E^C = -\frac{1}{3}\ \sigma_Y^C\ m + C \tag{C.9}$$

solving Eqs. (C.8) and (C.9) yields:

$$E^{tr} = \frac{3(E^T - E^C)}{(\sigma_Y^T + \sigma_Y^C)} + \frac{E^T \sigma_Y^C + \sigma_Y^T\ E^C}{(\sigma_Y^T + \sigma_Y^C)} \tag{C.10}$$

APPENDIX D

NOMENCLATURE

A summary of frequently used symbols is presented below for convenience. Symbols with dual meanings are listed twice.

a	normal to the hyper-surface at a stress point
B	matrix relates Green's strains at a point to finite element nodal displacements
b	fatigue strength exponent
c	fatigue ductility exponent
$C_{ijk\ell}$	matrix relating infinitesimal stress to infinitesimal plastic strain
D	cylinder diameter
D, D_{ij}	constitutive matrix
D_T	current constitutive matrix
D_i	fatigue damage factor
d	nozzle diameter
E	Young's modulus of elasticity
E^T	Young's modulus of elasticity in tensile response
E^C	Young's modulus of elasticity in compressive response
E^{tr}	Young's modulus of elasticity in transitional response
E_i	Young's modulus of elasticity for ith segment of linearly idealized stress-strain curve.
F	Body force
F	Load potential function
f	Stress potential function
G	Shear modulus
G	Scalar constant of proportionality

h	Thickness of an Ahmad shell element
H'	Tangent modulus of stress-plastic strain curve
IF	Internal force matrix
I_1	First invariant of strain
J_2	Second invariant of stress
K	Stiffness matrix
K_T	Tangential stiffness matrix
N_f	Load reversals to fatique failure
N_i	Fatigue life for certain load amplitude i
n_i	Load cycles for certain load amplitude i
N	Shape function matrix
p	Internal pressure
P	Equivalent nodal load
r	Nozzle radius
R	Cylinder radius
S	Body surface
S_{ij}	Deviatoric stress
S_N	Nominal peak stress
t	Nozzle thickness
T	Cylinder thickness
T	Temperature
u	Nodal displacement
u_i, v_i, w_i	Displacement of point, i, in an element
U	Strain energy
V	Body volume
X, Y, Z	Cartesian co-ordinates
x', y', z'	Element local co-ordinate system

α, β Local rotational degree of freedom for an Ahmed shell element

α Angle of intersection of two cylindrical shells

α_{ij} Instantaneous center of rotation of hyper-surfaces

$\delta(\ )$ Increment in a quantity

$\Delta(\ )$ Total change in a quantity

ϵ, ϵ_{ij} Green's strain

$\epsilon_p, \epsilon_{ij}^P$ Plastic component of strain

$\epsilon_e, \epsilon_{ij}^e$ Elastic component of strain

$\epsilon_1, \epsilon_2, \epsilon_3$ Principal strain

$\bar{\epsilon}_e$ Equivalent strain

ϵ_m Mean strain

ϵ'_f True fracture ductility

ϕ Sweeping angle on a plane normal to axis of rotation of nozzle

λ Lame's constant

ν Poisson's ratio

ρ Dimensionless parameter $= \frac{d}{D}\sqrt{D/T}$

σ, σ_{ij} 2nd Piola-Kirchoff stress

$\sigma_1, \sigma_2, \sigma_3$ Principal stresses

σ_o^i Yield stress of hyper-surface i

$\bar{\sigma}_e$ Equivalent stress

σ_m Mean stress

σ'_f True fracture strength

σ_a Axial stress

σ_o Hoop stress

σ_r Radial stress

DISTRIBUTION LIST

for

UNCLASSIFIED TECHNICAL REPORTS

The ONR Structural Mechanics Contract Research Program

This list consists of:

Part 1 - Government Activities
Part 2 - Contractors and Other
         Technical Collaborators

Notes:

Except as otherwise indicated, forward one
copy of all Unclassified Technical Reports
to each of the addressees listed herein.

Where more than one attention addressee is
indicated, the individual copies of the
report should be mailed separately.

Part 1 - Government
Administrative and Liaison Activities

Office of Naval Research
Department of the Navy
Arlington, Virginia 22217
Attn: Code 474 (2)
        Code 471
        Code 200

Director
Office of Naval Research
   Eastern/Central Regional Office
666 Summer Street
Boston, Massachusetts 02210

Director
Office of Naval Research
   Branch Office
536 South Clark Street
Chicago, Illinois 60605

Director
Office of Naval Research
New York Area Office
715 Broadway - 5th Floor
New York, New York 10003

Director
Office of Naval Research
   Western Regional Office
1030 East Green Street
Pasadena, California 91106

Naval Research Laboratory (6)
Code 2627
Washington, D.C. 20375

Defense Technical Information Center (12)
Cameron Station
Alexandria, Virginia 22314

Navy

Undersea Explosion Research Division
Naval Ship Research and Development
   Center
Norfolk Naval Shipyard
Portsmouth, Virginia 23709
Attn: Dr. E. Palmer, Code 177

Navy (Con't.)

Naval Research Laboratory
Washington, D.C. 20375
Attn: Code 8400
             8410
             8430
             8440
             6300
             6390
             6380

David W. Taylor Naval Ship Research
   and Development Center
Annapolis, Maryland 21402
Attn: Code 2740
             28
             281

Naval Weapons Center
China Lake, California 93555
Attn: Code 4062
             4520

Commanding Officer
Naval Civil Engineering Laboratory
Code L31
Port Hueneme, California 93041

Naval Surface Weapons Center
White Oak
Silver Spring, Maryland 20910
Attn: Code R-10
             G-402
             K-82

Technical Director
Naval Ocean Systems Center
San Diego, California 92152

Supervisor of Shipbuilding
U.S. Navy
Newport News, Virginia 23607

Navy Underwater Sound
   Reference Division
Naval Research Laboratory
P.O. Box 8337
Orlando, Florida 32806

Chief of Naval Operations
Department of the Navy
Washington, D.C. 20350
Attn: Code OP-098

Navy (Con't.)

Strategic Systems Project Office
Department of the Navy
Washington, D.C. 20376
Attn: NSP-200

Naval Air Systems Command
Department of the Navy
Washington, D.C. 20361
Attn: Code 5302 (Aerospace and Structures)
            604 (Technical Library)
            320B (Structures)

Naval Air Development Center
Warminster, Pennsylvania 18974
Attn: Aerospace Mechanics
            Code 606

U.S. Naval Academy
Engineering Department
Annapolis, Maryland 21402

Naval Facilities Engineering Command
200 Stovall Street
Alexandria, Virginia 22332
Attn: Code 03 (Research and Development)
            04B
            045
            14114 (Technical Library)

Naval Sea Systems Command
Department of the Navy
Washington, D.C. 20362
Attn: Code 05H
            312
            322
            323
            05R
            32R

Navy (Con't.)

Commander and Director
David W. Taylor Naval Ship
    Research and Development Center
Bethesda, Maryland 20084
Attn: Code 042
            17
            172
            173
            174
            1800
            1844
            012.2
            1900
            1901
            1945
            1960
            1962

Naval Underwater Systems Center
Newport, Rhode Island 02840
Attn: Bruce Sandman, Code 3634

Naval Surface Weapons Center
Dahlgren Laboratory
Dahlgren, Virginia 22448
Attn: Code G04
            G20

Technical Director
Mare Island Naval Shipyard
Vallejo, California 94592

U.S. Naval Postgraduate School
Library
Code 0384
Monterey, California 93940

Webb Institute of Naval Architecture
Attn: Librarian
Crescent Beach Road, Glen Cove
Long Island, New York 11542

Army

Commanding Officer (2)
U.S. Army Research Office
P.O. Box 12211
Research Triangle Park, NC 27709
Attn: Mr. J. J. Murray, CRD-AA-IP

Army (Con't.)

Watervliet Arsenal
MAGGS Research Center
Watervliet, New York 12189
Attn: Director of Research

U.S. Army Materials and Mechanics
  Research Center
Watertown, Massachusetts 02172
Attn: Dr. R. Shea, DRXMR-T

U.S. Army Missile Research and
  Development Center
Redstone Scientific Information
  Center
Chief, Document Section
Redstone Arsenal, Alabama 35809

Army Research and Development
  Center
Fort Belvoir, Virginia 22060

NASA

National Aeronautics and Space
  Administration
Structures Research Division
Langley Research Center
Langley Station
Hampton, Virginia 23365

National Aeronautics and Space
  Administration
Associate Administrator for Advanced
  Research and Technology
Washington, D.C. 20546

Air Force

Wright-Patterson Air Force Base
Dayton, Ohio 45433
Attn: AFFDL (FB)
          (FBR)
          (FBE)
          (FBS)
      AFML (MBM)

Chief Applied Mechanics Group
U.S. Air Force Institute of Technology
Wright-Patterson Air Force Base
Dayton, Ohio 45433

Air Force (Con't.)

Chief, Civil Engineering Branch
WLRC, Research Division
Air Force Weapons Laboratory
Kirtland Air Force Base
Albuquerque, New Mexico 87117

Air Force Office of Scientific Research
Bolling Air Force Base
Washington, D.C. 20332
Attn: Mechanics Division

Department of the Air Force
Air University Library
Maxwell Air Force Base
Montgomery, Alabama 36112

Other Government Activities

Commandant
Chief, Testing and Development Division
U.S. Coast Guard
1300 E Street, NW.
Washington, D.C. 20226

Technical Director
Marine Corps Development
  and Education Command
Quantico, Virginia 22134

Director Defense Research
  and Engineering
Technical Library
Room 3C128
The Pentagon
Washington, D.C. 20301

Dr. M. Gaus
National Science Foundation
Environmental Research Division
Washington, D.C. 20550

Library of Congress
Science and Technology Division
Washington, D.C. 20540

Director
Defense Nuclear Agency
Washington, D.C. 20305
Attn: SPSS

Other Government Activities (Con't)

Mr. Jerome Persh
Staff Specialist for Materials
  and Structures
OUSDR&E, The Pentagon
Room 3D1089
Washington, D.C. 20301

Chief, Airframe and Equipment Branch
FS-120
Office of Flight Standards
Federal Aviation Agency
Washington, D.C. 20553

National Academy of Sciences
National Research Council
Ship Hull Research Committee
2101 Constitution Avenue
Washington, D.C. 20418
Attn: Mr. A. R. Lytle

National Science Foundation
Engineering Mechanics Section
Division of Engineering
Washington, D.C. 20550

Picatinny Arsenal
Plastics Technical Evaluation Center
Attn: Technical Information Section
Dover, New Jersey 07801

Maritime Administration
Office of Maritime Technology
14th and Constitution Avenue, NW.
Washington, D.C. 20230

PART 2 - Contractors and Other Technical
         Collaborators

Universities

Dr. J. Tinsley Oden
University of Texas at Austin
345 Engineering Science Building
Austin, Texas 78712

Professor Julius Miklowitz
California Institute of Technology
Division of Engineering
  and Applied Sciences
Pasadena, California 91109

Universities (Con't)

Dr. Harold Liebowitz, Dean
School of Engineering and
  Applied Science
George Washington University
Washington, D.C. 20052

Professor Eli Sternberg
California Institute of Technology
Division of Engineering and
  Applied Sciences
Pasadena, California 91109

Professor Paul M. Naghdi
University of California
Department of Mechanical Engineering
Berkeley, California 94720

Professor A. J. Durelli
Oakland University
School of Engineering
Rochester, Missouri 48063

Professor F. L. DiMaggio
Columbia University
Department of Civil Engineering
New York, New York 10027

Professor Norman Jones
The University of Liverpool
Department of Mechanical Engineering
P. O. Box 147
Brownlow Hill
Liverpool L69 3BX
England

Professor E. J. Skudrzyk
Pennsylvania State University
Applied Research Laboratory
Department of Physics
State College, Pennsylvania 16801

Professor J. Klosner
Polytechnic Institute of New York
Department of Mechanical and
  Aerospace Engineering
333 Jay Street
Brooklyn, New York 11201

Professor R. A. Schapery
Texas A&M University
Department of Civil Engineering
College Station, Texas 77843

Universities (Con't.)

Professor Walter D. Pilkey
University of Virginia
Research Laboratories for the
  Engineering Sciences and
  Applied Sciences
Charlottesville, Virginia 22901

Professor K. D. Willmert
Clarkson College of Technology
Department of Mechanical Engineering
Potsdam, New York 13676

Dr. Walter E. Haisler
Texas A&M University
Aerospace Engineering Department
College Station, Texas 77843

Dr. Hussein A. Kamel
University of Arizona
Department of Aerospace and
  Mechanical Engineering
Tucson, Arizona 85721

Dr. S. J. Fenves
Carnegie-Mellon University
Department of Civil Engineering
Schenley Park
Pittsburgh, Pennsylvania 15213

Dr. Ronald L. Huston
Department of Engineering Analysis
University of Cincinnati
Cincinnati, Ohio 45221

Professor G. C. M. Sih
Lehigh University
Institute of Fracture and
  Solid Mechanics
Bethlehem, Pennsylvania 18015

Professor Albert S. Kobayashi
University of Washington
Department of Mechanical Engineering
Seattle, Washington 98105

Professor Daniel Frederick
Virginia Polytechnic Institute and
  State University
Department of Engineering Mechanics
Blacksburg, Virginia 24061

Universities (Con't)

Professor A. C. Eringen
Princeton University
Department of Aerospace and
  Mechanical Sciences
Princeton, New Jersey 08540

Professor E. H. Lee
Stanford University
Division of Engineering Mechanics
Stanford, California 94305

Professor Albert I. King
Wayne State University
Biomechanics Research Center
Detroit, Michigan 48202

Dr. V. R. Hodgson
Wayne State University
School of Medicine
Detroit, Michigan 48202

Dean B. A. Boley
Northwestern University
Department of Civil Engineering
Evanston, Illinois 60201

Professor P. G. Hodge, Jr.
University of Minnesota
Department of Aerospace Engineering
  and Mechanics
Minneapolis, Minnesota 55455

Dr. D. C. Drucker
University of Illinois
Dean of Engineering
Urbana, Illinois 61801

Professor N. M. Newmark
University of Illinois
Department of Civil Engineering
Urbana, Illinois 61803

Professor E. Reissner
University of California, San Diego
Department of Applied Mechanics
La Jolla, California 92037

Professor William A. Nash
University of Massachusetts
Department of Mechanics and
  Aerospace Engineering
Amherst, Massachusetts 01002

Universities (Con't)

Professor G. Herrmann
Stanford University
Department of Applied Mechanics
Stanford, California 94305

Professor J. D. Achenbach
Northwest University
Department of Civil Engineering
Evanston, Illinois 60201

Professor S. B. Dong
University of California
Department of Mechanics
Los Angeles, California 90024

Professor Burt Paul
University of Pennsylvania
Towne School of Civil and
  Mechanical Engineering
Philadelphia, Pennsylvania 19104

Professor H. W. Liu
Syracuse University
Department of Chemical Engineering
  and Metallurgy
Syracuse, New York 13210

Professor S. Bodner
Technion R&D Foundation
Haifa, Israel

Professor Werner Goldsmith
University of California
Department of Mechanical Engineering
Berkeley, California 94720

Professor R. S. Rivlin
Lehigh University
Center for the Application
  of Mathematics
Bethlehem, Pennsylvania 18015

Professor F. A. Cozzarelli
State University of New York at
  Buffalo
Division of Interdisciplinary Studies
Karr Parker Engineering Building
Chemistry Road
Buffalo, New York 14214

Universities (Con't)

Professor Joseph L. Rose
Drexel University
Department of Mechanical Engineering
  and Mechanics
Philadelphia, Pennsylvania 19104

Professor B. K. Donaldson
University of Maryland
Aerospace Engineering Department
College Park, Maryland 20742

Professor Joseph A. Clark
Catholic University of America
Department of Mechanical Engineering
Washington, D.C. 20064

Dr. Samuel B. Batdorf
University of California
School of Engineering
  and Applied Science
Los Angeles, California 90024

Professor Isaac Fried
Boston University
Department of Mathematics
Boston, Massachusetts 02215

Professor E. Krempl
Rensselaer Polytechnic Institute
Division of Engineering
Engineering Mechanics
Troy, New York 12181

Dr. Jack R. Vinson
University of Delaware
Department of Mechanical and Aerospace
  Engineering and the Center for
  Composite Materials
Newark, Delaware 19711

Dr. J. Duffy
Brown University
Division of Engineering
Providence, Rhode Island 02912

Dr. J. L. Swedlow
Carnegie-Mellon University
Department of Mechanical Engineering
Pittsburgh, Pennsylvania 15213

Universities (Con't)

Dr. V. K. Varadan
Ohio State University Research Foundation
Department of Engineering Mechanics
Columbus, Ohio 43210

Dr. Z. Hashin
University of Pennsylvania
Department of Metallurgy and
  Materials Science
College of Engineering and
  Applied Science
Philadelphia, Pennsylvania 19104

Dr. Jackson C. S. Yang
University of Maryland
Department of Mechanical Engineering
College Park, Maryland 20742

Professor T. Y. Chang
University of Akron
Department of Civil Engineering
Akron, Ohio 44325

Professor Charles W. Bert
University of Oklahoma
School of Aerospace, Mechanical,
  and Nuclear Engineering
Norman, Oklahoma 73019

Professor Satya N. Atluri
Georgia Institute of Technology
School of Engineering and
  Mechanics
Atlanta, Georgia 30332

Professor Graham F. Carey
University of Texas at Austin
Department of Aerospace Engineering
  and Engineering Mechanics
Austin, Texas 78712

Dr. S. S. Wang
University of Illinois
Department of Theoretical and
  Applied Mechanics
Urbana, Illinois 61801

Professor J. F. Abel
Cornell University
Department of Theoretical
  and Applied Mechanics
Ithaca, New York 14853

Universities (Con't)

Professor V. H. Neubert
Pennsylvania State University
Department of Engineering Science
  and Mechanics
University Park, Pennsylvania 16802

Professor A. W. Leissa
Ohio State University
Department of Engineering Mechanics
Columbus, Ohio 43212

Professor C. A. Brebbia
University of California, Irvine
Department of Civil Engineering
School of Engineering
Irvine, California 92717

Dr. George T. Hahn
Vanderbilt University
Mechanical Engineering and
  Materials Science
Nashville, Tennessee 37235

Dean Richard H. Gallagher
University of Arizona
College of Engineering
Tucson, Arizona 85721

Professor E. F. Rybicki
The University of Tulsa
Department of Mechanical Engineering
Tulsa, Oklahoma 74104

Dr. R. Haftka
Illinois Institute of Technology
Department of Mechanics and Mechanical
  and Aerospace Engineering
Chicago, Illinois 60616

Professor J. G. de Oliveira
Massachusetts Institute of Technology
Department of Ocean Engineering
77 Massachusetts Avenue
Cambridge, Massachusetts 02139

Dr. Bernard W. Shaffer
Polytechnic Institute of New York
Route 110
Farmingdale, New York 11735

Industry and Research Institutes	Industry and Research Institutes (Con't)
Dr. Norman Hobbs Kaman AviDyne Division of Kaman Sciences Corporation Burlington, Massachusetts 01803	Dr. T. L. Geers Lockheed Missiles and Space Company 3251 Hanover Street Palo Alto, California 94304
Argonne National Laboratory Library Services Department 9700 South Cass Avenue Argonne, Illinois 60440	Mr. William Caywood Applied Physics Laboratory Johns Hopkins Road Laurel, Maryland 20810
Dr. M. C. Junger Cambridge Acoustical Associates 54 Rindge Avenue Extension Cambridge, Massachusetts 02140	Dr. Robert E. Dunham Pacifica Technology P.O. Box 148 Del Mar, California 92014
Mr. J. H. Torrance General Dynamics Corporation Electric Boat Division Groton, Connecticut 06340	Dr. M. F. Kanninen Battelle Columbus Laboratories 505 King Avenue Columbus, Ohio 43201
Dr. J. E. Greenspon J. G. Engineering Research Associates 3831 Menlo Drive Baltimore, Maryland 21215	Dr. A. A. Hochrein Daedalean Associates, Inc. Springlake Research Road 15110 Frederick Road Woodbine, Maryland 21797
Newport News Shipbuilding and Dry Dock Company Library Newport News, Virginia 23607	Dr. James W. Jones Swanson Service Corporation P.O. Box 5415 Huntington Beach, California 92646
Dr. W. F. Bozich McDonnell Douglas Corporation 5301 Bolsa Avenue Huntington Beach, California 92647	Dr. Robert E. Nickell Applied Science and Technology 3344 North Torrey Pines Court Suite 220 La Jolla, California 92037
Dr. H. N. Abramson Southwest Research Institute 8500 Culebra Road San Antonio, Texas 78284	Dr. Kevin Thomas Westinghouse Electric Corp. Advanced Reactors Division P. O. Box 158 Madison, Pennsylvania 15663
Dr. R. C. DeHart Southwest Research Institute 8500 Culebra Road San Antonio, Texas 78284	Dr. H. D. Hibbitt Hibbitt & Karlsson, Inc. 132 George M. Cohan Boulevard Providence, Rhode Island 02903
Dr. M. L. Baron Weidlinger Associates 110 East 59th Street New York, New York 10022	Dr. R. D. Mindlin 89 Deer Hill Drive Ridgefield, Connecticut 06877

I

Industry and Research Institutes (Con't)

Dr. Richard E. Dame
Mega Engineering
11961 Tech Road
Silver Spring, Maryland   20904

Mr. G. M. Stanley
Lockheed Palo Alto Research
  Laboratory
3251 Hanover Street
Palo Alto, California   94304

Mr. R. L. Cloud
Robert L. Cloud Associates, Inc.
2972 Adeline Street
Berkeley, California   94703